Ultrafast low-energy electron diffraction at surfaces

Probing transitions and phase-ordering of charge-density waves

DISSERTATION

zur Erlangung des mathematisch-naturwissenschaftlichen Doktorgrades
“Doctor rerum naturalium”
der Georg-August-Universität Göttingen
-
im Promotionsprogramm ProPhys
der Georg-August University School of Science (GAUSS)

vorgelegt von
Herrn Simon Vogelgesang,
geb. Schweda
aus Göttingen

Göttingen, 2018

Betreuungsausschuss

Prof. Dr. Claus Ropers, IV. Physikalisches Institut

Prof. Dr. Alec M. Wodtke, Institut für Physikalische Chemie /
Max-Planck-Institut für biophysikalische Chemie

Mitglieder der Prüfungskommission

Referent: Prof. Dr. Claus Ropers, IV. Physikalisches Institut

Korreferent: Prof. Dr. Stefan Mathias, I. Physikalisches Institut

Weitere Mitglieder der Prüfungskommission

Prof. Dr. Fabian Heidrich-Meisner, Institut für Theoretische Physik

Prof. Dr. Sarah Köster, Institut für Röntgenphysik

Prof. Dr. Peter Sollich, Institut für Theoretische Physik

Prof. Dr. Alec M. Wodtke, Institut für Physikalische Chemie /
Max-Planck-Institut für biophysikalische Chemie

Tag der mündlichen Prüfung: 05.12.2018

Abstract

Due to their reduced dimensionality, surfaces and quasi two-dimensional materials exhibit numerous intriguing physical phenomena that drastically differ from the bulk. To resolve these effects and the associated dynamics at their intrinsic timescales requires experimental methodologies combining a high surface sensitivity with the essential temporal resolution. However, to date, there are still very few methods that facilitate investigation of the structural degrees of freedom of surfaces on the atomic scale along with a temporal resolution of femtoseconds or picoseconds.

Addressing these challenges, this thesis covers the development and application of ultrafast low-energy electron diffraction in a backscattering geometry to study structural dynamics at surfaces.

In this context, a central aspect is the development of a miniaturized and laser-driven electron source based on a nanometric needle photocathode. Using such a sharp metal tip, the photoemitted electron bunches offer a particularly high coherence and remarkably short pulse durations, which were also successfully implemented recently in ultrafast transmission electron microscopy, as well as in time-resolved transmission low-energy electron diffraction.

Employing the capabilities of this novel technique, so-called transition metal dichalcogenides constitute an ideal prototype system. Specifically, in the present work, the transient structural disorder of charge-density waves at the surface of 1T-TaS$_2$ has been examined. Following the optically induced transition between two temperature-dependent charge-density wave phases, this method enables the observation of a highly disordered transient state and the subsequent phase-ordering kinetics. More precisely, the temporal evolution of the growing charge-density correlation length is traced over several hundreds of picoseconds and found to obey a power-law scaling behavior. Due to the particular properties of the charge-density wave system at hand, the observed transient disorder can be explained by the ultrafast formation of topological defects and their subsequent annihilation. These results are complemented by a numerical modeling using a time-dependent Ginzburg-Landau approach.

Finally, two different excitation schemes demonstrating the possibility to study the relaxation of the investigated sample on the nanosecond and microsecond timescale are presented, as well as future prospects of ultrafast low-energy electron diffraction, including other promising surface sample systems.

Contents

Chapter 1

Introduction

Considering the chemical properties of a material, one may notice that these are largely defined by its *surface*, which generally involves the outermost atomic layers that separate the bulk from vacuum. In comparison, boundary layers between two different materials or media are commonly referred to as *interfaces*.

Both cases have in common a broken translational symmetry, as the boundary atoms are missing bonds that would exist in the bulk. For this reason, both surfaces and interfaces exhibit properties which drastically differ from the bulk, such as surface states [1, 2], modified band structures [3, 4] or surface reconstructions [5, 6].

Furthermore, systems of reduced dimensionality exhibit a wealth of fundamental phenomena exclusively present herein. Promoted by the discovery of graphene and its outstanding mechanical and electronic properties, the recent years have experienced a rapidly growing interest in other (quasi) two-dimensional (2D) materials [7]. Among the numerous 2D systems studied, a prototype material class are transition metal dichalcogenides (TMDCs), which are exceptionally prone to electron correlation effects such as superconductivity or charge-density and spin-density instabilities [8, 9]. Moreover, in low-dimensional materials, the concept of topology plays an important role. Here, the unbinding of topological defects can cause a new type of phase transition, as originally predicted by Kosterlitz and Thouless [10]. Such defects may take many forms and appear as dislocations in atomic lattices, as well as vortices in superfluids or magnetic structures [11–13]. From a quantum mechanical perspective, the distinct interplay between surfaces and topologically protected states is particularly evident in phenomena such as the quantum Hall effect or topological insulators [14, 15].

Furthermore, the peculiar properties of surfaces, interfaces and low-dimensional materials form the basis for a multitude of technological applications. The particular relevance for practical utilizations is vividly summarized in a quote by Herbert Kroemer, one of the pioneers in the field of semiconductor heterojunctions. Being awarded the Nobel Prize in 2001, he stated in his laureate speech [16]:

> *"Often, it may be said that the interface is the device."*
>
> - Herbert Kroemer, 2001

Prominent examples for devices based on the unique properties of surfaces which we encounter on a daily basis include photovoltaics, rechargeable batteries, catalysts for chemical processing or exhaust gas treatment, as well as nanoscale integrated electronics. Providing essential fundamental knowledge, the field of *surface science* constitutes an indispensable means for the development of these applications, as it deals with the analysis of elementary electronic, magnetic or structural properties of surfaces. In this context, experimental methods offering outstanding surface sensitivity are the central requirement [17]. As the latter is closely related to the penetration depth of the respective physical probe, for instance, photons in the visible range are ideally suited to analyze a surface's dielectric properties, since they are absorbed or reflected within the first few tens of nanometers (nm) depending on the material's dielectric response. The spatial resolution of photon-based techniques, however, is usually limited to half of the wavelength of the incident light.

As the de Broglie wavelength of electrons or ions is typically on the order of the interatomic distances or below, electron or ion scattering offers a drastically increased spatial resolution. Moreover, low-energy electrons are characterized in particular by a very small inelastic mean free path in most materials, which makes them a probe of remarkable surface sensitivity [18]. This fact is utilized in well-established experimental techniques such as low-energy electron diffraction (LEED) or microscopy (LEEM) that are well suited to investigate a surface's lattice structure and morphology [18, 19]. Further methods making use of the short escape depth of slow electrons are, e.g., Auger electron spectroscopy (AES) or angle-resolved photoemission spectroscopy (ARPES) [6, 17]. In comparison, these approaches are rather sensitive to the chemical composition and the electronic band structure of a surface, respectively.

In particular, LEED played a considerable role in the development of surface science. First, it has been closely connected to the early stages of surface analysis, since Gerhard Ertl *et al.* used LEED to study hydrogen adsorption on palladium in 1974 [20]. Second, over time, LEED became a standard method for static surface structure determination due to its relatively simple and low-cost implementation together with a well-established theoretical framework.

In the recent decades, aiming for the fundamental understanding of dynamic processes at surfaces, there has been much interest in extending surface science to the time domain [1]. For example, this addresses the analysis of chemical reactions, phase transitions or the formation of surface reconstructions, which occur on the timescale of femtoseconds (fs) or picoseconds (ps). In order to attain time-domain access to such processes, commonly, pump-probe approaches are pursued, which allow for disentangling complex correlations by means of their relaxation behavior. As the necessary temporal resolution is typically provided by femtosecond laser systems, all-optical pump-probe schemes are a well-established approach to study the electronic degrees of freedom. Prominent examples for such techniques are transient reflectivity measurements or time-resolved ARPES [21–23].

In comparison, investigating the structural dynamics of the outermost atomic layers has proven much more complex and the number of available methods is very limited. The main reason for this difficulty is the challenge of generating high-quality femtosecond-pulsed electron beams at low kinetic energies. In this context, the problems are twofold: First, electron pulses are highly susceptible to external electric and magnetic fields, as well as internal Coulomb repulsion leading to space-charge broadening. Secondly, a finite kinetic energy spread causes a pronounced dispersion of the electron pulses on their way from the source to the sample. Both effects are particularly severe for low-energy electrons, as a result of the longer propagation and interaction times [24].

This problem has been circumvented by time-resolved reflection high-energy electron diffraction (RHEED) [25–27]. However, as RHEED gains its elevated surface sensitivity from grazing incidence electron pulses, this approach is characterized by an elongated probing area. To compensate for the resulting velocity mismatch between the electrons and the pump pulse, the examined region needs to be excited by means of a tilted pulse front scheme [28]. Moreover, the indexing of individual diffraction peaks and quantitative intensity measurements turn out non-trivial, as the symmetry of the diffraction pattern is heavily dependent on the sample's azimuthal orientation, and, for small incidence angles, diffraction peak intensities are dominated by surface wave resonances [29].

In comparison, using low-energy electron pulses at normal incidence allows one to harness the full potential of LEED, which manifests in, e.g., intrinsically symmetric diffraction patterns, as well as a well-proven theoretical background for their analysis.
To address the above-mentioned challenges of electron pulse broadening, nanometric metal tips have been suggested for their use as highly confined electron sources [30, 31]. Such photocathodes not only have the advantage of rapid electron bunch acceleration in the very vicinity of the tip apex, due to a drastically enhanced static electric field. The nanoscale emission area at the tip apex also leads to a remarkably high coherence of the photo-emitted electron pulses [32]. For this reason, recently, nanoscopic photocathodes have been successfully implemented in an ultrafast transmission electron microscope (UTEM) [33], in ultrafast point-projection microscopy [34, 35], as well as in a time-resolved LEED setup operated in transmission geometry [36]. Whereas the latter experiment is ideally suited for the investigation of atomically thin films, due to the high scattering cross section of low-energy electrons, it is limited to samples up to a few nanometer in thickness. Therefore, to attain access to the entire wealth of potential material systems and fundamental surface phenomena, the development of ultrafast LEED working in the classical back-scattering geometry is highly desirable.

This thesis demonstrates the first implementation and application of ultrafast low-energy electron diffraction (ULEED) for the investigation of structural dynamics at surfaces. Specifically, ULEED is employed to resolve the phase-ordering kinetics associated with a structural phase transition at the surface of a very prominent model system, namely, the highly correlated quasi two-dimensional material 1T-TaS$_2$[37].
For the development of the present ULEED system, the key component is a millimeter-sized electron source, which has been constructed in collaboration with Gero Storeck. It tackles the challenge of electron pulse broadening due to velocity dispersion by a reduction of propagation distance. Featuring a nanometric needle photoemitter, this miniaturized electron gun allows for recording unobscured diffraction patterns even at working distances down to a few millimeter from the sample in combination with a remarkable k-space resolution.
Enabled by the novel capabilities of ULEED operated in back-reflection geometry, we study a structural phase transition caused by charge-density waves (CDW) at the surface of the layered transition metal dichalcogenide (TMDC) 1T-TaS$_2$. Herein, after intense optical excitation, we observe a pronounced decrease of the CDW correlation length that is traced back to the appearance of topological defects in the high-temperature CDW

phase. The subsequent phase-ordering kinetics are governed by a power-law growth of the CDW correlation length, which is attributed to the annihilation of topological defects. These findings are corroborated by a numerical simulation, which models the dynamics of the high-temperature CDW phase in real space using a time-dependent Ginzburg-Landau approach.

In conclusion, ULEED represents a novel technique that allows for unique insights into the ultrafast structural dynamics of so-far elusive fundamental physical effects at surfaces.

Outline

This work is structured as follows: In Chap. 2, the basic methods and fundamental concepts essential for the further discussion of the ULEED experiment and the investigated sample system are introduced. This comprises the elementary principles of LEED and diffraction pattern formation at surfaces, as well as the general properties of CDWs and key characteristics of topological defects. Chapter 3 focuses on the structural and electronic properties of 1T-TaS$_2$, with a particular emphasis on the present temperature-dependent CDWs.

The detailed experimental realization of the ULEED setup is presented in Chap. 4, which includes the design of the miniaturized electron source and the spatio-temporal characterization of the emitted electron pulses, as well as the necessary ultra-high vacuum (UHV) chamber system. Chapter 5 encompasses the presentation and analysis of the time-resolved measurement data which focuses on the transition from the room-temperature to the high-temperature CDW phase. Particular emphasis is placed on the temporary disorder associated with the CDW phase transition. Since the decrease of the CDW correlation length is attributed to the appearance and ensuing annihilation of topological defects inside the CDW, in Chap. 6, these findings are substantiated by a numerical simulation of the CDW dynamics after a transition to the high-temperature phase following intense optical excitation.

Two further excitation schemes, which mainly concentrate on the relaxation behavior of 1T-TaS$_2$, are briefly described in Chap. 7. The first approach, based on optical pumping with a second electronically synchronized ns-laser, addresses the temporal recovery of the room temperature CDW phase. In comparison, the second excitation scheme utilizes single laser-pulse excitation inside a TEM to observe a probabilistic switching between the two degenerate and intrinsically chiral CDW ground states in real space.

In the subsequent discussion in Chap. 8, the experimental observations are compared to the results of the numerical modeling and further work on 1T-TaS_2 using different experimental techniques. Finally, Chapter 9 summarizes the experimental results of this thesis and gives an outlook on further fundamental phenomena and intriguing material systems that can be investigated with ULEED.

Chapter 2

Methods and concepts

To establish the theoretical and experimental methods essential within this work, this chapter provides an introduction to the basic principles of low-energy electron diffraction, as well as the concepts necessary to describe the investigated sample system. This includes a brief summary of the historical incidents around the invention of LEED, the fundamental concepts of electron scattering at crystalline surfaces (Sec. 2.1), as well as the influence of surface superstructures and domains on LEED diffraction patterns (Sec. 2.2). The following sections focus on the formation of charge-density waves in low-dimensional materials (Sec. 2.3) and on the description and characterization of topological defects present in numerous systems exhibiting a broken continuous symmetry (Sec. 2.4).

2.1 Fundamental principles of LEED

2.1.1 Historical background

Like numerous pioneering inventions, the discovery of electron diffraction and LEED in particular happened as a consequence of intuition of the involved experimentalists and fortunate circumstances. Launching a series of experiments in 1924, Clinton Davisson and Lester Germer originally intended to investigate the extranuclear structure of atoms by means of elastically scattered electrons, similarly to the alpha particle scattering experiments conducted by Ernest Rutherford. However, a few months later, their work got interrupted by a cracked vacuum tube leading to an accidental oxidation of the nickel target. Subsequently, they observed a pronounced electron scattering in certain directions [38], and a thorough analysis of the target showed that the repeated heating had caused the growth of several single crystalline facets in the formerly polycrystalline sample. From this fact, Davisson and Germer surmised that rather the arrangement of the atoms than their inner structure would be the reason for their unexpected observations. Still, it took another year until they realized the full scope of their findings, which ironically happened during a talk of Max Born, who cited previous results of Davisson as an evidence for the existence of matter waves postulated by de Broglie [39]. Encouraged by Born, they pursued their search for diffracted electron beams with even more enthusiasm, and in January 1927, they finally observed “a quantum bump” in an energy-dependent scattering measurement [38]. These diffraction peaks and other results, which clearly indicated the observation of the three-fold symmetry of the nickel crystal, were published in a short note in April of 1927 [40]. In retrospect, their hurry is justified by the fact that only one moth later, George Paget Thomson and Andrew Reid published their results of electron diffraction at thin films [41]. In contrast to Davisson and Germer, they used high-energy electron beams for scattering at very thin celluloid and metal films and obtained ring-like diffraction patterns. For their works, which paved the road for structure determination by means of electrons, Davisson and Thomson shared the Nobel prize in 1937 [42].

However, in the 1930s LEED was an arduous business, since vacuum chambers consisted of hand-blown glass tubes, and electron beams had to be recorded with manually manipulated Faraday cups. These technological difficulties primarily prevented LEED from immediately becoming a common method for surface analysis, and it was not until the 1960s that vacuum technology was developed so far that it could routinely provide for clean surfaces [17]. In the meantime, experimentalists introduced advancements such as improved electron sources, luminescent screens and retarding grid energy filters, which allowed for the visualization and photographic recording of diffraction patterns [6, 43, 44]. Especially, the commercial availability of UHV equipment triggered massive progress in the field of surface science and LEED in particular. The increased interest of both experimentalists and theoreticians led to the development of more involved dynamical scattering theories. As a consequence, for several decades, LEED has been a well-established technique for surface structure determination [17].

In the 1980s, surface science again experienced rapid progress with the advent of scanning tunneling microscopy (STM) [5, 45]. As it was complementary to LEED, this technique enabled the analysis of surfaces and point-like defects in real space and with atomic resolution. The groundbreaking new perspective on surfaces and fundamental insights facilitated by STM led to the Nobel Prize for Binnig and Rohrer only a few years later [46]. However, despite the distinguished role STM and other scanning probe techniques have played for surface science to date, LEED is still a very important method to obtain long-range surface lattice structures and determine atomic distances with the highest accuracy [18].

2.1.2 Low-energy electron scattering

To obtain information about a crystal's lattice structure by means of electron diffraction, the elastically scattered electrons are of particular interest, as they have the ability to form diffraction patterns by interference. Accordingly, how far electrons penetrate into the bulk before they lose part of their kinetic energy determines a critical depth (or sample thickness) up to which structural information is encoded in a diffraction pattern. Hence, an important quantity is the probability for inelastic scattering, such as interactions with plasmons or phonons. A measure for this probability is the inelastic mean-free path Λ (IMFP) of electrons in matter, which is defined as the distance after which the fraction e^{-1} of the beam is propagating with its original energy [6]. In many experiments $\Lambda(E)$, is found to be rather insensitive to the atomic number of the considered species [47]. Thus, $\Lambda(E)$ follows the so-called "universal curve" of the inelastic mean-free path for electrons in matter, which has a minimum at an energy of a few tens of eV (see Fig. 2.1) [47]. Close to this energy, it is very likely for electrons to experience an inelastic scattering event within the first few atomic layers, and accordingly, the elastically scattered electrons within this energy range could not penetrate the sample deeper than approximately 5 to 10 Å. This gives rise to the very high surface sensitivity of LEED.

As can be seen in Fig. 2.1, $\Lambda(E)$ is characterized by two branches of different slope in the log-log-plot. This is due to the approximation that for low-energy excitations Λ

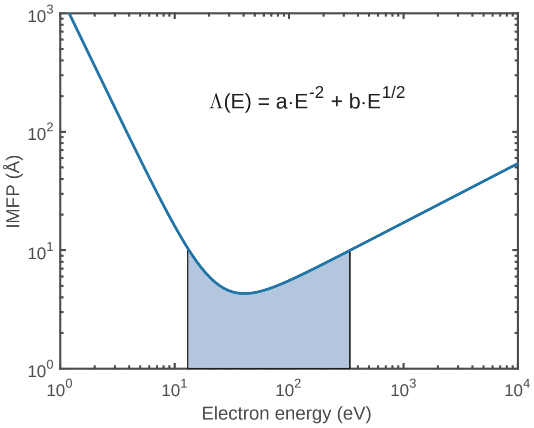

Figure 2.1: Fit of the inelastic mean-free path $\Lambda(E)$. Fit parameters $a = 143$ and $b = 0.054$ resemble a variety of elements [47]. For electron energies 13 eV $\lesssim E \lesssim$ 340 eV with respect to the Fermi level the IMFP Λ is smaller than 1 nm (shaded area) giving rise to the high surface sensitivity of LEED.

is inversely proportional to simple excitation of electron-hole-pairs, which in turn are proportional the number for unoccupied electron states ($\propto E$) as well as holes ($\propto E$), i.e., $\Lambda \propto E^{-2}$ [48]. For higher electron energies, ionization and plasmon excitations become the dominant loss process, and in a simple model, the inelastic scattering cross section is assumed proportional to the interaction time τ. Hence, above approximately 150 eV, Λ increases with $\sqrt{E}$ [48].

Additionally, at electron energies between a few tens and hundreds of eV, the wavelength $\lambda = h/p$ of the incident electrons coincides well with typical atomic distances in a crystal of a few Å. For this reason, elastically scattered electrons exit the surface at large diffraction angles, which makes them readily detectable and provides for high k-space resolution. These two factors - the short penetration depth combined with a well suited electron wavelength - form the basis of all LEED experiments and renders low-energy electrons not just an excellent probe for surface structure determination, but also makes them ideally suited to investigate ultra-thin films in transmission diffraction. This has been demonstrated recently by studying the dynamics of polymer superstructures on a freestanding graphene substrate [36].

2.1.3 Diffraction at surfaces

While often the corpuscular nature of electrons is instructive for discussing inelastic scattering processes, their wave-like properties are essential for the understanding of elastic interactions. For many situations, electrons impinging on a surface can be described as a plane wave interacting with the periodic potential of the atomic lattice. Then, following Huygens' principle, all atoms involved act as emitters of a spherical waves, which in turn interfere with each other and lead to plane waves propagating in certain directions.
To qualitatively understand the diffraction patterns observed by LEED (i.e., the positions of refections), it is sufficient to stay within the framework of the *kinematic approximation* meaning that incident waves scatter exactly once, while fulfilling energy and momentum conservation. However, to comprehensively describe the intensity of individual diffraction peaks, dynamic or multiple scattering theory is necessary.

To consider diffraction at surfaces within the kinematic approximation, the *Bravais lattice* of a surface is defined in terms of the two basis vectors $\boldsymbol{a}_1$ and $\boldsymbol{a}_2$. Then, the position of an arbitrary unit cell is given by $\boldsymbol{R}_{mn} = m\boldsymbol{a}_1 + n\boldsymbol{a}_2$ (Fig. 2.2).
Assuming that the incident plane wave $\exp(i\boldsymbol{k}\boldsymbol{r})$ is scattered at the origin of the lattice,

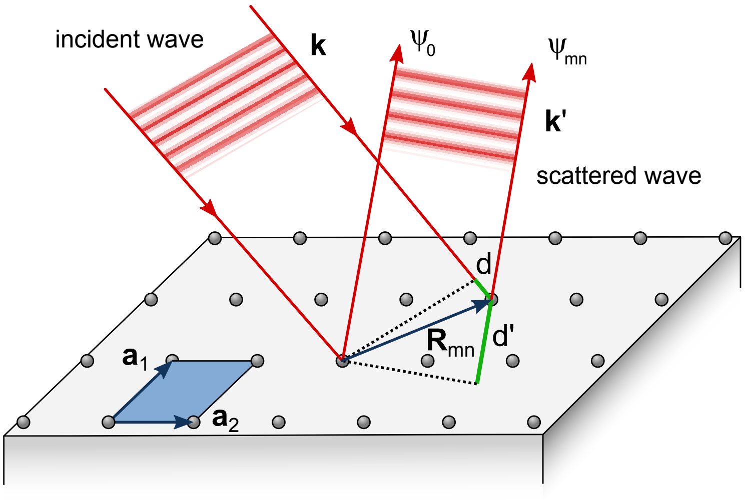

Figure 2.2: Electron waves (red) being scattered at a crystalline surface or the respective lattice unit cells (blue) defined by $\boldsymbol{a}_1$ and $\boldsymbol{a}_2$. The path difference (green) between the two waves ψ_0 and ψ_{mn} is giving rise to a phase-shift, leading to constructive interference in certain directions.

in the far field, the outgoing wave may be described as a plane wave $\psi_0 = f \cdot \exp\left(i\boldsymbol{k}'\boldsymbol{r}\right)$ with wavevector $\boldsymbol{k}'$ and an amplitude $f\left(\boldsymbol{k}, \boldsymbol{k}', \boldsymbol{r}\right)$, which is depending on the composition of the lattice unit cell (atomic positions and species) [49]. The wave emitted at position $\boldsymbol{R}_{mn}$ in direction $\boldsymbol{k}'$ then just contains a phase shift given by the inner products $(\boldsymbol{k} \cdot \boldsymbol{R}_{mn})$ and $(\boldsymbol{k}' \cdot \boldsymbol{R}_{mn})$ and reads

$$\psi_{mn} = \psi_0 \cdot \exp\left(i\left(\boldsymbol{k}' - \boldsymbol{k}\right)\boldsymbol{R}_{mn}\right) = \psi_0 \cdot \exp\left(i\boldsymbol{K}\boldsymbol{R}_{mn}\right) \tag{2.1}$$

with the scattering vector $\boldsymbol{K} = \boldsymbol{k}' - \boldsymbol{k}$ (cf. Fig. 2.2). If the Bravais lattice unit cell contains J atoms at positions $\boldsymbol{r}_j$ possibly differing in species, this can be accounted for by varying ψ_{0j} with f_j. Then, $\boldsymbol{r} = \boldsymbol{R}_{mn} + \boldsymbol{r}_j$ unambiguously determines the atomic positions inside the crystal lattice. Finally, the observed diffracted intensity $I = \left|\sum \psi_{mn}\right|^2$ is obtained via summation over the finite numbers M and N of unit cells in directions

$\boldsymbol{a}_1$ and $\boldsymbol{a}_2$, respectively, as well as the J atoms inside one unit cell:

$$I = \left| \sum_{m,n,j} \psi_{0j} \cdot \exp\left(i\boldsymbol{K}\left(\boldsymbol{R}_{mn} + \boldsymbol{r}_j\right)\right) \right|^2 \tag{2.2}$$

$$= \underbrace{\left| \sum_{j=1}^{J} f_j \cdot \exp\left(i\boldsymbol{K}\boldsymbol{r}_j\right) \right|^2}_{\text{basis}} \cdot \underbrace{\left| \sum_{m,n=1}^{M,N} \exp\left(i\boldsymbol{K}\boldsymbol{R}_{mn}\right) \right|^2}_{\text{lattice}} = |F|^2 \cdot |S|^2 \tag{2.3}$$

Commonly, $|S|^2$ is referred to as the structure factor of the lattice, whereas $|F|^2$ denotes the form factor defined by the basis of the unit cell. Using the geometric series, the lattice term can also be expressed as

$$|S|^2 = \frac{\sin\left(\frac{M}{2} \cdot \boldsymbol{K}\boldsymbol{a}_1\right)^2}{\sin\left(\frac{1}{2} \cdot \boldsymbol{K}\boldsymbol{a}_1\right)^2} \cdot \frac{\sin\left(\frac{N}{2} \cdot \boldsymbol{K}\boldsymbol{a}_2\right)^2}{\sin\left(\frac{1}{2} \cdot \boldsymbol{K}\boldsymbol{a}_2\right)^2}\,, \tag{2.4}$$

which defines a series of peaks that get sharper as more scattering entities contribute, i.e., $I_{max} \propto (MN)^2$ [50]. The condition for peaks to appear are the zeros of Eq. 2.4 given by

$$\boldsymbol{K} \cdot \boldsymbol{a}_1 = 2\pi \cdot h \quad \text{and} \quad \boldsymbol{K} \cdot \boldsymbol{a}_2 = 2\pi \cdot k \quad h, k \,\epsilon\, \mathbb{N}. \tag{2.5}$$

These are commonly referred to as the *Laue conditions* for diffraction, with h, k being the corresponding *Miller indices* [49, 51]. If $\boldsymbol{K}$ meets these conditions, it can be expressed as the linear combination $\boldsymbol{K} = h\boldsymbol{a}_1^* + k\boldsymbol{a}_2^*$ of vectors $\boldsymbol{a}_1^*$ and $\boldsymbol{a}_2^*$ that fulfill

$$\boldsymbol{a}_i\boldsymbol{a}_j^* = 2\pi\delta_{ij}\,. \tag{2.6}$$

Eq. 2.6 is the definition for the so-called *reciprocal lattice vectors* $\boldsymbol{a}_j^*$, which are pairwise orthogonal to $\boldsymbol{a}_i$. Moreover, this definition illustrates that the lengths of vectors $\boldsymbol{a}_i$ and $\boldsymbol{a}_i^*$ have to be inversely proportional to each other.

To obtain a comprehensive view of the whole reciprocal lattice, $\boldsymbol{a}_3^*$ has to be considered as well. Since the number of scattering entities in $\boldsymbol{a}_3$ direction is limited by the surface on the one side and by an extremely short penetration depth on the other side, only very few layers contribute to the cardinal sine function equivalent to Eq. 2.4. Hence, the diffraction peaks at positions $\boldsymbol{a}_3^*$ become very broad and can be even approximated as “rod-like”, which is depicted in Fig. 2.3a.

Generally, as can be seen from Eq. 2.2, the diffracted intensity I may be viewed as a product of two Fourier transforms of the real-space lattice: Here, $|S|^2$ generates sharp peaks at the reciprocal lattice sites, whereas $|F|^2$ is a smoothly varying function, which modulates the intensity of the diffraction peaks.

2.1.4 Ewald sphere

The Laue equations state that diffraction occurs if the scattering vector $\boldsymbol{K} = \boldsymbol{k}' - \boldsymbol{k}$ equals a reciprocal lattice vector

$$\boldsymbol{G} = h\boldsymbol{a}_1^* + k\boldsymbol{a}_2^* + l\boldsymbol{a}_3^* \,. \tag{2.7}$$

However, at surfaces this condition is weakened due to the rod-like extension of $\boldsymbol{a}_3^*$. Hence, during electron diffraction, additionally to energy and momentum conservation, the component of $\boldsymbol{k}$ parallel to the surface is conserved except for an in-plane reciprocal lattice vector, i.e.,

$$|\boldsymbol{k}'| = |\boldsymbol{k}| \quad \text{and} \tag{2.8}$$

$$\boldsymbol{k}'_{||} = \boldsymbol{k}_{||} + \boldsymbol{G} = \boldsymbol{k}_{||} + h\boldsymbol{a}_1^* + k\boldsymbol{a}_2^* \,. \tag{2.9}$$

This situation is nicely illustrated by the *Ewald sphere* construction. For its assembly, the end of the incident wavevector $\boldsymbol{k}$ is fixed at the origin of the reciprocal lattice, while a sphere of radius $|\boldsymbol{k}|$ is drawn around its start. Then, the intersections of sphere's surface and the rods of the reciprocal lattice define the directions at which diffraction peaks will be present (Fig 2.3b).

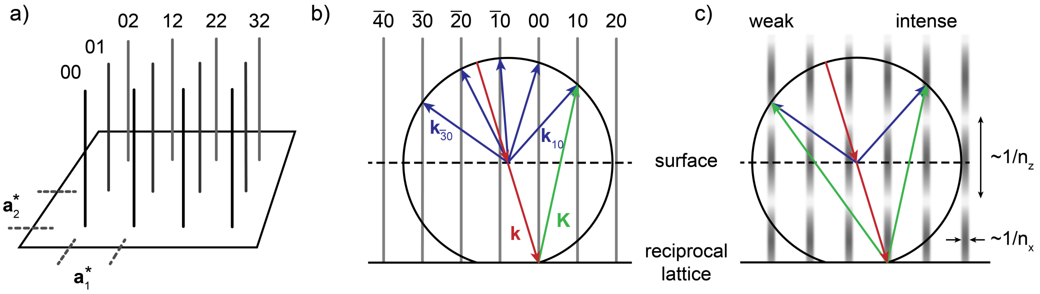

Figure 2.3: **a**, Rods characterizing the reciprocal lattice of a surface are identified by the Miller indices. **b**, Two-dimensional representation of the Ewald sphere construction visualizing the angles at which diffracted electrons are observed. **c**, A finite electron penetration depth leads to diffraction peaks of varying intensity. In the framework of the Ewald sphere this is caused by a modulation of the reciprocal lattice rods along the $\boldsymbol{a}_3^*$ direction.

Since the radius of the Ewald sphere is $|\boldsymbol{k}|$, it grows with higher electron energies, and more diffraction reflexes loom up. On the other hand, as the rods are continuously intersecting the sphere's surface, the diffraction condition remains fulfilled as long as $|\boldsymbol{k}|$ is bigger than the smallest possible reciprocal lattice vector $\boldsymbol{G}$.
In contrast, for diffraction at a bulk crystal, the well-defined and widely separated reciprocal lattice points have to coincide with the Ewald sphere. Hence, while probing thick samples with x-rays or high-energy electrons, it strongly depends on the incident wavelength or sample tilt angle, whether certain diffraction peaks can be observed at all.

Assuming the low-energy electrons to penetrate several atomic layers into the sample, the reciprocal lattice can be no longer described by uniform rods. In fact, the situation represents the transition to the previously described case of diffraction at the bulk. Then, analogous to the sharpening of the peaks in $\boldsymbol{a}_1^*$ and $\boldsymbol{a}_2^*$ direction with increasing M and N, as described in Eq. 2.4, the width of the intensity distribution along the rods is inversely proportional to the number of layers involved (Fig 2.3c). Hence, measurements with a variable kinetic energy of the incident electrons lead to oscillating diffraction spot intensities, depending on the intersections of the reciprocal lattice rods and the Ewald sphere, respectively.

Furthermore, the Ewald sphere construction directly emphasizes another advantage of LEED: For normal incidence, its diffraction patterns are inherently symmetric and equivalent spots emerge at the same energy.

2.1.5 Debye-Waller effect

In the previous considerations, all atoms were treated as static and deviations from a perfect crystal lattice were neglected. However, at room temperature, the atoms fluctuate around their equilibrium positions having an amplitude of up to 10 % of their lattice parameter [52].

Taking into account a variable local displacement $\boldsymbol{u}(t)$, the atomic positions then read $\boldsymbol{r}(t) = \boldsymbol{R}_{mn} + \boldsymbol{r}_j + \boldsymbol{u}(t)$, similar to Sec. 2.1.3. This includes the assumption that all atoms inside the unit cell are equally displaced. Then, to obtain the basis structure factor $|F|^2$ according to Eq. 2.2, the temporal average of $\boldsymbol{u}(t)$ has to be calculated [52], i.e.,

$$\begin{aligned} \langle F \rangle_t &= \left\langle \sum_{j=1}^{J} f_j \cdot \exp\left(i\boldsymbol{K}\left(\boldsymbol{r}_j + \boldsymbol{u}(t)\right)\right) \right\rangle_t && (2.10) \\ &= \sum_{j=1}^{J} f_j \cdot \exp\left(i\boldsymbol{K}\boldsymbol{r}_j\right) \cdot \langle \exp\left(i\boldsymbol{K}\boldsymbol{u}(t)\right) \rangle_t = F_{stat} \cdot \langle \exp\left(i\boldsymbol{K}\boldsymbol{u}(t)\right) \rangle_t \, . && (2.11) \end{aligned}$$

This may be simplified using the series expansion

$$\langle F \rangle_t = F_{stat} \cdot \langle \exp\left(i\boldsymbol{K}\boldsymbol{u}(t)\right) \rangle_t = F_{stat} \cdot \left[1 + \langle i\boldsymbol{K}\boldsymbol{u}(t) \rangle_t - \left\langle \frac{1}{2} \left(\boldsymbol{K}\boldsymbol{u}(t)\right)^2 \right\rangle_t + ... \right] . \quad (2.12)$$

Assuming that orientations of $\boldsymbol{K}$ and $\boldsymbol{u}(t)$ are uncorrelated over time, the second term yields $\langle i\boldsymbol{K}\boldsymbol{u}(t) \rangle_t = 0$. Moreover, using the angle γ between $\boldsymbol{K}$ and $\boldsymbol{u}(t)$ in the third term and averaging $\cos^2 \gamma$ over all possible directions leads to [52]

$$-\left\langle \frac{1}{2} \left(\boldsymbol{K}\boldsymbol{u}(t)\right)^2 \right\rangle_t = -\frac{1}{2} \left\langle K^2 u^2(t) \cos^2 \gamma(t) \right\rangle_t = -\frac{1}{6} K^2 \left\langle u^2(t) \right\rangle_t . \quad (2.13)$$

Accordingly, Eq. 2.12 may be written as

$$\langle F \rangle_t = F_{stat} \cdot \left[1 - \frac{1}{6} K^2 \left\langle u^2(t) \right\rangle_t + ... \right] \approx F_{stat} \cdot \exp\left(-\frac{1}{6} K^2 \left\langle u^2(t) \right\rangle_t \right) . \quad (2.14)$$

In terms of diffracted intensity, Eq. 2.14 then reads

$$I = I_0 \cdot \exp\left(-\frac{1}{3} K^2 \left\langle u^2(t) \right\rangle_t \right) , \quad (2.15)$$

in which the exponential suppression is commonly referred to as the *Debye-Waller factor*. Assuming the atoms to be harmonic oscillators, for small amplitudes the mean square displacement $\langle u^2(t)\rangle_t$ is directly proportional to the temperature T [52]. Using this approach, an alternative formulation of the Debye-Waller factor is

$$I = I_0 \cdot \exp\left(-\frac{k_B T}{m\omega^2} K^2\right) , \tag{2.16}$$

where ω denotes the oscillation frequency of the atoms having mass m. In this temperature-dependent suppression of the diffraction peak intensity, all electrons that get scattered out of the original diffraction peaks contribute to the increase of a homogeneous background. Correspondingly, to obtain a high-contrast diffraction pattern, low temperatures and small scattering vectors $\boldsymbol{K}$ are beneficial, which might be achieved either by using grazing incidence angles or small energies [49].

A more detailed description of the Debye-Waller effect taking into account the correct atomic oscillations given by the phonon dispersion relation would lead to a pronounced inelastic scattering in certain k-space directions. Such a modulation of the background intensity is studied in a time-resolved way in Refs. [53] and [54].

2.1.6 Experimental implementations of LEED

In general, there exist a multitude of different types of LEED systems customized to the requirements of the particular application (e.g., investigating molecular adsorbates, low-energy resonances or surface barrier effects) [6]. However, today, mainly two different implementations of LEED setups are commercially available:

In a conventional LEED setup a thermionic emitter (e.g., $\mathrm{LaB_6}$) produces a well-collimated and sufficiently monochromatic electron beam of desired energy, which is subsequently diffracted from a crystalline surface and detected on a hemispherical fluorescent screen. Beam currents of such electron sources typically vary between 10^{-8} A and 10^{-4} A [18]. After that, the resulting diffraction pattern can be recorded photo-optically through a viewport of the vacuum chamber from both sides of the screen. To prevent the inelastically scattered electrons from enhancing the background of the diffraction pattern, usually a retarding field energy filter is placed between the sample and screen. Commonly consisting out of four metal grids, the outer two grids of the energy filter are grounded, and the inner two are held on a potential close to the electron energy. The major advantage of this combination of a hemispherical screen and energy analyzer, which was proposed in 1962 by Lander *et al.* [44], is that the Ewald sphere is inherently represented by the experimental setup. Thus, by projecting the curved screen onto a photographic plane

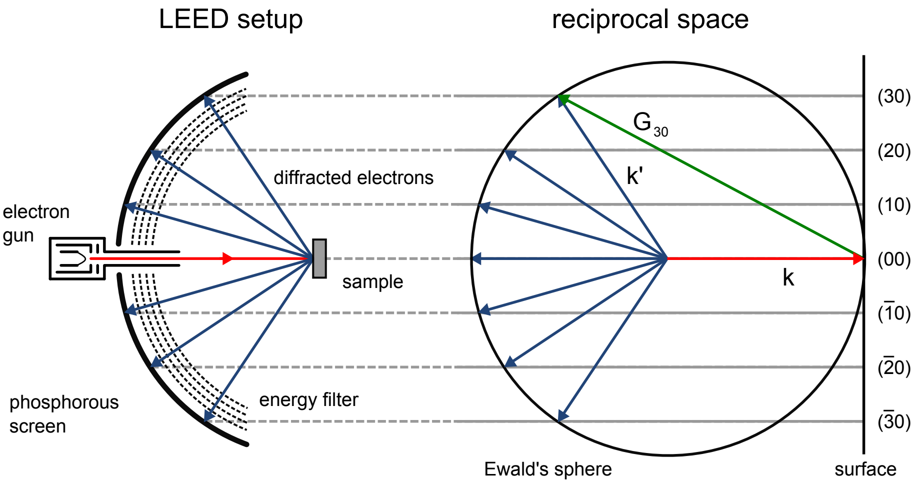

Figure 2.4: Schematic of a conventional LEED setup including the Ewald sphere construction of the resulting diffraction pattern with incident and scattered electrons shown in red and blue, respectively. Figure adapted from Ref. [55].

one directly obtains an undistorted image of the reciprocal lattice defined by the sample surface (Fig. 2.4). Furthermore, with suitable electronics, the energy filter allows for Auger-electron-spectroscopy (AES), which is very sensitive to the chemical composition of the surface, and therefore can be used to detect even very small amounts of surface contaminants or other adsorbates.

In a different implementation of LEED, the angles of the incident and diffracted electron beams are controlled by a set of octopole electrodes. The electrons diffracted in a direction close to the incident ones are detected by a channeltron with a small entrance slit (Fig. 2.5). To record a complete diffraction pattern, a large area of the surface's reciprocal lattice has to be scanned over the detector. Using an electrostatic entrance lens right before the sample, the electron crossover of the gun is imaged onto the channeltron. Compared to a conventional LEED system, this provides for a significantly higher k-space resolution and leads to transfer widths up to $w_t = 200$ nm [56, 57].

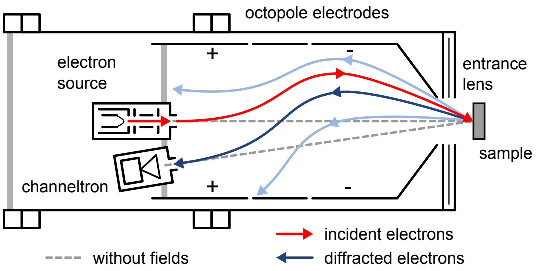

Figure 2.5: Schematic of a SPA-LEED system. Instead of using a spatially extended electron detector like a phosphorous screen, the reflected electrons are scanned across a channeltron electron multiplier to enhance the sensitivity and k-space resolution. Figure adapted from Ref. [58].

Hence, this instrument is suited to investigate the shape of individual diffraction peaks, giving rise to its name *spot profile analysis* (SPA) LEED [57]. A further difference to a conventional LEED system arises from the fact that the angle between $\boldsymbol{k}$ and $\boldsymbol{k}'$ remains constant, while the incident and scattered beams are simultaneously tilted with respect to the surface. This leads to a modified Ewald sphere, which features a radius of $G = k - k'$ instead of $2k$, as shown in Fig. 2.4. Additionally, SPA-LEED diffraction patterns intrinsically show the (00)-reflex, which is masked in a conventional LEED at normal incidence either by the gun or the sample itself.

In summary, depending on the desired quantity, LEED offers different ways of operation [49]: First, it can be used to obtain information about the overall surface symmetry, reconstruction, periodicity or lattice constants from the diffraction spot positions. In order to gauge the reciprocal lattice observed, it is necessary to either have a reference structure or precise knowledge about the dimensions of the setup and energy used.

Secondly, by thorough analysis of the peak shapes, LEED can be utilized to enlighten the surface morphology (e.g., roughness, steps, terraces), as well as to investigate possibly present domains or defect structures. This method is of particular interest for monitoring the deposition of thin films or other growth processes at surfaces, and it requires for a high transfer width.

Finally, LEED even allows for determination of the exact crystal structure of the surface, by measuring the energy-dependent intensity of a large number of diffraction peaks, so-called I-V-curves [59]. Then, using an iterative algorithm, the accurate atomic positions inside the surface unit cell are deduced by comparison with Fourier transforms of previously calculated structures.

2.1.7 Electron beam properties

Discussing characteristic properties of electron beams, a particular interest is to assess their suitability for diffraction and imaging. To this end, several quantities are employed as figure of merit throughout the literature, which will be briefly presented in the following paragraphs. Primarily, these measures vary by their point of view as they emanate from different core issues of the experiment, such as electron beam generation, propagation, sample interaction or diffraction pattern formation.

Emittance and brightness

To examine the beam quality of an electron bunch propagating in z-direction through an accelerator or microscope and having a finite energy spread ΔE, the ensemble of electrons is fully described by their positions $\boldsymbol{r}_i$ and momenta $\boldsymbol{p}_i$, which gives rise to a six-dimensional phase space. Neglecting Coulomb interaction, the momentum p_z can be assumed independent of p_x and p_y, effectively reducing the phase-space dimensions to four. Furthermore, if the electron bunch features rotational or ellipsoidal symmetry, it is sufficient to consider the 2D phase spaces (x, p_x) and (y, p_y) separately. Thus, the electron distribution in, e.g., (x, p_x) is evaluated by means of the so-called normalized root-mean-square (rms) *emittance*

$$\tilde{\varepsilon}_{n,x} = \frac{1}{m_e c}\sqrt{\langle x^2\rangle \langle p_x^2\rangle - \langle x p_x\rangle^2} \tag{2.17}$$

where the variances $\langle x^2\rangle$ and $\langle p^2\rangle$ denote the position and momentum spread, respectively, whereas the covariance term $\langle xp\rangle^2$ represents a correlation of x and p occurring after, for instance, being focused by a lens [60]. The normalized emittance $\tilde{\varepsilon}_n$ given by Eq. 2.17 already accounts for varying kinetic energies of the electron bunch[1]. If the applied optic system is linear, an area A_x enclosed by an isodensity contour in phase space is conserved during propagation of the electron bunch, as stated by Liouville's theorem [60, 61]. Nonlinear effects, such as lens aberrations, lead to filamentation of the phase space and are reflected by an increasing $\varepsilon_{n,rms}$ [60]. Accordingly, small values for $\tilde{\varepsilon}_n$ are favorable,

---

[1] Alternative definitions of the emittance use the so-called trace space (x, x') characterized by position x and divergence $x' = \mathrm{d}x/\mathrm{d}z \approx \alpha_x$ of the electrons, which leads to $\varepsilon_{rms} = \beta\gamma\sqrt{\langle x^2\rangle \langle x'^2\rangle - \langle xx'\rangle^2}$ with the velocity-dependent correction factors $\beta = v_e/c$ and $\gamma = 1/\sqrt{1-\beta^2}$.

giving rise to an ultimate quantum mechanical limit governed by Heisenberg's uncertainty principle

$$\sqrt{\langle x^2 \rangle}\sqrt{\langle p_x^2 \rangle} \geq \frac{\hbar}{2}\,, \tag{2.18}$$

which corresponds to [33]

$$\varepsilon_{qm} = \frac{\hbar}{2m_e c} \approx 0.19\,\mathrm{nm{\cdot}mrad}\,. \tag{2.19}$$

Generally, the emittance can be decreased down to ε_{qm} by cutting out electrons with high transversal momenta using apertures in the beam path. Hence, for a more meaningful figure of merit the number of electrons has to be taken into account.

To this end, the so-called source brightness B is introduced as [60, 61]

$$B = \frac{\mathrm{d}I}{\mathrm{d}A\mathrm{d}\Omega} \tag{2.20}$$

where $\mathrm{d}I$ is the electron current emitted from an area $\mathrm{d}A$ into the solid angle $\mathrm{d}\Omega$. Since this quantity may vary across the beam, an averaged brightness $\bar{B}_n$ normalized for different acceleration voltages can be defined using the previously introduced normalized rms emittances [60]

$$\bar{B}_n = \frac{I}{8\pi^2 \tilde{\varepsilon}_{n,x}^2 \tilde{\varepsilon}_{n,y}^2}\,. \tag{2.21}$$

To experimentally determine the emittances $\tilde{\varepsilon}_{n,x}$ and $\tilde{\varepsilon}_{n,y}$, a possible way is to measure the beam waist and divergence after a focusing element, i.e., the caustic of the respective electron beam [33].

Coherence

An important quantity of the instrument's spatial resolution in both light and electron optics is the coherence of the respective beam. It can be viewed as the degree of phase mismatch between two independent waves still giving rise to constructive interference. Due to the wave character of electrons, most of the concepts to quantify coherence initially developed for light optics can be directly transferred to electron beams. Typically, for all kinds of waves, the degree of coherence along the optical axis and perpendicular to it is considered separately, commonly named *longitudinal* and *transversal coherence*, respectively. Specifically, the former mainly depends on the monochromaticity $\Delta\lambda$ or energy spread ΔE of the electrons and thus accounts for the temporal phase relation between two co-propagating rays or electrons. It gives rise to a maximum longitudinal coherence length ξ_l, after which two waves of slightly varying wavelength $\lambda = h/p$ would be out of phase, defined as [62, 63]

$$\xi_l = \frac{\lambda^2}{\Delta\lambda} = \frac{v_e h}{\Delta E} \tag{2.22}$$

for non-relativistic electrons with velocity v_e.

The transversal coherence length ξ_t, on the other hand, limits the ability of two scattering sites separated by a distance d to constructively interfere with each other. Hence, if an electron wave interacts with a sample, only regions of diameter $d_{max} < \xi_t$ can cause a diffraction pattern, whereas larger areas just contribute via incoherent superposition.

For an incoherently emitting source of size L, this effect is nicely illustrated in a Young's double slit experiment, in which two holes separated by a distance d are illuminated by a source located at distance R from the slit.

As laid out in Ref. [64], this leads to the condition

$$\frac{dL}{R} \lesssim \frac{\lambda}{2}\,. \tag{2.23}$$

for the emergence of a diffraction pattern. Associating the maximum slit distance d_{max} with the transversal coherence length ξ_t and applying the small angle approximation $d/R = 2\tan(\alpha/2) \approx \alpha$, Eq. 2.23 then reads

$$\xi_t = \frac{\lambda}{2\alpha}\,. \tag{2.24}$$

Alternatively, ξ_t can be defined using the angular spread σ_α of the beam and an additional factor of π [65]

$$\xi_t = \frac{\lambda}{2\pi\sigma_\alpha}\,. \tag{2.25}$$

As a consequence, it is possible to express Eq. 2.24 in terms of the aforementioned normalized rms emittance $\tilde{\varepsilon}_{n,x}$. Since the correlation term in Eq. 2.17 vanishes at a beam waist, here, using the approximation $\sigma_\alpha = \sigma_{p_x}/p$ for the spread of the transversal momentum p_x, the correlation length is given by

$$\xi_t = \frac{\hbar}{m_e c} \cdot \frac{\sigma_x}{\tilde{\varepsilon}_{n,x}}\,. \tag{2.26}$$

Transfer width

A different approach to quantify the spatial resolution of a diffraction apparatus emanates from analysis of the resulting diffraction pattern. As discussed in Sec. 2.1.3, the intensity distribution $I\left(\boldsymbol{k}\right)$ caused by diffraction from a perfect crystal is given by Eq. 2.2. In a real experiment, however, $I\left(\boldsymbol{k}\right)$ is always affected by the so-called *instrument response function* $T\left(\boldsymbol{k}\right)$, which depends on a multitude of parameters, such as beam divergence, the type of electron detector or the photo-optical imaging system. Hence, $T\left(\boldsymbol{k}\right)$ effectively broadens the peaks of the measured signal $I_m\left(\boldsymbol{k}\right)$ via convolution [66]

$$I_m\left(\boldsymbol{k}\right) = I\left(\boldsymbol{k}\right) * T\left(\boldsymbol{k}\right) \ . \tag{2.27}$$

It is possible to show that the ultimate information encoded in a diffraction pattern is the autocorrelation or pair correlation function $\Phi\left(\boldsymbol{r}\right)$ of the diffracting surface, due to the loss of phase information [49, 67]. In the framework of the kinematic scattering theory, the latter is obtained via Fourier transformation of $I\left(\boldsymbol{k}\right)$, i.e.,

$$\mathcal{F}\left\{I\left(\boldsymbol{k}\right)\right\} = \Phi\left(\boldsymbol{r}\right) \ . \tag{2.28}$$

Using the convolution theorem, the Fourier transform of the measured intensity distribution $I_m\left(\boldsymbol{k}\right)$ can be expressed as the point-wise product of the pair correlation $\Phi\left(\boldsymbol{r}\right)$ and a function $\mathcal{F}\left\{T\left(\boldsymbol{k}\right)\right\} = t\left(\boldsymbol{r}\right)$:

$$\mathcal{F}\left\{I_m\left(\boldsymbol{k}\right)\right\} = \mathcal{F}\left\{I\left(\boldsymbol{k}\right) * T\left(\boldsymbol{k}\right)\right\} = \mathcal{F}\left\{I\left(\boldsymbol{k}\right)\right\} \cdot \mathcal{F}\left\{T\left(\boldsymbol{k}\right)\right\} = \Phi\left(\boldsymbol{r}\right) \cdot t\left(\boldsymbol{r}\right) \tag{2.29}$$

Commonly, $t\left(\boldsymbol{r}\right)$ is also referred to as the *transfer function* of the instrument and causes a modulation of the measured pair correlation function. Specifically, its finite width (the so-called *transfer width*) w_t defines a distance beyond which it becomes increasingly difficult to obtain meaningful information from the pair correlation function $\Phi\left(\boldsymbol{r}\right)$. The exact distance, however, strongly depends on the signal-to-noise ratio of the particular instrument or measurement conditions and can be significantly larger than w_t [68]. Determining w_t from a diffraction peak width via $w_t = 2\pi/w_p$ gives rise to the accuracy $a = \Delta w_p/w_p$. Then a is used to define the “maximum resolvable distance” $d_{max} = w_t/\sqrt{2a}$ [69]. As will be shown in the following section, for conventional imaging LEED systems, typical values of w_t range from 10 nm to 30 nm [66, 69].

2.2 Surface effects in electron diffraction

Due to its broken symmetry, the surface of a material exhibits a multitude of properties drastically differing from the bulk or exclusively present here. Prominent examples are modified band structures [3, 4], surface states [1, 2], as well as surface relaxation or the formation of reconstructions [17]. Since a variety of these phenomena has direct influence on the results obtained by diffractive methods, the ones important for the further considerations of this work will be briefly highlighted in the following section.

2.2.1 Surface reconstructions and superstructures

Cleaving a bulk crystal in vacuum creates two surfaces, in which the outermost atoms are lacking their former binding partner. Hence, a large number of dangling bonds is created, leading to a high surface free energy [17], which depends on the chemical composition of the bulk, the types of bonds involved, as well as the crystallographic direction of the truncation. Naturally, the surface aims to reduce this free energy by rearrangement of the outermost atoms, also termed *surface reconstruction*. This process may involve changes of the atomic density, dimerization of neighboring atoms, or, especially for semiconductors, depend on the temperature applied. Hence, for some materials it is possible to observe a variety of reconstructions of the same surface by varying annealing time or temperature.

There are two common ways to precisely describe a surface reconstruction. Both are employing the primitive basis vectors $\boldsymbol{a}_1$ and $\boldsymbol{a}_2$ of the bulk-truncated surface, as well as the basis vectors $\boldsymbol{b}_1$ and $\boldsymbol{b}_2$ of the reconstruction unit cell: In Wood's notation the reconstruction is defined by the aspect ratios $m = |\boldsymbol{b}_1| / |\boldsymbol{a}_1|$ and $n = |\boldsymbol{b}_2| / |\boldsymbol{a}_2|$ and a possible rotation angle φ of the reconstructed unit cell, which then reads $(m \times n)\,\mathrm{R}\varphi$ [48].

However, this approach fails if $\boldsymbol{b}_1$ and $\boldsymbol{b}_2$ are rotated by different angles. Then, it is more instructive to express $\boldsymbol{b}_i$ as a linear combination of the substrate basis vectors $\boldsymbol{a}_i$, which is done in the transfer matrix notation [6, 70]

$$\begin{pmatrix} \boldsymbol{b}_1 \\ \boldsymbol{b}_2 \end{pmatrix} = \begin{pmatrix} m_{11} & m_{12} \\ m_{21} & m_{22} \end{pmatrix} \begin{pmatrix} \boldsymbol{a}_1 \\ \boldsymbol{a}_2 \end{pmatrix} = M \begin{pmatrix} \boldsymbol{a}_1 \\ \boldsymbol{a}_2 \end{pmatrix} . \tag{2.30}$$

Both notations are not just valid for surface reconstructions, but can be applied to all kinds of superstructures, for example, formed by adsorbates or charge-density waves. In general, a surface superstructure does not necessarily have to be in registration with the underlying substrate lattice. For this reason, two cases are distinguished:

- For a *commensurate* superstructure, the edges of the substrate and superstructure unit cells periodically coincide at certain positions. Therefore, the elements of the transfer matrix m_{ij} are rational.
- A superstructure is *incommensurate* to the substrate if at least one element of the transfer matrix m_{ij} is irrational. Hence, its atoms are not in registration with the underlying lattice, giving rise to a continuously degenerate ground state.

In a diffraction experiment all relations regarding the surface, reconstructions or possible superstructures are mapped into reciprocal space. Utilizing the concept of reciprocal lattice vectors, as introduced in Sec. 2.1.3, a superstructure's reciprocal lattice unit cell is given by [6]

$$\begin{pmatrix} \boldsymbol{b}_1^* \\ \boldsymbol{b}_2^* \end{pmatrix} = M^* \begin{pmatrix} \boldsymbol{a}_1^* \\ \boldsymbol{a}_2^* \end{pmatrix} . \tag{2.31}$$

With the definition of $\boldsymbol{a}_i \boldsymbol{a}_j^* = 2\pi\delta_{ij}$ the Matrix M^* is derived via $M^* = 2\pi \left(M^T\right)^{-1}$ or explicitly

$$M^* = \begin{pmatrix} m_{11}^* & m_{12}^* \\ m_{21}^* & m_{22}^* \end{pmatrix} = \frac{2\pi}{\det(M)} \begin{pmatrix} m_{22} & -m_{21} \\ -m_{12} & m_{11} \end{pmatrix} , \tag{2.32}$$

which is equivalent to $M^T M^* = 2\pi I$ with I being the identity matrix [52].

Since $|\boldsymbol{b}_i| > |\boldsymbol{a}_i|$ holds well for most superstructures, the relation is inverse in reciprocal space. Hence, in a diffraction pattern of a reconstruction or superstructure, the Bragg peaks of the substrate lattice are decorated by satellite spots originating from the wider modulation of the topmost layer. In some cases this leads to ambiguity for the interpretation of diffraction patterns, and certain superstructures turn out it impossible to be distinguished solely by their diffraction patterns. For example, on a cubic substrate, a (2×1)-superstructure consisting of different domains rotated by 90° with respect to each other, can produce the same diffraction pattern as a (2×2)-superstructure by incoherent superposition. To resolve this problem, further experimental techniques are necessary, which combine surface sensitivity with high spatial resolution, such as STM or novel LEED sources allowing for extremely confined electron beams. However, this issue draws attention to the question of how diffraction patterns of surfaces are affected by domains of varying structure or size, which will be addressed in the following paragraph.

2.2.2 Domains and defect structures

Under certain conditions, domains of superstructures permit ambiguity in the analysis of the resulting diffraction pattern. This requires that the superstructure unit cell and rotated copies of it can resemble a different superstructure, and, in addition, multiple domains are illuminated by an electron beam which features a coherence length smaller than the size of the respective domains. Then the diffracted beams emanating from the respective domains add up incoherently producing a diffraction pattern, which possibly is indistinguishable from a larger superstructure.

However, if the coherence length of the incident beam becomes large compared to the domain size, it causes interference of the electrons diffracted by the individual domains, leading to a completely different result.

To understand this effect in more detail, it is instructive to consider a 1D surface covered with N_2 equally spaced identical domains consisting of N_1 atoms (Fig. 2.6). The lattice parameter inside one domain is defined as $\boldsymbol{a}$ and the translation of neighboring domains $\boldsymbol{b} = (N_1 + g)\,\boldsymbol{a}$, where g determines the size of the gap in multiples of $\boldsymbol{a}$. Hence, the adjacent domains feature a constant phase mismatch φ_g, and for $g \bmod a = 0.5$ the gaps are also referred to as *antiphase boundaries* [49]. This type of superstructure can be directly interpreted as a lattice of domains, in which the domain itself serves as the lattice basis.

Hence, analogous to Eq. 2.2 and 2.4, the intensity I of the diffraction pattern is given by the product of two Fourier-transforms. The factor

$$|F|^2 = \frac{\sin\left(\frac{N_1}{2} \cdot \boldsymbol{Ka}\right)^2}{\sin\left(\frac{1}{2} \cdot \boldsymbol{Ka}\right)^2} \tag{2.33}$$

corresponds to the diffracted intensity of one domain with N_1 atoms, whereas the lattice

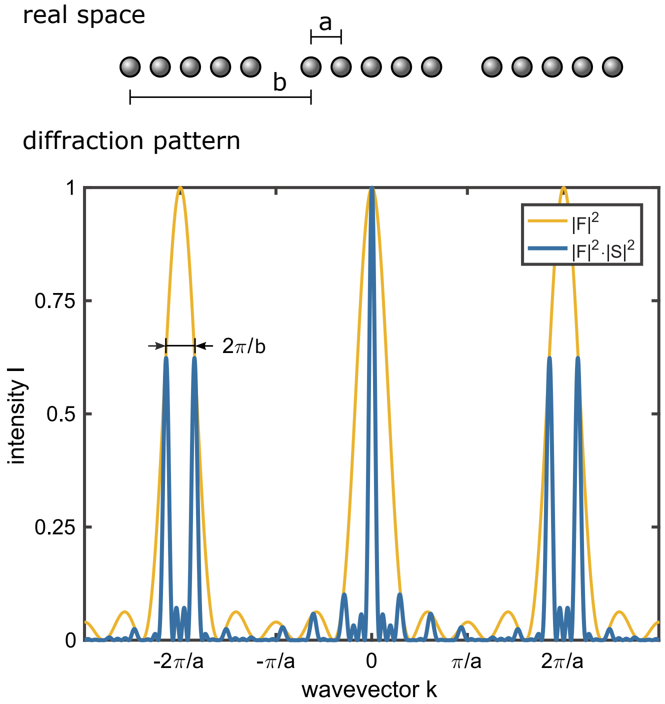

Figure 2.6: Diffraction spot splitting caused by antiphase domain boundaries. Yellow curve: Diffraction of a single domain consisting of $N_1 = 5$ atoms. Blue curve: Interference of $N_2 = 4$ domains with $g = 1.5$.

of domains is represented by the structure factor

$$|S|^2 = \frac{\sin\left(\frac{N_2}{2} \cdot \boldsymbol{K}\boldsymbol{b}\right)^2}{\sin\left(\frac{1}{2} \cdot \boldsymbol{K}\boldsymbol{b}\right)^2}\,, \tag{2.34}$$

giving rise to $I \propto |F|^2 \cdot |S|^2$ as depicted for exemplary values in Fig. 2.6. Using this formalism, the spacing between the two components of a split up diffraction spot is readily attributed to the distance $\boldsymbol{b}$ between two adjacent domains. Thus, in a more generalized view, every $\Delta\boldsymbol{K}$ between two arbitrary peaks in a diffraction pattern corresponds to a maximum of the pair correlation function $\Phi(\boldsymbol{r})$ of the surface, namely, a frequently found distance vector $\boldsymbol{d}$ between similar sites of the lattice, which are connected via $\Delta\boldsymbol{K} \cdot \boldsymbol{d} = 2\pi n$ [49].

However, one has to be careful, attributing the distances extracted from a LEED pattern to actual periodicities, since the information contained in the diffraction peaks resembles averaged quantities. Regarding the splitting of diffraction spots, this means that their distance $\Delta\boldsymbol{K}$ just corresponds to a mean domain spacing $\boldsymbol{b}$, and even a very similar diffraction pattern may be observed even for a relatively broad distribution of domain sizes, as shown in Ref. [67].

The phenomenon of split up diffraction spots can be observed at the room-temperature phase of the layered compound 1T-TaS_2, which is of particular interest later in this work and which will be described in more detail in Chap. 3.

Besides regular deviations from a perfect single crystalline surface structure, numerous kinds of disordered defects have large impact on the diffraction pattern formation, as well. Due to the lack of periodicity, usually they do not cause any diffraction spot splitting, but rather influence the shape of the diffraction peaks observed. Examples for such defects may be lattice impurities, mobile adsorbates, edge- or screw-dislocations, as well as distributions of terraces or domain sizes. In a simple approximation, the positions of such defects may be modeled by a Markovian distribution [71]. Here, while preceding from one atom to the next on a 1D surface, the probability to come across a defect after each step is defined as γ. Consequently, the probability $P\left(N\right)$ to find a domain boundary after N steps is determined by the geometric distribution [49]

$$P\left(N\right) = \gamma\left(1-\gamma\right)^{N-1} \, , \tag{2.35}$$

leading to an average defect spacing of $1/\gamma$. Considering the continuous average over the whole surface, this leads to an exponentially distributed pair-correlation function, which in turn results in a Lorentzian diffraction spot profile by Fourier transformation [49, 71]. If several types of defects are present at surface simultaneously, their influences on the diffraction peak profiles have to be examined separately. Subsequently, the overall signal is obtained by convolution of the ensuing line shapes. In the particular case of various Lorentzian profiles, the convolution again is a Lorentzian whose width is simply given by the sum of the widths of the respective contributions [71].

2.3 Charge-density waves in solids

Independently proposed in the 1950s by Peierls and Fröhlich [72, 73], charge-density waves (CDW) embody a static or "frozen-in" modulation of the conduction electrons in a solid. However, it took roughly twenty years from the theoretical prediction until their first experimental observation by Monceau *et al.*[2] in NbSe$_3$ [75]. In general, dimensionality plays a crucial role for the appearance of CDWs, becoming more likely for low-dimensional systems. Hence, the majority of CDW effects is observed in quasi one- or two-dimensional compounds, such as Indium nanowires or the class of transition metal dichalcogenides, respectively [28, 76, 77]. Although their emergence in one-dimensional systems is relatively well understood, CDW formation in more complex materials is still subject of ongoing research and comprehensive theories giving quantitative predictions of their properties have not been established yet [8].
In the 1D case, a CDW may be described as a spatially varying charge density

$$\varrho\left(\boldsymbol{r}\right) = \varrho_0\left(1 + \varrho_1 \cos\left(\boldsymbol{q}\boldsymbol{r} + \varphi\right)\right) , \tag{2.36}$$

with ϱ_0 being the original, unperturbed electron density, whereas ϱ_1, $\boldsymbol{q}$ and φ denote the amplitude, wavevector and an arbitrary phase of the charge-density modulation, respectively [8]. As a consequence, the atomic cores located at multiples of the lattice parameter na react the modified charge landscape by moving a small distance δa towards the centers of negative charge accumulation, resulting in a periodic lattice distortion (PLD).

In the Landau theory of phase transitions, the system is described in terms of an order parameter [78]. For a material exhibiting a CDW, the natural order parameter is the conduction electron density modulation $\alpha\left(\boldsymbol{r}\right) = \varrho_1 \cos\left(\boldsymbol{q}\boldsymbol{r} + \varphi\right)$ [79]. However, for numerous applications it is more straightforward to use a complex order parameter $\psi\left(r\right) \propto A \cdot \exp\left(i\boldsymbol{q}\boldsymbol{r}\right)$ with the charge-density modulation being $\alpha\left(\boldsymbol{r}\right) = \mathrm{Re}\left[\psi\left(\boldsymbol{r}\right)\right]$ [79]. This notation immediately pays off by considering a planar CDW system: In two dimensions the charge-density modulation typically is no longer a plane wave but features hexagonal symmetry. This system is conveniently described in terms of a triple CDW, i.e., the superposition of three plane waves $\psi_j\left(\boldsymbol{r}\right)$, $j = 1, 2, 3$ with wavevectors q_j rotated by 120° with respect to each other. The resulting charge modulation is given

---

[2] Actually, in their first publication Monceau *et al.* interpreted the observed anomalous transport properties in terms of single electron Zener-tunneling. Yet, another year later, Ong and Monceau came up with the suggestion for charge transport mediated by sliding CDWs to be responsible for the unexpected behavior of NbSe$_3$ [74].

by $\alpha(\boldsymbol{r}) = \mathrm{Re}\left[\psi_1(\boldsymbol{r}) + \psi_2(\boldsymbol{r}) + \psi_3(\boldsymbol{r})\right]$ [79]. In order to obtain rotationally-symmetric charge accumulations, it is important to note that the phases $\varphi_j(\boldsymbol{r})$ of $\psi_j(\boldsymbol{r})$ are not independent, but have to add up to zero (or multiples of 2π), i.e.,

$$\sum_{j=1,2,3} \varphi_j(\boldsymbol{r}) = 2\pi n \text{ with } n \in \mathbb{Z}. \tag{2.37}$$

2.3.1 Peierls instability and Fermi surface nesting

An intuitive approach to qualitatively understand the interplay of CDWs with the distorted arrangement of lattice atoms is the Peierls-model for a one-dimensional atomic chain. Considering the linear distribution of hydrogen-like atoms at distances a, this leads to a typical tight-binding dispersion relation for the electronic states $E(k)$, i.e., the band structure

$$E(k) = -E_F \cos(ka) \,. \tag{2.38}$$

Since $E(k)$ is exactly half filled, this example represents the band structure of a 1D metal with occupied states up to E_F at the Fermi-wavevector k_F (Fig 2.7). In fact, as Peierls and Fröhlich showed, this system turns out to be unstable against slight distortions δa, which would double the size of the unit cell from a to $2a$ [72, 73]. This causes the boundaries of the first Brillouin zone (BZ) to shift from π/a to $\pi/2a = k_F$. As a consequence, the formerly continuous band splits up at the new boundary of the 1st BZ, i.e., k_F. The resulting band gap of width $2\Delta E$ correspondingly lowers the energy of the occupied states in its vicinity (Fig 2.7b), and, hence, the system transforms from a 1D metal to a semiconductor.

However, for this transition to be stable, the electronic energy gain δE_e has to compensate for the elastic energy δE_l needed to periodically distort the atomic lattice, and a simple stability criterion reads $\delta E_e + \delta E_l < 0$ [8]. Finally, the displaced atoms cause a modulation of the charge density along the chain (depicted in blue in Fig 2.7b), which has a wavelength of $\lambda_{CDW} = \pi/k_F$. However, it remains a rather philosophical question, whether the displaced atoms give rise to the charge modulation, or if the locally increased electron densities itself serve as a driver for the lattice distortion. Still, it is worth noting that both CDW and PLD are inherently linked processes, which invariably occur at the same time.

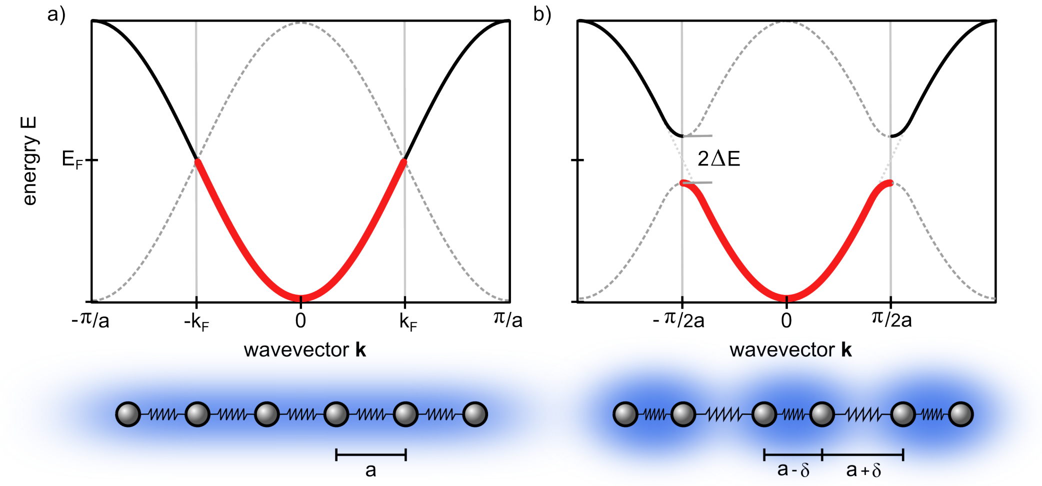

Figure 2.7: Peierls instability of a 1D metal. **a**, Half-filled band structure of an undistorted one dimensional atomic chain. Occupied states shown in red. **b**, Splitting of the band structure at $\boldsymbol{k}_F$ induced by a doubled periodicity of $2a$ leading to an electronic energy gain of ΔE. The modulated charge density of the atomic chain is illustrated in blue. Dashed lines indicate the band structure folded back to the first Brillouin zone.

In a more thorough treatment, based on the Fröhlich Hamiltonian [80], the phonon mode $\boldsymbol{q}$ causes a displacement $u(\boldsymbol{q})$ of the ionic cores with mass m, which leads to a potential

$$V(\boldsymbol{q}) = g(\boldsymbol{q})\, u(\boldsymbol{q}) \sqrt{\frac{2m\omega(\boldsymbol{q})}{\hbar}}, \tag{2.39}$$

where $g(\boldsymbol{q})$ and $\omega(\boldsymbol{q})$ denote the electron-phonon coupling constant and the frequency of phonon mode $\boldsymbol{q}$, respectively [8]. The electronic energy gain δE_e and distortion energy of the lattice δE_l can be expressed as

$$\delta E_l = \frac{m\omega^2 u^2}{2} \quad \text{and} \quad \delta E_e = |V(\boldsymbol{q})|^2 \chi_0(\boldsymbol{q}) \tag{2.40}$$

with the non-interacting electronic susceptibility $\chi_0(\boldsymbol{q})$, which is the response of the system to weak perturbations. Using Eq. 2.39 and 2.40, the aforementioned stability criterion reads

$$\frac{4g^2}{\hbar\omega} > \frac{1}{\chi_0(\boldsymbol{q})}. \tag{2.41}$$

Accordingly, a strong electron-phonon coupling constant $g(\boldsymbol{q})$ as well as a large electronic susceptibility $\chi_0(\boldsymbol{q})$ are vital prerequisites for CDW formation.

The term $\chi_0(\boldsymbol{q})$ is also known as the *Lindhard response function*, which in the 1D case of non-interacting electrons is defined as [8]

$$\chi_0(\boldsymbol{q}) = \frac{1}{L} \sum_{1st\, BZ} \frac{f(\boldsymbol{k}, 0) - f(\boldsymbol{k}+\boldsymbol{q}, 0)}{E(\boldsymbol{k}) - E(\boldsymbol{k}+\boldsymbol{q})}, \tag{2.42}$$

with L being the length of the atomic chain, $E(\boldsymbol{k})$ the energy of state $\boldsymbol{k}$, and the Fermi-Dirac distribution

$$f(\boldsymbol{k}, T) = \left(\exp\left(\frac{E(\boldsymbol{k}) - \mu}{k_B T}\right) + 1\right)^{-1}. \tag{2.43}$$

From Eq. 2.42 it directly follows that $\chi_0(\boldsymbol{q})$ becomes large if many electrons are scattered from an occupied to an unoccupied state (e.g., $f(\boldsymbol{k}, 0) = 1$ and $f(\boldsymbol{k}+\boldsymbol{q}, 0) = 0$ or vice versa), and if the energy difference $E(\boldsymbol{k}) - E(\boldsymbol{k}+\boldsymbol{q})$ is small. Both conditions are fulfilled right at the Fermi edge, which means that the electronic susceptibility $\chi_0(\boldsymbol{q})$ diverges for $\boldsymbol{q} = 2\boldsymbol{k}_F$. Hence, at this phonon wavevector, the participating electrons are scattered either from $-\boldsymbol{k}_F$ to $\boldsymbol{k}_F$ or in the opposite direction, which is also known as “umklapp-process”, a terminology coined by Peierls in his seminal work [73].

Explicitly calculating the electronic susceptibility $\chi_0(\boldsymbol{q})$ for a one-, two- or three-dimensional electron gas at $T = 0$ leads to the following proportionalities [81–83]:

$$\chi_{1D}(\boldsymbol{q}) \propto \frac{k_F}{q} \ln\left|\frac{2k_F + q}{2k_F - q}\right| \tag{2.44}$$

$$\chi_{2D}(\boldsymbol{q}) \propto \begin{cases} 1 & \text{for } q < k_F \\ 1 - \sqrt{1 - (2k_F/q)^2} & \text{for } q > k_F \end{cases} \tag{2.45}$$

$$\chi_{3D}(\boldsymbol{q}) \propto 1 + \frac{k_F}{q}\left(1 - \left(\frac{q}{2k_F}\right)^2\right) \ln\left|\frac{2k_F + q}{2k_F - q}\right|. \tag{2.46}$$

As can be seen from Fig. 2.8a, $\chi_{1D}(\boldsymbol{q})$ diverges logarithmically at $\boldsymbol{q} = 2\boldsymbol{k}_F$, whereas the higher-dimensional representations remain continuous. This is explained by the fact that the electronic susceptibility increases with the number of electrons involved in the “umklapp” scattering. Thus, it also depends on the topology of the Fermi surface, or, more precisely, on how many states with energy E_F can be connected by parallel wavevectors $\boldsymbol{q} = 2\boldsymbol{k}_F$. This requirement is referred to as *Fermi surface nesting*. Since a 1D metal features a Fermi surface simply consisting of two points (or planes), it corresponds to the perfect nesting condition causing the response function to diverge (Fig. 2.8b).

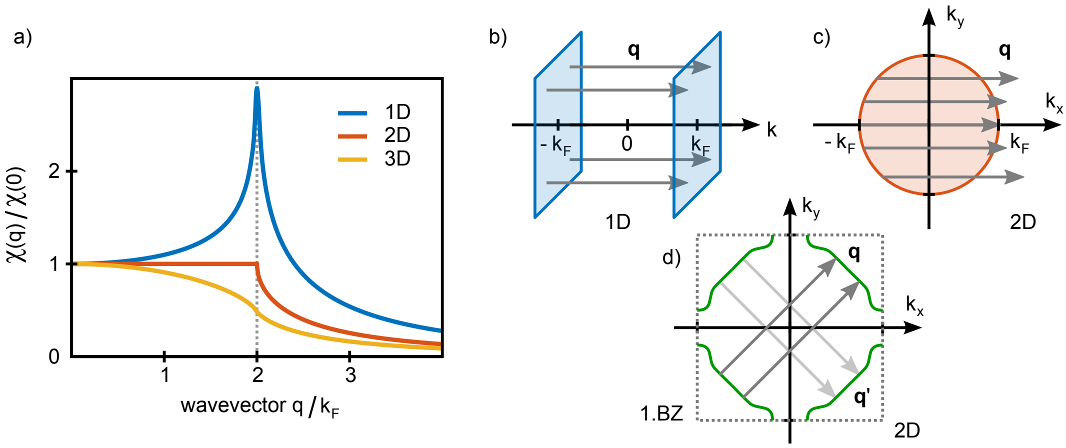

Figure 2.8: **a**, Electronic susceptibility $\chi\left(\boldsymbol{q},T\right)$ at $T=0$ for a one-, two- and three-dimensional electron gas. **b** and **c**, Efficiency of Fermi surface nesting illustrated for the one- and two-dimensional electron gas of panel **a**. **d**, Fermi surface of an exemplary 2D metal unstable against periodic lattice distortions in directions $\boldsymbol{q}$ and $\boldsymbol{q}'$.

However, in 2D or 3D, the percentage of equal wavevectors $\boldsymbol{q}$ connecting two points at the Fermi edge decreases compared to the number of states available. Hence, in principle, Fermi surfaces featuring large parallel regions are promising candidates to exhibit Peierls instabilities by fulfilling the nesting condition. Accordingly, CDWs are rarely found in materials, which do not show at least one strong lattice anisotropy, but are a prominent phenomenon in one-dimensional metals or other quasi two-dimensional materials [77, 84].

Note that, in general, $\chi\left(\boldsymbol{q},T\right)$ is temperature-dependent (cf. Eq. 2.42) due to the Fermi distribution $f\left(\boldsymbol{k},T\right)$. Hence, a finite temperatures T the sharp edge at E_F is smeared out attenuating the singularity of $\chi_{1D}\left(\boldsymbol{q},0\right)$ at $\boldsymbol{q}=2\boldsymbol{k}_F$.

2.3.2 Kohn anomaly

In the previous paragraph it was shown that both the Peierls instability and the associated CDW are intrinsically linked to a periodic modulation of the atomic lattice. An alternative way to understand the formation a PLD is to consider it as a "static" or "frozen" phonon with wavelength $\lambda_{CDW} = \pi/k_F$ and frequency $\omega = 0$. Hence, at a critical temperature T_c, indicating the transition to the CDW state, the first derivative of the phonon dispersion relation $\omega\left(\boldsymbol{q}\right)$ becomes singular at $q = 2k_F$. However, even at temperatures $T > T_c$ the frequencies of phonon modes in the vicinity of $2k_F$ are substantially lowered, a process commonly referred to as "phonon softening" [77]. This effect leading to a dip in the phonon dispersion relation can be considered as a high temperature precursor of a CDW phase transition or Peierls instability, respectively [77].
From a theoretical point of view, the phonon dispersion relation $\tilde{\omega}\left(\boldsymbol{q}\right)$ of a 1D metal can be derived again using the Fröhlich Hamiltonian [80]. As a result, $\omega\left(\boldsymbol{q}\right)$ - the phonon dispersion relation without electron-lattice interaction - is renormalized to [8]

$$\tilde{\omega}^2 = \omega^2 \left(1 - \frac{4g^2}{\hbar\omega}\chi\left(\boldsymbol{q}, T\right)\right) \tag{2.47}$$

including the temperature-dependent electron susceptibility. Figure 2.9 shows the emerging singularity in $\tilde{\omega}\left(\boldsymbol{q}\right)$ for a set of different temperatures above T_c (with $T_1 > T_2 > T_c$). Back in 1959, Walter Kohn was the first to predict this anomalous behavior or kinks in the vibrational spectrum of a metal [83], giving the *Kohn anomaly* its name. Likewise, he pointed out the close relationship between the phonon dispersion relation and the Fermi surface via the aforementioned nesting vectors. Since at that time experimentalists were lacking methods to spatially quantify the electronic band structure, such as

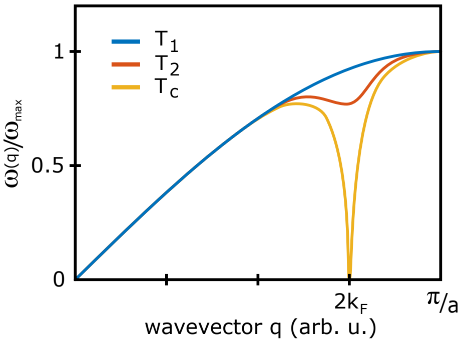

Figure 2.9: Illustration of the Kohn anomaly for different temperatures. While approaching T_c, a kink appears at $q = 2k_F$ in the the phonon dispersion relation, leading to $\omega\left(2k_F\right) = 0$ for the CDW transition temperature T_c.

ARPES, measuring Kohn anomalies turned out an elegant but time-consuming approach to indirectly map a Fermi surface. However, the results of early experiments conducted at lead and aluminum [85, 86] are in good agreement with modern findings.

2.3.3 Electron correlation effects

So far, the appearance of CDWs has been considered as an effect solely mediated by electron-phonon coupling. This is a justified approximation if the conduction electrons are well delocalized and Coulomb repulsion can be neglected. Though, it does not apply for materials, in which electron-electron interactions have notable contribution to the formation of CDWs and drastically affect the conductivity or band structure. Therefore, it is instructive to consider weak and strong-coupling CDWs separately, and to point out the differences between both approaches for modeling CDWs, as well as the varying properties associated with their formation mechanism [87]:

As already stated above, in the *weak coupling limit* CDWs are mainly Fermi surface driven. By fulfilling the nesting condition, the presence of a sufficient number of vectors $q = 2k_F$ simultaneously leads to a lattice distortion and lowers the electronic energy of the system. Since the amplitude of the resulting PLD is relatively small, it likewise corresponds to small energy gap at k_F in the band structure. Furthermore, generally, the length of k_F is not restricted to a multiple of the lattice parameter a, as it just depends on the topology of the Fermi surface. Thus, in most cases the wavelength λ_{CDW} is incommensurate to the underlying atomic lattice, and it can be shifted by an arbitrary phase φ with respect to the underlying lattice without changing its energy. For this reason, IC CDWs were suspected for superconductivity by Fröhlich in 1954 [72]. However, in his calculations he neglected CDW pinning to lattice impurities, which results in a finite resistivity.

On the contrary, in the setting of the *strong coupling limit* the electrons are localized at the atom positions and their Coulomb repulsion plays an important role. Now the interaction of atoms at adjacent lattice sites can be rather viewed in terms of chemical bonding [87]. Hence, the distortion amplitude is markedly bigger than in the case of weak coupling, leading to large energy gaps, which spread the electronic gain over a wide region of the 1. BZ [8]. As a result, for a strong coupling CDW, the texture of the host lattice is often characterized by well confined clusters causing λ_{CDW} to be commensurate or “in registration” with the atomic lattice. In turn, the pronounced deformation requires a larger number of phonon modes to contribute to the distortion, which likewise has influence on the thermodynamics of the system. In the strong coupling limit, it is primarily the thermal disordering of the lattice which increases the entropy, whereas, for a weak coupling CDW with a small energy gap at k_F, the temperature induced disorder is mainly of electronic nature, i.e., electron-hole pair excitation [8].

Moreover, if the electrons are no longer delocalized but confined to the lattice sites, it depends on Coulomb energy U_c and distance of the atoms, whether the electrons are able to move across the lattice. Hence, with stronger electron localization the DOS at the Fermi edge decreases forcing the conduction band to split up in a occupied lower and unoccupied upper Hubbard band [77]. This is also referred to as a *Mott-transition* postulated by N. F. Mott in 1949 [88]. It explains why some materials that are supposed to behave like a metal in a tight-binding approach, in fact, turn out to be insulators.

In general, a Mott-transition does not necessarily involve the formation of a CDW. However, the pronounced lattice deformation of CDWs in the strong coupling limit reduces the overlap of atomic orbitals, possibly leading to Mott-insulating behavior. In fact, this is the case for the low-temperature phase of 1T-TaS$_2$, which will be considered in more detail in Sec. 3.1 of this work.

2.3.4 CDW fluctuation modes

Following the emergence of a CDW in a suitable material, the periodic electron density modulation may be also viewed as a lattice of charge accumulations. Therefore, analogous to the underlying atomic lattice, the CDW itself can serve as a host of bosonic excitations. As described by Overhauser and McMillan, these fluctuation modes involve either a time-dependent variation of the CDW amplitude $\varrho_1(t)$ or a phase shift $\varphi(t)$ (cf. Eq. 2.36) [79, 89]. Since both types of collective excitations have a discrete energy spectrum $\omega(q)$, they are referred to as *amplitudons* and *phasons*, respectively. Their oscillatory behavior is sketched in Fig. 2.10, and it can be seen that the fluctuations of both modes correspond to the CDW equivalent of optical and acoustic phonon modes [81].

Usually phasons are considered “soft” excitations, since their energy is relatively small. However, this is primarily true for incommensurate CDW systems, in which charge accumulations can slide freely across the lattice. On the contrary, in a commensurate system phasons become “rigid”, since the CDW is locked to the arrangement of atomic clusters [81].

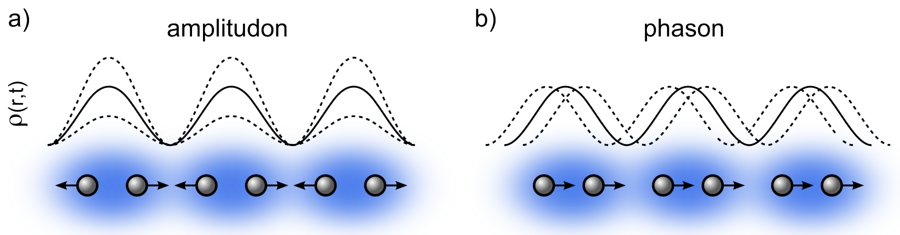

Figure 2.10: Sketch of 1D CDW fluctuation modes. **a**, Oscillating amplitude $\varrho_1(t)$ of the charge-density modulation (amplitudon). **b**, Time-dependent modulation of the CDW phase $\phi(t)$ with respect to a given ground state (phason).

As phasons involve a shift of the charge lattice with respect to ion cores, this mode turns out to be infrared active. Amplitudons, on the other hand, comprise a charge redistribution in each atomic cluster and, therefore, are Raman active [80]. Accordingly, the phason mode with $q = 0$ corresponds to charge transport mediated by the CDW, which can be observed by applying a DC field strong enough to overcome the CDW pinning.

Due to their analogy to phonons, in a diffraction experiment phasons manifest themselves in an additional contribution to the Debye-Waller effect of the atomic lattice, which only acts on the CDW diffraction peaks, as experimentally verified by Chapman *et al.* by means of x-ray diffraction [90]. Hence, by comparing the relative suppression of atomic lattice and CDW diffraction spots at elevated temperatures, the phasonic contribution can be separated [91].

2.4 Topological defects and dislocations

From a general perspective, the mathematical field of algebraic topology deals with the properties of paths or geometrical objects that are conserved under so-called continuous transformations. These include modifications such as shearing, stretching, compression, bending or crumpling. Objects which can be transformed from one to another like this are considered topologically equivalent or homeomorphic [92]. In a simple geometric view, this refers to the number of holes in the specific object, the so-called *genus*. Accordingly, a donut and a mug belong to the same topological class (homotopy), as well as a pair of scissors and a bag with two handles.

Topology has a wide range of applicability to numerous aspects of condensed matter physics. For example, it may be used to describe real-space structures, such as defects in periodic arrangements, or it allows for predicting anomalous conductivity phenomena from the topology of the band structure, as it is the case for topological insulators [14, 15]. In 1973, Michael Kosterlitz and David Thouless employed topological defects to predict a new class of phase transitions in ordered media [10]. Together with Duncan Haldane, their works paved the way for a multitude of effects that can be now explained within the framework of topological order. For this achievement, all three of them were awarded with the 2016 Nobel prize in physics [93].

Focusing on topological defects, these can be understood as a singularity of the order parameter in systems with a broken continuous symmetry. To identify and classify them, first an order-parameter of the system has to be defined, which is subsequently analyzed by traversing around the suspected defect on a closed contour [92, 94]. This course of action will be described in more detail in the next paragraph, followed by an illustration of the significance for CDWs.

Depending on the particular subject of research, the terminology of topological defects can differ. For instance, in superfluid Helium or spin structures they appear as vortices [95, 96], whereas in crystal structures they are referred to as dislocations and disclinations [97]. However, in all cases, the methods forming the basis of their description in terms of topology are the same, as will be laid out in the following by means of two examples.

2.4.1 Classification of topological defects

A simple model to introduce topological defects are spins $s\left(x,y\right)$ in a two-dimensional plane. In a field of unit vectors, each spin is completely characterized by the angle $\vartheta\left(x,y\right)$,

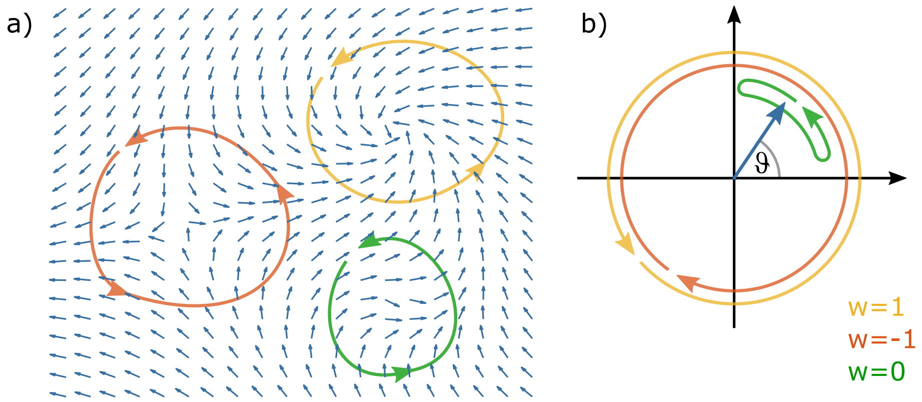

Figure 2.11: Characterization of topological defects in terms of a winding number w. **a,** Real-space representation of spins in a 2D lattice featuring two dislocation defects. **b**, To categorize these defects, the spin directions on an arbitrarily shaped loop around each defect are mapped into order-parameter space by a parametric transformation with respect to the path distance.

which is therefore chosen as the order parameter. Accordingly, the order-parameter space is given by a circle, on which each spin $s(x,y)$ is represented by a point. If we now consider perturbations from a totally uniform vector field, a possible way to characterize the distortions is choosing an arbitrarily shaped closed contour around an area A in the 2D plane and integrating over the order parameter while traversing the loop in a counterclockwise fashion [92]. The implications of this procedure are emphasized by mapping the traced contour into order-parameter space (Fig. 2.11). Since the contour is a loop in real space, it corresponds to a closed path on the circle. Therefore, integration over the order parameter ϑ complies with the number of revolutions the mapping wraps the loop around the circle in order-parameter space. Hence, the integral over ϑ can only yield $2\pi \cdot w$, with $w \in \mathbb{Z}$ being the so-called *winding number* of a defect [92].

It can be easily seen that the vector field $s(\boldsymbol{r})$ actually exhibits a defect in the enclosed space A with $w \neq 0$ by successively shrinking the contour. In the limit $A \rightarrow 0$ the gradient of the vector field will diverge, giving rise to a singularity in $s(\boldsymbol{r})$, at which the order parameter is not well defined anymore [97]. This distinct point is called a *topological defect* or topologically protected state, since it is conserved under the aforementioned continuous deformations of the vector field[3]. Similarly, these transformations can be applied to the mappings from real space to order-parameter space: All contours are called homotopic if they lead to the same integral value. Thus, the green loop with $w = 0$ in Fig. 2.11b is homotopic to a single point on the circle, or, alternatively, to a region of

---

[3] For this reason, a possible application of topological states could be their use as "qubits" for a fault-tolerant quantum computer, as suggested by Alexei Kitaev [98].

uniformly directed spins. To this end, perturbations of $s(\boldsymbol{r})$ with $w = 0$ (green curve in Fig. 2.11a) are considered topologically unstable and can flatten out by themselves. This is in contrast to defects with $w \neq 0$, which are inherently stable entities, and need a defect with opposite winding number nearby to allow for an unperturbed vector field at a sufficient distance. An example for this situation is the contour which includes the whole vector field displayed in Fig. 2.11a. The two defects with winding numbers $w = 1$ and $w = -1$ neutralize, and on the edge of the displayed vector field, its singularities are not discernible anymore. For this reason, a path with $w = 0$ may include either no topological defects or a compensating number of defects having opposite winding numbers. Thus, the contour to identify topologically protected states should generally be chosen as small as possible.

It is worth noting that the same winding number w can be obtained for very different vector field distributions. For instance, by using polar coordinates $\boldsymbol{r} = (r, \phi)$, one can construct the field $s(\vartheta(\boldsymbol{r})) = w\phi + \alpha$ with winding number w and an overall tilt angle of the spins α [97]. Then the offset angle α has no influence on w, since it just implies a rotation of the circle in order-parameter space. To illustrate this fact, some exemplary fields with varying α are shown in Fig. 2.12. Accordingly, sources and drains of a vector field belong to the same topological class, and they require defects of opposite winding number to neutralize them.

In a second example, topological defects in a 2D cubic crystal lattice are analyzed using the previously introduced concept. Here, the order parameter is the displacement $\boldsymbol{u}(x, y)$ of the atoms for any distortions from the perfectly aligned lattice [94]. Due to broken translational symmetry of the lattice, the order-parameter space is a square with periodic boundary conditions, which is topologically equal to a torus (Fig. 2.13). If we now consider a part of the lattice distorted by an extra row of atoms, we can study the induced perturbation

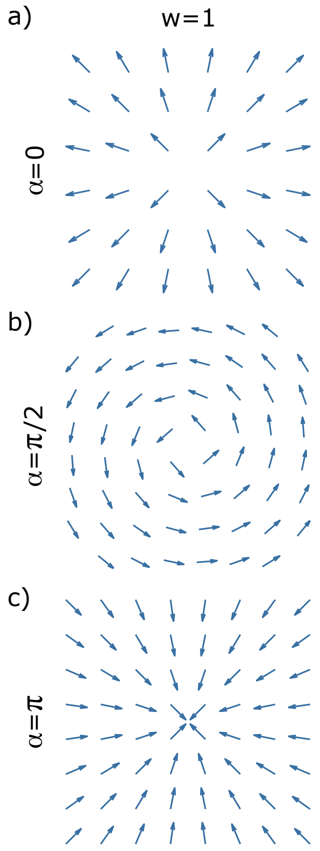

Figure 2.12: Topological defects in a xy-model with $w = 1$ and an overall phase shift α varying from 0 to π. Therefore, a "hedgehog" defect (**a**) is topologically equivalent to a vortex (**b**).

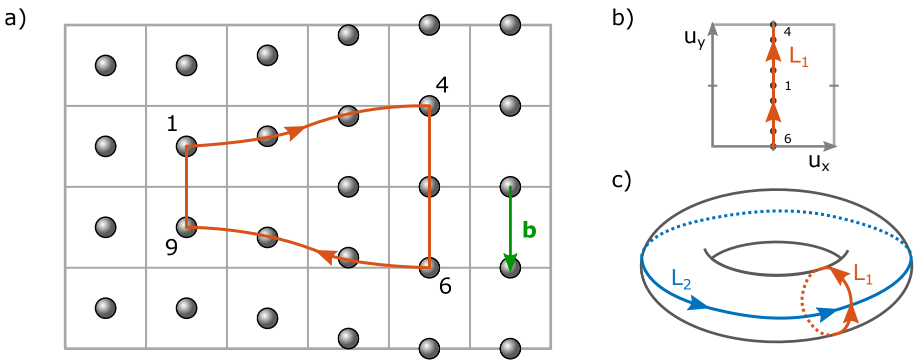

Figure 2.13: **a**, Sketch of a topological defect in a cubic 2D lattice with a contour (red) circulating around a dislocation, which is also characterized by the Burgers vector $\boldsymbol{b}$ (green). **b**, Displacements of the atoms on the contour mapped into order-parameter space. **c**, Torus representation of the order-parameter space with loops L_1 and L_2 for horizontal or vertical dislocations, respectively. Figure adapted from Ref. [94].

by traversing around the region of interest on a closed contour while mapping the order parameter $\boldsymbol{u}(x, y)$ on the associated torus. As can be seen in Fig. 2.13, this extra row of atoms, partially inserted from the right side, and usually referred to as a dislocation, resembles a circulation L_1 around the torus, whereas a dislocation inserted from the top or bottom would correspond to path L_2. Hence, in this case, the number of extra rows or columns of atoms constitute the winding numbers w_1 and w_2, and, due to the shape of the torus, it is clear that for both types of dislocations the contours L_1 and L_2 cannot be transformed into each other.

Since the winding numbers w_i in periodic solids are directly related to the number of extra rows or planes of atoms, topological defects in crystalline structures may be described in terms of the lattice basis vectors $\boldsymbol{a}_i$. Then the vector $\boldsymbol{b} = w_i \boldsymbol{a}_i$, also referred to as *a Burgers vector*, represents the strength and type of a dislocation defect of winding number w_i. For a geometrical construction of $\boldsymbol{b}$, one circuits around a defect counterclockwise in steps of $\boldsymbol{a}_i$. By repeating the same step sequence in an undistorted region of the lattice, the path won't yield a closed loop, and $\boldsymbol{b}$ is defined as the necessary closing vector[4]. Proceeding from 2D lattices to three dimensional crystals, the singularity of a dislocation defect is not just a single point, but becomes a line winding through the crystal structure. In this case defects are distinguished between so-called edge and screw dislocations, depending on whether $\boldsymbol{b}$ is perpendicular or parallel to the dislocation line, respectively [51, 97, 99].

---

[4] However, in the literature there seems to be uncertainty with respect to the sign of $\boldsymbol{b}$ comparing references [52, 97] and [99]. For consistency, this work will use the definition presented in [97].

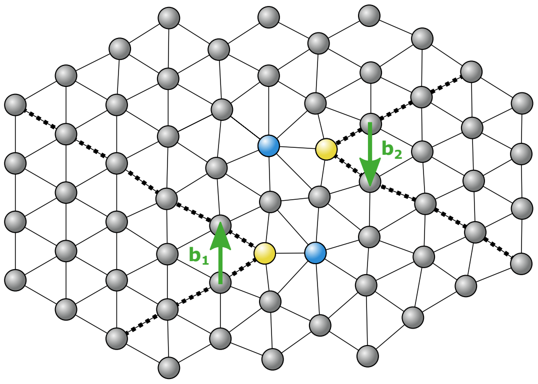

Figure 2.14: Hexagonal crystal lattice exhibiting two dislocation defects. Each defect is either characterized by two extra rows of atoms (dashed bonds) or, alternatively, one five-fold and one seven-fold coordinated atom (yellow and blue, respectively) at the dislocation core. These defects can appear if the crystal is sheared in the opposite directions given by the two Burgers vectors $\boldsymbol{b}_1$ and $\boldsymbol{b}_2$.

The concept of Burgers vectors is quite universal and has been successfully employed to characterize dislocation defects in crystalline media even before the concept of topological order was widely applied to condensed matter physics. Thus, in many situations they constitute an equivalent description to homotopy groups to grasp the nature of topological defects at hand [92].

For example, the above introduced concept of Burgers vectors also holds in a 2D hexagonal crystal lattice, although dislocation defects in this type of periodic arrangements are defined somewhat differently. Here, each defect is characterized by two extra semi-infinite lines of atoms (or other lattice defining entities), as compared to one half line, which is the case for cubic lattices (cf. Fig. 2.13 and Fig. 2.14).
Alternatively, dislocation defects in hexagonal arrangements may be identified by means of the coordination number. Specifically, in this case, each dislocation core features exactly one five-fold and one seven-fold coordinated atom, which are depicted in Fig. 2.14 in yellow and blue, respectively.

In general, the nature of topological defects strongly depends on the spatial dimension d of the considered system and the number n of components necessary to describe the chosen order parameter. Using this notation, the dimension of the present topological defects is determined by $d - n$ [100]. For instance, in an Ising Ferromagnet the spin can only adjust along one direction ($n = 1$), and topological defects manifest as domain walls, which appear as lines in $d = 2$ and surfaces in $d = 3$ [101]. In comparison, for $n = d = 2$, the topologically protected states are point like and appear as vortices or dislocations, as discussed above.

2.4.2 KTHNY-theory and hexatic phase

Furthermore, the concept of dislocations is beneficial to understand melting on an atomic level. Although phase transitions are occurring ubiquitously, their description is mostly of phenomenological nature. The underlying processes, however, are far from being well understood, and microscopic theories of melting solely exist for two-dimensional systems [102]. The most prominent approach was developed in the 1970s by John Kosterlitz, David Thouless, Burt Halperin, David Nelson, and Peter Young, therefore named KTHNY-theory. It describes the transition from a well-ordered 2D crystal to an isotropic fluid via the unbinding of topological defects and the subsequent loss of translational and orientational order.

Specifically, in the KTHNY-theory, the melting process takes place via two continuous phase transitions occurring at the two distinct temperatures T_m and T_i. Below T_m, the 2D crystal is characterized by quasi long-range translational order and a likewise long-range orientational symmetry. To quantify translational and rotational order of a hexagonal lattice, it is instructive to introduce the two respective correlation functions $g_T(\boldsymbol{R})$ and $g_6(\boldsymbol{r})$ as [102, 103]

$$g_T(\boldsymbol{R}) = \langle \rho_{\boldsymbol{G}}(\boldsymbol{R})\, \rho^*_{\boldsymbol{G}}(0) \rangle \quad \text{with} \;\; \rho_{\boldsymbol{G}}(\boldsymbol{R}) = \exp\left(i\boldsymbol{G} \cdot [\boldsymbol{R} + \boldsymbol{u}(\boldsymbol{R})]\right), \text{ and} \tag{2.48}$$

$$g_6(\boldsymbol{r}) = \langle \psi(\boldsymbol{r})\, \psi^*(0) \rangle \quad \text{with} \;\; \psi(\boldsymbol{r}) = \frac{1}{N}\sum_{j=1}^{N} \exp\left(i6\theta_j(\boldsymbol{r})\right). \tag{2.49}$$

Here $\boldsymbol{G}$, denotes a reciprocal-lattice vector and $\boldsymbol{u}(\boldsymbol{R})$ is the displacement of the atom located at $\boldsymbol{R}$. To calculate the orientational correlation function $g_6(\boldsymbol{r})$ the bond angles θ_j of the N nearest neighbors need to be measured against a fixed axis.

Compared to three dimensions, where $g_T(\boldsymbol{R})$ is constant for $\boldsymbol{R} \to \infty$, in the situation of 2D crystals, the transversal correlation function decays algebraically even at low temperatures, which is also know as the the *Mermin-Wagner theorem* [104]. Specifically, this means $g_T(\boldsymbol{R}) \propto R^{-\eta}$ with η being defined via the Lamé constants λ_R and μ_R of the material (cf. Ref. [103]). In comparison, below T_m, the orientational correlation function $g_6(\boldsymbol{r})$ is a constant given by [102]

$$\ln g_6 = -\frac{9k_BT}{8\pi\mu_R a_0^2}. \tag{2.50}$$

At temperature T_m, the situation changes significantly. Now, thermally activated and formerly short-lived pairs of dislocations begin to unbind, which has large influence on the translational and rotational order. Due to the presence of free dislocation defects, the long-range translational correlation is markedly suppressed and decreases as $g_T \propto \exp(-R/\xi)$ with correlation length ξ [102]. The orientational correlation, on the other hand, is less strongly affected by free dislocations, and g_6 decays algebraically as $g_6 \propto r^{-\eta_6}$ with

$$\eta_6 = \frac{18k_BT}{\pi K_A} \tag{2.51}$$

where K_A denotes the Frank's constant of the material. This intermediate phase, characterized by short-range translational and long-range orientational order, is also referred to as the *hexatic phase*[5], which is exclusively present in 2D crystals and was first observed experimentally by Pindak *et al.*, who conducted x-ray diffraction experiments at thin films of smectic liquid crystals [102, 106].

The increased loss of translational order above T_m is illustrated by the scale bars and arrows shown in Figs. 2.15a and b. As stated in the previous section, alternatively to the two extra half-lines of atoms (dashed bonds), dislocations in a hexagonal lattice can be characterized by a pair of five- and seven-fold coordinated atoms, which are likewise depicted in yellow and blue in Figs. 2.15a and b.

Increasing the temperature even further, at T_i, the dislocations tend to dissociate, which means unbinding of the five- and seven-fold coordinated sites at a dislocation core. The resulting new topological defects are called *disclinations.* In comparison to dislocations, which feature two extra semi-infinite lines of atoms, disclinations correspond to a missing (or additional) wedge of atoms and exhibit a five-fold (or seven-fold) coordinated atom at its center (Fig. 2.15c). Hence, disclinations strongly suppress the orientational order, which now likewise decays exponentially. As a consequence, the 2D system passes on to an isotropic fluid phase lacking discrete transversal or rotational symmetry.

A prototype system to observe these two continuous phase transitions at $T_{m,i}$ and to validate the predictions of the KTHNY-theory are 2D colloid crystals [107, 108]. The

---

[5] In the situations of two- or four-fold rotational crystal symmetry, phases exhibiting short-range translational and long-range orientational order are called nematic or tetratic, respectively [105]. For Instance, this applies for periodic arrangements formed by liquid crystals.

two main advantages of colloids are that they are small enough to obey the principles of thermally driven Brownian motion and, on the other hand, are large enough to be directly analyzed in real space by means of video microscopy [107, 109]. This technique allows for identification and characterization of single dislocations in the colloid lattice, as well as for tracing trajectories of single colloids.

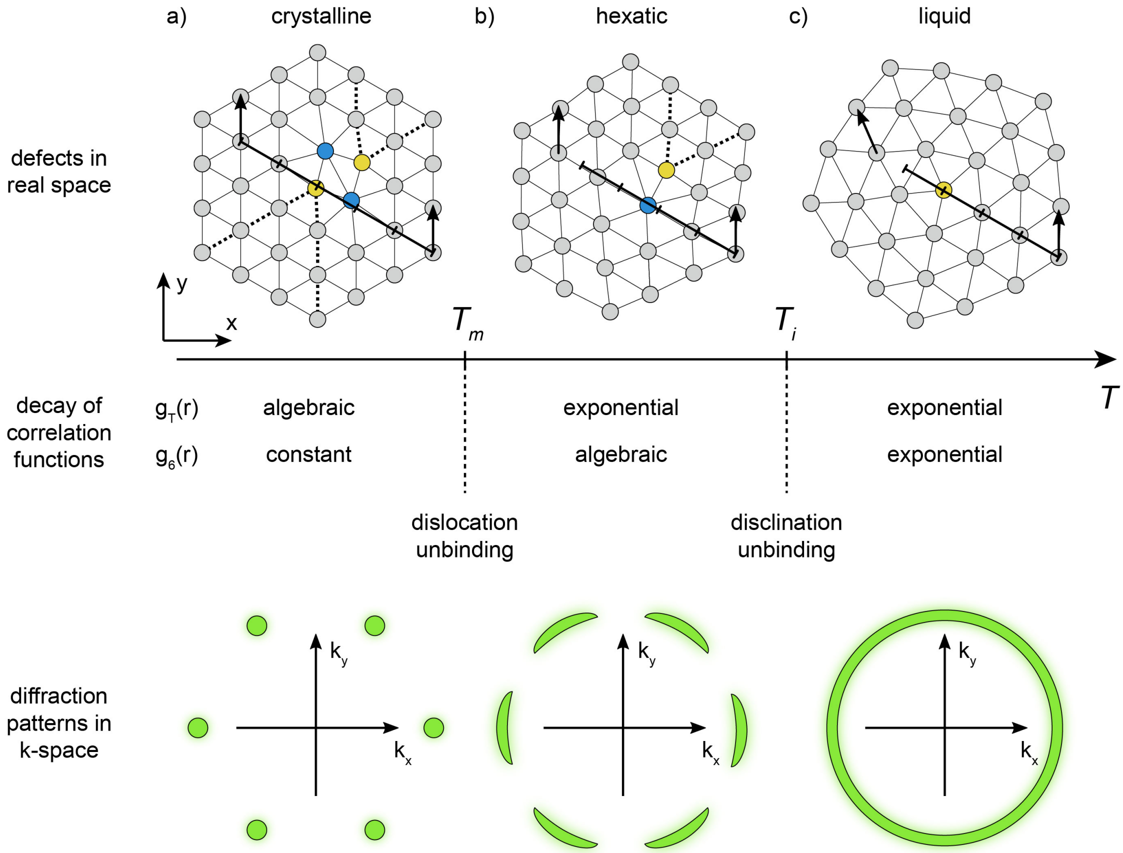

Figure 2.15: Phase transitions predicted by KTHNY-theory. **a**, Undistorted 2D hexagonal crystal lattice leads to well defined diffraction peaks (bottom). Local thermal fluctuations do not affect the long range crystalline order. **b**, At temperature T_m thermally activated dislocation pairs begin to unbind and form free dislocations, which are characterized by one five- and seven-fold coordinated atom each (depicted in yellow and blue, respectively). In an alternative view, dislocations in a hexagonal lattice feature two additional half-lines of atoms (dashed bonds). In the hexatic phase at $T_i > T > T_m$ long-range translational order is lost exponentially, whereas orientational order persists (cf. scale bars and arrows). Due to the effective mosaicity of the lattice, typically, the diffraction peaks are elongated in azimuthal direction. **c**, Above T_i single dislocations dissociate into two disclinations characterized by one five- or seven-fold coordinated atom at its center. These defects break the discrete rotational symmetry (arrows) and indicate the transition to the isotropic fluid phase, which manifests itself as a uniform ring in k-space. Figure adapted from Ref. [108].

2.4.3 Topological defects in charge-density waves

Beyond the examples of ordered spin systems and atomic or colloidal crystal structures, topological excitations may be also found in arrangements of periodic charge modulations, i.e., CDWs. Here, one generally has to take into account the interaction of the CDW with the underlying atomic lattice. In particular, the degree of commensurability between both plays an important role for the occurrence and manifestation of topological defects.

As discussed in Sec. 2.3.1, a one-dimensional metal with a half-filled band is intrinsically unstable against a PLD. It gets distorted by a wavevector $q = 2k_F$ doubling the size of the unit cell, and simultaneously giving rise to a commensurate CDW, which has a two-fold degenerate ground state corresponding to the phase shifts $\varphi = 0$ and $\varphi = \pi$ (see Fig. 2.16). If the CDW exhibits a m-fold degenerate ground state, the phase jump at the domain boundary can be any integer multiple of $2\pi/m$. Then, in principle, all m ground states are equally possible and will be present in a 1D chain of atoms. Hence, at the domain boundaries between two regions of different ground states the CDW experiences a phase shift, which can be achieved either by strain or compression of λ_{CDW}. These domain boundaries are topologically stable and can travel along the atomic chain without changing their appearance. To describe their motion, one can employ the *sine-Gordon equation*, which has solutions of propagating solitary waves [81]. Thus, the kinks of a CDW at a domain boundary are also called solitons [81, 110].

If λ_{CDW} is incommensurate but close to a multiple of the underlying atomic lattice parameter a, it is possible that the CDW is slightly strained (or compressed) to fulfill the commensurability condition. As a consequence, it registers to the atomic lattice in

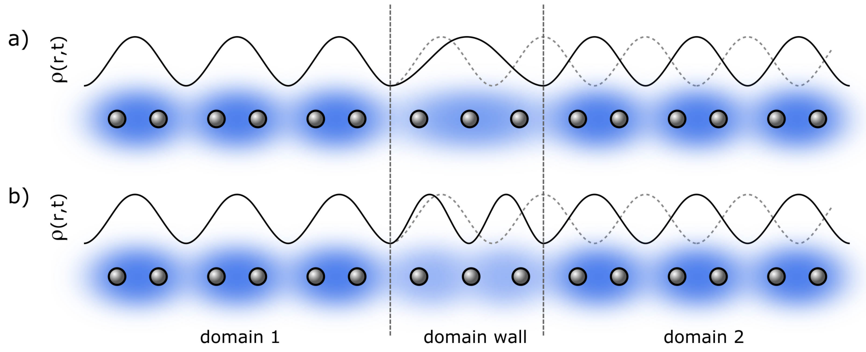

Figure 2.16: Sketch of possible antiphase domain boundaries in a commensurate one-dimensional CDW. The phase shift between the domains representing the degenerate ground states are facilitated either by strain (**a**) or compression (**b**) of the CDW.

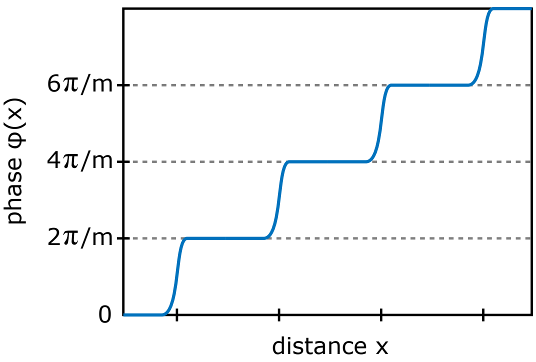

Figure 2.17: The phase $\varphi(x)$ of a close-to-commensurate CDW forming a soliton lattice is characterized by rapid phase jumps at the domain boundaries (or discommensurations) and remains constant in the commensurate regions. Figure adapted from Ref. [81].

finite regions separated by domain walls, which are also named *discommensurations* in this context [79, 81]. To this end, the commensurability energy

$$E_c \propto 1 - \cos\left(m\phi\left(r\right)\right) \tag{2.52}$$

has to compensate for the strain energy in each domain, as well as for the deformations in the domain boundaries. In thermal equilibrium, this leads to a regular spacing of commensurate patches separated by the domain walls of lowest energy. In an m-fold degenerate ground state, this corresponds to a phase jump of one atomic lattice parameter a between two adjacent domains (Fig. 2.17). Due to its periodicity, the resulting arrangement of commensurate regions and discommensurations is also referred to as a *soliton lattice* [81]. In fact, this situation is experimentally observable and, e.g., corresponds to the room temperature CDW phase of 1T-TaS$_2$, as will be shown in Sec. 3.1.

In the case of incommensurate CDWs, usually, the interaction with the underlying lattice for the appearance of topological defects can be neglected. Because of the absent commensurability energy, it is considered as a “free-floating” CDW that may be shifted across the atomic lattice without changing the total internal energy. Hence, rapid phase jumps, as displayed in Fig. 2.16, are not topologically stable anymore, but will decay into a phase shift of the CDW, slowly varying over a distance of several lattice constants.

However, this is not the case for topological defects in two-dimensional incommensurate CDWs, which often form a hexagonal lattice of charge accumulations. Therefore, it is instructive to discuss the occurrence of dislocations in periodic arrangements with three-fold symmetry.

As mentioned in Chap. 2.3, a convenient way to describe a hexagonal lattice of charge accumulations is that of a triple CDW, namely the superposition of three plane waves $\psi_j(\boldsymbol{r}) = \phi_j \exp\left(i\boldsymbol{q}_j\boldsymbol{r}\right)$ with wavevectors $\boldsymbol{q}_j$ rotated by 120° relative to each other and complex amplitudes ϕ_j. A topological defect at point P in one of the three contributions ψ_j then corresponds to a pitchfork dislocation of the ideally plane wave. It is comparable to the extra semi-infinite line of atoms in the crystal shown in Fig. 2.13, and traversing around it on a closed contour leads to an accumulated phase of $\pm 2\pi$ (cf. Fig 2.18),

As already stated in Sec. 2.3, in order to obtain a lattice of spherical charge accumulations by means of a triple CDW, the phases of ψ_j cannot be chosen arbitrarily, but have to satisfy the condition

$$\sum_{j=1,2,3} \arg\left(\phi_j\right) = 2\pi n \text{ with } n \in \mathbb{Z}. \tag{2.53}$$

Hence, the phase-shift induced by a dislocation in ψ_1 has to be compensated by another dislocation in ψ_2 or ψ_3. For this reason, topological defects in a hexagonal lattice are always composed of two partial dislocations and are characterized by Burgers vectors pointing in one of the six possible directions given by the lattice basis vectors $\pm\boldsymbol{a}_j$. This fact applies for continuously modulated hexagonal lattices, like CDWs, as well as for periodic arrangements of rigid entities like atoms or colloids [97].

However, in a continuously modulated system one has to avoid discontinuities of the order parameter at the dislocation center P. This is guaranteed by smoothly setting the charge modulation amplitude $|\phi_j|$ to zero while approaching the *core* of the dislocation. Following this requirement and Eq. 2.53, using polar coordinates r and θ, in one of his seminal works William L. McMillan defines a dislocation with Burgers vector in direction $-\boldsymbol{a}_1$ the following way [79]:

$$\phi_1 = c(r)\exp\left(-i\left(\theta - \frac{\pi}{2}\right)\right) \tag{2.54}$$

$$\phi_2 = c(r)\exp\left(i\left(\theta - \frac{\pi}{2}\right)\right) \tag{2.55}$$

$$\phi_3 = c(r) \tag{2.56}$$

$$c(r) = \phi_0\left(1 - \exp\left(-\frac{r}{R_c}\right)\right), \tag{2.57}$$

where ϕ_0 is the absolute value of the charge modulation far away from the defect, and R_c

denotes the radius of the dislocation core. Finally, the overall charge-density modulation including the defects is obtained via $\mathrm{Re}\left[\psi_1 + \psi_2 + \psi_3\right]$, which is shown in Fig. 2.18b for two exemplary topological defects with Burgers vectors $\boldsymbol{b}_{1,2} = \mp \boldsymbol{a}_1$.

In an atomic or colloidal lattice, dislocations increase the overall internal energy by locally inducing elastic deformations. Considering the interaction Hamiltonians of dislocations and disclinations, one finds out that for both types of topological defects their interplay can be described by an attractive pair-potential, which obeys $V(r) \propto \ln(r/a)$ [102]. Since this result is independent of the interaction of the atoms or colloids itself, the same holds for incommensurate CDWs. Accordingly, two dislocations of opposite winding number w at positions $\boldsymbol{r}_1$ and $\boldsymbol{r}_2$ exert a force on each other given by [97]

$$F(\boldsymbol{r}_1, \boldsymbol{r}_2) \propto K w^2 \frac{\boldsymbol{r}_2 - \boldsymbol{r}_1}{\left|\boldsymbol{r}_2 - \boldsymbol{r}_1\right|^2}\,, \tag{2.58}$$

where K is an isotropic elasticity constant of the CDW [79]. This behavior is similar to the situation of two charged point-like particles in 2D, with the difference that here the winding number or strength of the topological defect corresponds to a quantized topological charge. Accordingly, for some applications, topological defects may be interpreted as a two-dimensional Coulomb gas with mobile charges, which have the possibility to recombine [97].

Considering the mobility of topological defects, one has to distinguish between lattices composed of rigid entities and continuous modulations. In the former case, mass is conserved and motion (or creep) of dislocations demands the mobility of atoms or vacancies. Accordingly, in an atomic crystal dislocations preferably move in nearest neighbor directions given by the lattice basis vectors. These motions are referred to *glide* and *climb*, depending on whether they are parallel or perpendicular to its slip plane, respectively [99].

In a CDW, on the other hand, the charge density is conserved even if the modulation amplitude vanishes. This, in principle, allows topological defects to freely move through a CDW lattice. Due to attractive or repulsive forces, dislocations of opposite winding number will move towards each other, annihilate, and thereby lower the internal free energy. For a single CDW, this situation is shown in Fig. 2.18c, and it is obvious that annihilation of both defects will result in a plane wave.

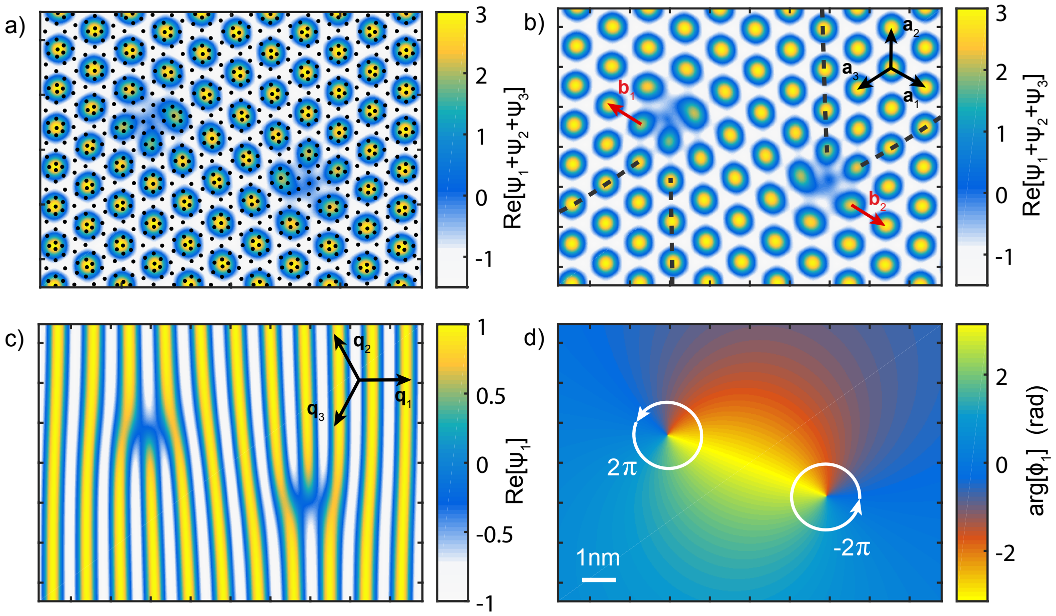

Figure 2.18: Topological defects in a hexagonal CDW lattice. **a**, Atomic lattice (black dots) distorted by an incommensurate CDW that features two dislocation defects. **b**, The topological defects of the CDW shown in **a** are characterized by Burgers vectors (red) of opposite sign. Alternatively, each dislocation can be described by two extra rows of charge accumulations (dashed lines). At the center of each dislocation core the CDW amplitude exponentially approaches zero to avoid singularities of the charge modulation. **c**, Real part of the contribution ψ_1 to the triple CDW illustrating that each topological defect in panel **a** and **b** is composed of two pitchfork dislocations. **d**, Argument of ϕ_1 showing two phase singularities in ψ_1. The integrated phases of $\pm 2\pi$ correspond to winding numbers of ± 1 or burgers vectors of opposite direction, respectively.

However, since topological defects in triple CDWs - or hexagonal lattices in general - are composed of two partial dislocations distributed on two of the three ψ_j, for complete annihilation of the defects, all partial dislocations have to come upon their exact counterpart. Alternatively, recombination of topological defects is also possible. Specifically, this means annihilation of one partial dislocation per defect each, and generating a new topological defect from the two remaining partial dislocations. Such processes require two partial dislocations of opposite winding number in ψ_j and two other dislocations in ψ_{j+1} and ψ_{j+2} having arbitrary winding numbers.

Alternatively, while characterizing topological defects by Burgers vectors, coalescence and recombination of defects is equivalent to simple vector addition. Therefore, it is easy to see that the two topological defects in Fig. 2.18b will annihilate, whereas two different defects, for instance, characterized by Burgers vectors $\boldsymbol{b}_1 = \boldsymbol{a}_1$ and $\boldsymbol{b}_2 = \boldsymbol{a}_3$ may recombine to a new defect having $\boldsymbol{b}_3 = -\boldsymbol{a}_2$. Another peculiarity of triple CDWs, compared to rigid hexagonal lattices, arises from the fact that the modulation amplitude may vanish, as in the dislocation core. For this reason, two partial dislocations generating a topological defect do not necessarily have to be at the same position, but can be displaced by several lattice constants [97]. The line connecting the two dislocations centers P_1 and P_2 is then characterized by imperfect phasing of the triple CDW.

Chapter 3

The layered CDW composite 1T-TaS$_2$

Belonging to the family of transition-metal dichalcogenides (TMDC), the quasi 2D material 1T-TaS$_2$ has been subject of research for decades and is still of vital interest due to its peculiar physical properties. This includes high pressure superconductivity [111, 112], a Mott-insulating state [112, 113], as well as the emergence of various temperature-dependent CDW phases [9, 76].

In all TMDCs, the unit cell consists of one transition-metal atom (e.g., Ta, Mo or W) and two chalcogen atoms (e.g., S, Se or Te), as is shown in Fig. 3.1. The latter are covalently bound and coordinated either trigonal prismatic or octahedrally around the transition metal atom. Repetition of these unit cells leads to solid layers, which are stacked along the crystal's c-axis and loosely bound via Van-der-Waals interaction. For 1T-TaS$_2$ the prefix 1T indicates that the sulfur atoms are arranged as an distorted octahedron around the tantalum atom, and its unit cell spans just one layer in c-direction [8]. Other

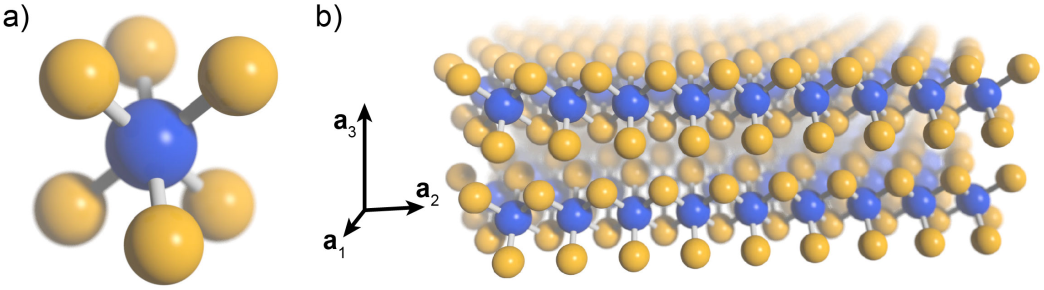

Figure 3.1: **a**, Unit cell of the 1T-TaS$_2$ crystal with one Ta atom (blue) and two octahedrally coordinated sulfur atoms (yellow). **b**, Lattice structure of two 1T-TaS$_2$ layers.

polymorphs of TMDCs can have larger unit cells in $\boldsymbol{a}_3$ direction, and, for instance, 4H$_b$-TaSe$_2$ features four layers of alternating chalcogen atom coordination (trigonal prismatic and antiprismatic) [114]. The pristine 1T-TaS$_2$ structure belongs to the space group $P\bar{3}m1$ (such as Cd(OH)$_2$) and exhibits lattice constants of $a_1 = a_2 = 3.36$ Å and $a_3 = 5.90$ Å [115].

Regarding the stability of this material, the yellow shimmering 1T-TaS$_2$ is a high-temperature polymorph present above 1100 K and meta-stable at room temperature.

In comparison, the gray metallic 2H-TaS$_2$ is the stable structure at ambient conditions [76, 116]. To produce the 1T polymorph at room temperature, the crystallites grown around 1130 K have to undergo a rapid quench and must not be reheated beyond 600 K [76, 117].

3.1 CDW phases and superstructures

In the temperature range below 600 K, 1T-TaS$_2$ features a variety of CDW phases, each giving rise to a corresponding periodic lattice distortion, which is linearly coupled to the CDW amplitude [79].

Due to the material's quasi 2D order, these superstructures are present in the bulk, as well as at the surface, and can be efficiently analyzed by means of electron diffraction or LEED in particular. Hence, in the following paragraph the possible lattice structures are discussed together with their representations in reciprocal space.

Commensurate phase

The ground state of 1T-TaS$_2$ is characterized by a CDW that is commensurate to the underlying atomic lattice, thus, denoted as the C-phase. Here, the PLD mainly affects the tantalum atoms, which form clusters consisting of 13 atoms, each shaped like a "Star of David" (cf. Fig. 3.2) with a maximum displacement amplitude of 0.24 Å [8].

Consequently, the superstructure unit cell features basis vectors $\boldsymbol{b}_1$ and $\boldsymbol{b}_2$ elongated by a factor of $\sqrt{13}$, and it is rotated by an angle of $\alpha = 13.9°$. In Wood's notation, this reads $\left(\sqrt{13} \times \sqrt{13}\right)$ R13.9°, which is a common way to describe simple superstructures [118, 119].

However, Wood's notation lacks the information, whether the rotation happens clockwise or counter-clockwise. Thus, since both symmetry-equivalent cases are equally possible in

$1T\text{-}TaS_2$, it is more instructive to use the transfer matrix notation [70], with

$$\begin{pmatrix} \boldsymbol{b}_1 \\ \boldsymbol{b}_2 \end{pmatrix} = M \begin{pmatrix} \boldsymbol{a}_1 \\ \boldsymbol{a}_2 \end{pmatrix} \text{ and}$$

$$M_{cw} = \begin{pmatrix} 3 & -1 \\ 1 & 4 \end{pmatrix} \text{ or } M_{ccw} = \begin{pmatrix} 4 & 1 \\ -1 & 3 \end{pmatrix}$$

where M_{cw} and M_{ccw} represent the superstructure of commensurate domains, which are rotated clockwise and counterclockwise, respectively. The occurrence of symmetry-equivalent ground states in the C phase was initially observed by Wilson *et al.* [76, 120]. These are denoted as α- and β-domains, which will be discussed in more detail in Chap. 7.2.

Due to the commensurate superstructure, the diffraction pattern of the C phase features CDW satellite spots around the atomic lattice Bragg peaks, which appear at wavevectors $\pm\boldsymbol{q}_C = (3\boldsymbol{a}_1^* + \boldsymbol{a}_2^*)/13$ and equivalent directions rotated by 120° [115]. Analogous to the real-space lattice, they are are tilted by 13.9° with respect to the atomic lattice Bragg peaks and fulfill the same commensurability condition. Accordingly, higher order satellite spots perfectly coincide (cf. Fig. 3.3 bottom).

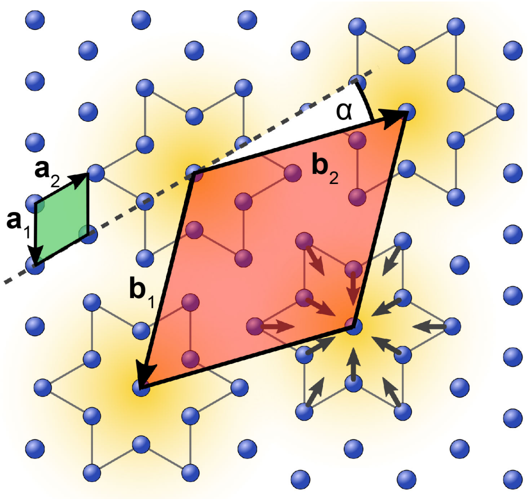

Figure 3.2: Sketch of one layer of Ta atoms forming a unit cell (green) of the pristine atomic lattice, as well as the commensurate superstructure, which consists of star-like clusters and features a 13 times bigger unit cell (red).

Nearly-commensurate phase

In the temperature range between 353 K and 187 K (or 223 K upon heating) 1T-TaS$_2$ exhibits the so-called nearly-commensurate (NC) CDW phase. Here, the overall CDW wavevectors are incommensurate to the atomic lattice, but their length and orientation are still close to the ones of the C phase, i.e., $\boldsymbol{q}_{NC} \approx 0.245\boldsymbol{a}_1^* + 0.068\boldsymbol{a}_2^* + 1/3\boldsymbol{a}_3^*$ [115]. Therefore, as discussed in section 2.4.3, the CDW may gain commensurability energy by local registration to the atomic lattice in finite regions separated by a rapid phase jump of the CDW. Hence, the NC phase is represented by a lattice of commensurate patches with discommensurations in between [121, 122]. While proceeding from one commensurate domain to the next, the CDW phase change can be either expressed as one atomic lattice constant or - depending on the direction - as 2, 6 or 8 times $\pi/13$ of the CDW wavelength [121]. To illustrate this fact, Fig. 3.4b shows the phase of ϕ_1, the complex amplitude of the first contribution to the order parameter of the triple CDW [121]. It depicts the 2D representation of the 1D CDW case shown in Fig. 2.17. Hence, it is possible to interpret the NC CDW phase as a two-dimensional soliton lattice, as predicted by Sólyom [81]. In an alternative view, the commensurate regions can also be seen as a Kagome lattice of edge touching hexagons. The discommensurations are then filling the remaining triangles (cf. Fig. 3.4a) [115].

Due to the repeated finite phase shift along the domain-like structure, the CDW satellite spots split up, as discussed in Sec. 2.2.2, which results in a highly decorated diffraction pattern (Fig. 3.3, middle). Thus, the distance between two neighboring CDW diffraction peak maxima directly gives information about the size of the commensurate patches. At ambient conditions their diameter is roughly five star-like clusters wide, corresponding to ~ 7.3 nm. However, by lowering the temperature, their size increases, which causes the split up CDW diffraction spots to merge (cf. diffraction patterns in Chap. A.4 of the appendix) [123]. This process can be also viewed as a continuous rotation of the satellite peaks, until the positions of lower- and higher-order CDW diffraction peaks coincide.

As depicted in Fig. 3.3, the C-NC-phase transition is subject to a considerable hysteresis. Additionally, it shows the appearance of a triclinic (T) CDW phase, in the range of 187 K to 223 K, which is only observable upon heating [120, 124, 125]. It can be interpreted as an anisotropic phase, in which two of the three CDW wavevectors stay in the C phase, but one is loosing its commensurability to the atomic lattice. The result is a striped CDW superstructure, which, for example, has been observed in STM measurements [125].

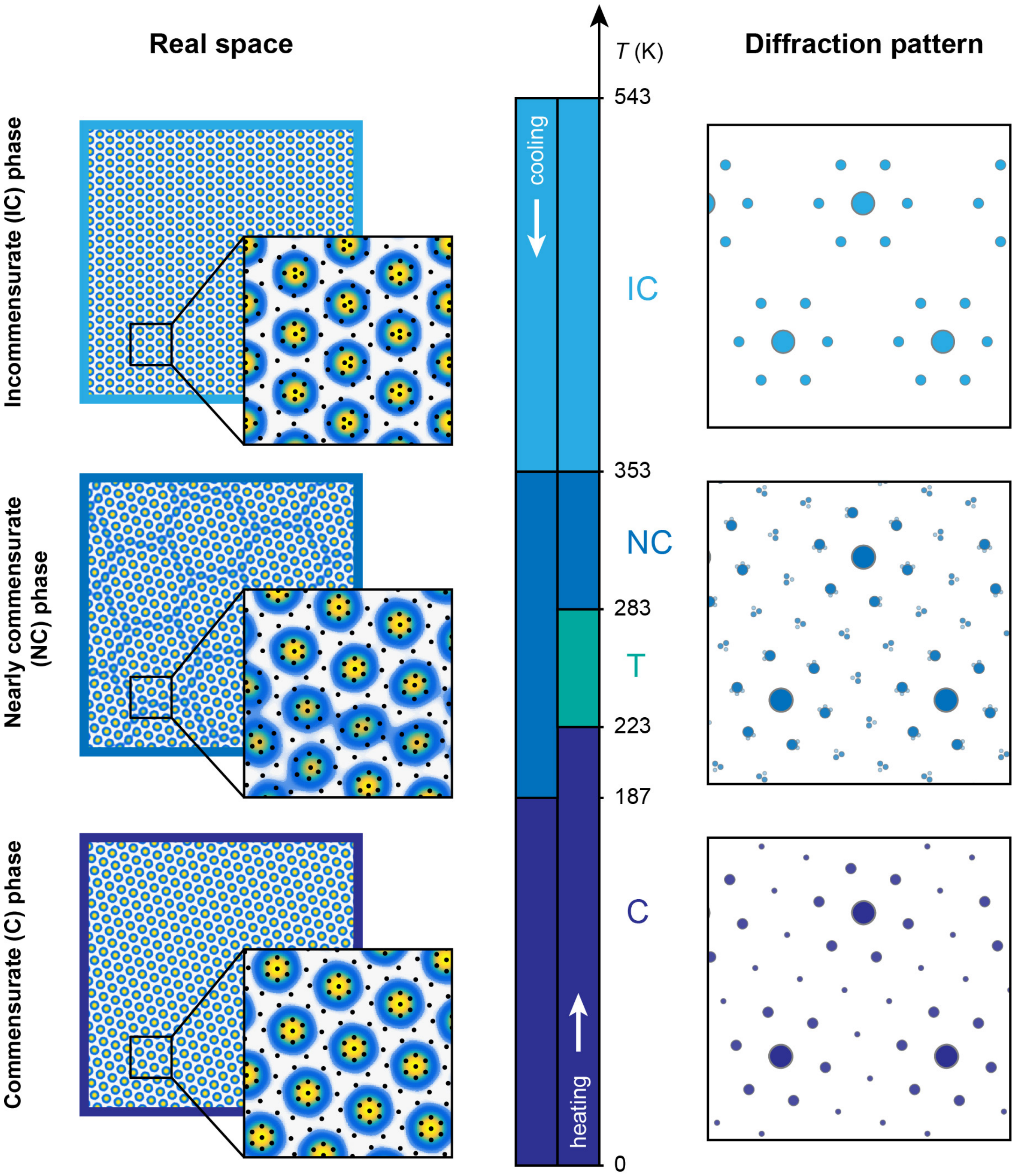

Figure 3.3: Schematic summary of the temperature-dependent CDWs present in 1T-TaS$_2$. Left column: Real space representation of the CDW order in the IC, NC and C phase (top, middle, bottom). Close-ups show the associated periodic lattice distortion of the underlying tantalum atoms. Right column: Sketch of the diffraction patterns corresponding to the respective CDW phases on the left side. Both real and reciprocal-space representations of the triple CDW indicate the rotation of the wavevectors $\boldsymbol{q}_i$ by 13,9° during the transition from the C to IC phase. The triclinic (T) phase is just present upon heating in a small temperature range.

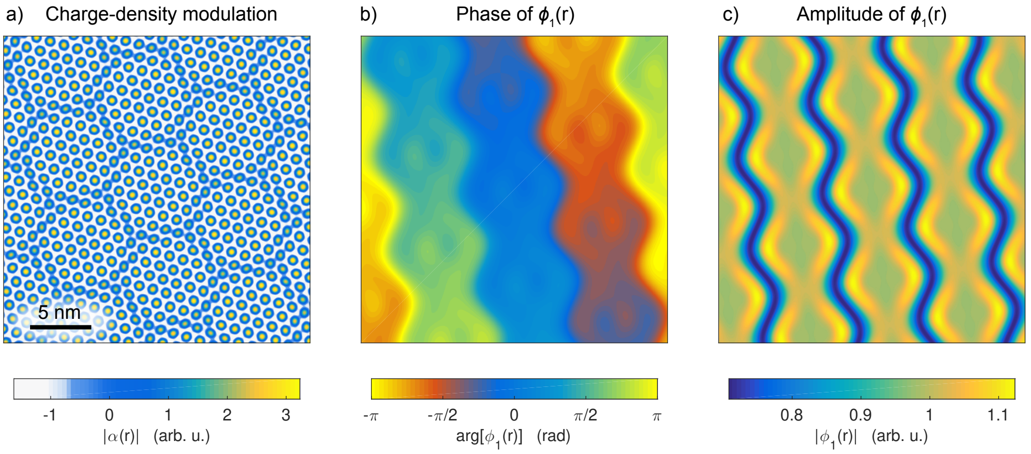

Figure 3.4: Charge-density modulation and complex amplitude of the NC phase. **a**, The NCP is characterized by a close-to-hexagonal arrangement of commensurate patches separated by discommensurations. Their nature is determined by the complex amplitudes ϕ_j of the three contributions φ_j to the triple CDW. **b**, For instance, considering ϕ_1, the phase $\varphi_1 = \arg[\phi_1]$ remains relatively constant in commensurate regions of the NCP and along $\boldsymbol{q}_1$, whereas it undergoes a rapid change at the discommensurations in directions $\boldsymbol{q}_2$ and $\boldsymbol{q}_3$. **c**, The pronounced phase jump at the discommensurations is accompanied by a reduction of the amplitude $|\phi_1|$ down to ~70% of its original value [121].

Incommensurate phase

Exceeding 353 K, the CDW in 1T-TaS$_2$ exhibits a further phase transition associated with a pronounced effect on the lattice distortion. Beyond this temperature, the wavevectors of the CDW and the atomic lattice basis vectors are lacking a rational multiple and are oriented parallel to each other. This means $\lambda_{CDW}/a_{1,2} \approx 3.53$ for the real space structure and $\boldsymbol{q}_{IC} \approx 0.283\boldsymbol{a}_1^* + 1/3\boldsymbol{a}_3^*$ in reciprocal space, respectively [115]. Accordingly, the present CDW phase is named incommensurate (IC) CDW phase. Since the orientation of the wavevectors is drastically differing from the C and NC phase, it inhibits the appearance of commensurate regions in real space, as for the NC phase. Since in this case the CDW is no longer in registration with the atoms, it can be shifted across the atomic lattice without energy gain or loss. Hence, the ICP may be also considered a “free-floating” CDW phase. Consistent with this weaker coupling, the IC phase shows a significantly smaller maximum displacement amplitude of the atoms compared to the C phase of approximately 0.166 Å [90]. Furthermore, the PLD is less nonlinear, manifesting itself in the lack of higher harmonics in the diffraction pattern (as sketched in Fig. 3.3, top). The IC phase is present up to 543 K and vanishes at higher temperatures where no CDW order is observable anymore, and 1T-TaS$_2$ is present in its metallic normal state.

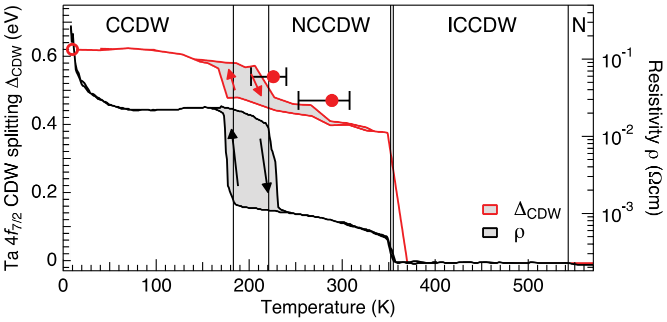

Figure 3.5: Temperature-dependent measurement of the in-plane resistivity at ambient pressure indicating the varying conductivity of the three CDW phases. Reprinted figure with permission from Ref. [127], Copyright 2010 by the American Physical Society.

All CDW transformations discussed here are first-order phase transitions [121, 124], in comparison to, e.g., 1T-TiSe$_2$, which exhibits a second-order phase transition directly from the commensurate CDW to the metallic state [126].

3.2 Electronic properties

Due to its close relationship to the structural degrees of freedom, the electronic properties of 1T-TaS$_2$ exhibit numerous characteristic signatures, such as hysteresis, which occur simultaneously to the CDW phase transitions. These may be observed via, e.g., measuring the in-plane resistivity, the optical reflectivity, or mapping the electronic band structure by means of ARPES.

Since the geometry of the commensurate superstructure at low temperatures is relatively simple to describe, usually tight-binding models are used to study the corresponding band structure [8, 128]. To this end, one considers the displacement of the tantalum 5d conduction electrons, which move towards the center of a star-like cluster. In k-space, this formation of the C phase goes along with translating all umklapp bands by reciprocal lattice vectors of the superstructure into the first Brillouin zone (Fig. 3.6c). Subsequently, these bands split up into subband manifolds, thus lowering the electronic energy and giving rise to a band gap opening between the K and M-points (Fig. 3.6d, red arrow). However, since just twelve out of thirteen electrons contribute to this deformation, and one electron remains unchanged at the center of the cluster, there is still a narrow half-filled band intersecting the Fermi level preventing the system from being completely gapped (Fig. 3.6d). Accordingly, the C phase would be conductive.

Resistivity measurements, however, indicate that 1T-TaS$_2$ is insulating at low temperatures and ambient pressure (cf. Fig. 3.5). This fact can be explained by strong

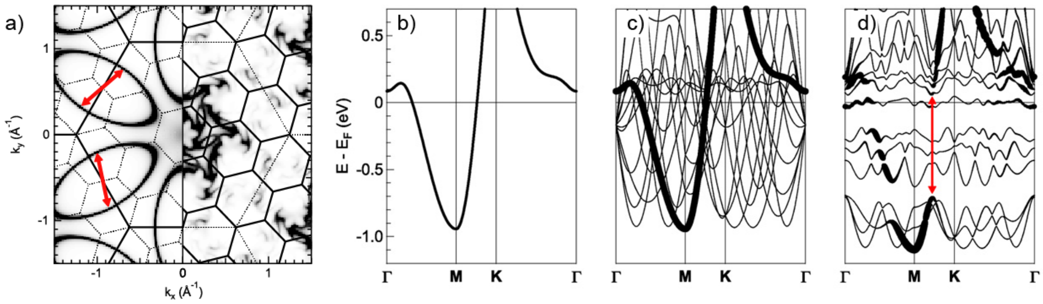

Figure 3.6: Fermi surface and band structure of 1T-TaS$_2$ obtained by means of tight-binding calculations. **a**, Fermi surface in the normal phase (left) and after formation of the commensurate superstructure (right). Brillouin zones of both the normal phase and the superstructure are sketched with solid and dotted lines. Red arrows indicate possible nesting vectors. **b**, Band structure of the pristine 1T-TaS$_2$. **c**, Translation of all umklapp bands by reciprocal lattice vectors of the superstructure into the first Brillouin zone of the unreconstructed material. **d**, Spectral weight of the reconstructed band structure after the displacement inside the star-like clusters is taken into account. © IOP Publishing. Reproduced with permission from Ref. [8]. All rights reserved.

electron-electron interactions in the star-like clusters, which lead to the formation of an empty upper and occupied lower Hubbard-band separated by a gap of a few 100 meV close to the Γ-point [113]. Although Mott-physics was suggested relatively early to account for the high resistivity of the C phase [129], validation of this prediction took until spectroscopic methods became available [130, 131].

Thus, taken as a whole, the band structure of the C phase features two band gaps. They are located around the center of the k-space and at the Brillouin zone boundary. Depending on their formation mechanism, these can be attributed to a strong electron-electron interaction and electron-phonon coupling, respectively (Fig. 3.7, left side). Since at elevated temperatures the strong electron correlation is lost together with the CDW commensurability, in the IC phase, only the band gap between the K and M-point remains due to Fermi surface nesting (Fig. 3.7, right). In the intermediate spatially textured NC phase both cases are present at the same time. The hexagonally arranged commensurate patches remain insulating, while the charge transport is mediated by the network of discommensurations [112].

To emphasize the distinguished interplay between CDW order and electronic properties in 1T-TaS$_2$, the stacking of the commensurate CDW in $\boldsymbol{a}_3$-direction seems to play an important role for the conductivity and possibly could be used to switch the C phase between a semiconducting and metallic state [132]. Similar observations were made in

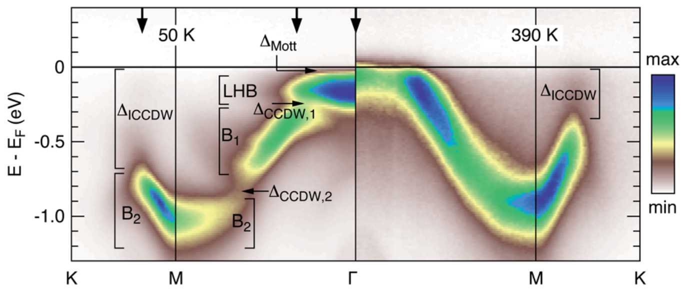

Figure 3.7: The characteristic gaps in the band structure of the C (left) and the IC phase (right) are visualized by ARPES measurements. Figure reprinted from Ref. [113] by Sohrt *et al.*, licensed under CC BY 3.0.

different studies, which report the observation of a conductive “hidden phase” accessible at low temperatures via intense optical excitation [133–136]. Another intriguing electronic phenomenon in 1T-TaS$_2$ includes the superconductivity present at temperatures below 5 K and pressures above 4 GPa [112].

3.3 Previous time-resolved experiments

A manifold of experimental and theoretical works focusing on TMDCs, and 1T-TaS$_2$ in particular, have been conducted in the 1970s and 80s [76]. These comprise various electron and x-ray diffraction studies [90, 120, 123], as well as optical scattering [137] and transport measurements [129]. Still, the nature of the CDW origin was not fully understood, and over time, the scientific interest turned to other fields, such as high T_c superconductors. However, the situation drastically changed with the discovery of graphene in 2004 and the Nobel prize being awarded for it six years later [138]. Due to its outstanding electronic and mechanical properties, a lot of attention was drawn towards carbon monolayers and other (quasi) 2D materials. This renewed interest, plus the availability of novel experimental techniques developed in the meantime led to a renaissance of layered TMDCs in the recent decade. In the following paragraph, a brief summary is given about previous time-resolved studies focusing on the ultrafast electronic and structural dynamics of 1T-TaS$_2$.

A versatile experiment to elucidate the response of the electronic system after intense excitation is time-resolved photoemission spectroscopy (PES). Its high temporal and energy resolution makes it a versatile tool to study the dynamics of the overall density of states. By extending this approach to time-resolved ARPES, the redistribution of spectral weight of specific bands becomes accessible with a high k-space resolution, as well. These experiments require high photon energies, which is why they are commonly conducted at synchrotrons or free-electron lasers, or, alternatively, pumped by HHG sources. With regard to 1T-TaS$_2$, major effort has been put on clocking the decay of the Mott-insulating behavior in the low-temperature C phase after optical excitation by means of both tr-PES [22, 117, 127, 139] and tr-ARPES experiments [23, 113, 140]. Here, the essential results are two spectroscopic signatures occurring on two distinct timescales. The first is an almost instantaneous collapse of the Mott-gap close to the Γ-point, which in all experiments happens within the achievable temporal resolution and, thus, is assumed to be faster than 50 fs [113, 140]. The second signature is a coherent oscillation of the CDW amplitude mode, which is strongly coupled to the electrons near the Fermi edge between the M- and K-point of the reconstructed Brillouin zone [140]. The excitation of these phonon modes takes approximately 230 fs, which corresponds to one half cycle of the oscillation period. It is worth noting that all tr-(AR)PES experiments mentioned here exclusively focus on C phase, and no time-resolved measurements of the NC or IC phase have been conducted yet. The few available NC or IC phase band structures recorded by ARPES correspond to static measurements [113, 140]. Moreover, although in most experiments the applied pump fluences are high enough to drive the C-NC-phase transition, the measured spectra only represent non-equilibrium transient states of the C phase driven by a hot electron bath [23, 113, 117, 140], which should drastically differ from the equilibrium NC phase with its well ordered domain-like structure.

In contrast, purely optical fs-spectroscopy requires significantly less experimental effort. In a classical pump-probe approach, mapping the transient reflectivity $\Delta R/R$ provides information about the single particle response of the electronic system and possible temperature-dependent gaps, as well as the excitation of coherent phonon oscillations. For 1T-TaS$_2$, almost all measurements were conducted in the low-temperature C phase. Here, early experiments focus on the Peierls-Mott gap and the phonon spectrum at the transition to the NC phase [141] or report on the time-dependent evolution of two distinct phonon modes ($\nu_{AM} = 2.4$ THz and $\nu_{E_g} = 2.1$ THz) at 3.3 K [142]. Possibilities to extend this approach are either THz time-domain spectroscopy [143], other broadband excitations to obtain information about the transient conductivity [144], or reflectivity measurements using double-pulse excitation [136, 145]. The latter experiments indicate that it is possible to suppress the CDW amplitude mode with a second pump pulse delayed by multiples of the amplitude mode period [145]. Alternatively, the second pump pulse can be used to trace the amplitude mode through the optically induced transition from the C phase to the formerly mentioned “hidden” H-state [136].

A complementary approach offering time-resolved access to the structural degrees of freedom in 1T-TaS$_2$ is ultrafast electron diffraction (UED) at high kinetic energies. Because of the experimental challenges associated with this technique, such as providing for ultrashort high-brightness electron pulses, only few experiments were conducted at 1T-TaS$_2$ in the recent years. In a first set of measurements, Eichberger *et al.* optically suppressed the CDW order and traced the response of the PLD in the NC phase around 200 K [146]. Here, the PLD was suppressed within 250 fs, consistent with previous ARPES measurements [140], and relaxed on a timescale of 4 ps. However, in this experiment, the fluences used (2-4 mJ/cm^2) were not sufficient to thermally drive the transition to the IC CDW phase. On the contrary, in Refs. [147] and [148] the CDWs underwent an optically excited transition from the C and the NC state to the IC phase, respectively. In the former tr-TEM study, the cascade of phase transitions was associated to a continuous rotation of the CDW wavevectors [147], whereas the latter UED experiment exclusively concentrated on the NC-IC transition, which appeared to happen in a two-step process on a fluence-dependent timescale (0.3-1.5 ps for the fast component and 80-230 ps for the slow component) [148]. As a possible microscopic mechanism for the emergence of the ordered high temperature CDW state, Haupt *et al.* proposed a domain-like expansion of the IC CDW starting at the NC phase discommensurations.

An alternative method also sensitive to the PLD is time-resolved x-ray diffraction (XRD) in a grazing incidence geometry. In principle, this technique allows for very high spatio-temporal resolution, whereas a major challenge is to maintain a homogeneous sample excitation due to the different laser and x-ray penetration depths. Experiments using this approach were conducted at the C phase of 1T-TaS$_2$ [149], as well as at the NC-IC phase transition [150]. Reference [149] reports on the observation of coherent amplitude modes, that are damped to a long-lived state of reduced diffraction intensity, which is subsequently associated with the “hidden” H phase observed by Stojchevska *et al.* [135]. In the second work, Laulhé *et al.* traced the emergence of the IC phase after the optically induced phase transition. Here, they observed a narrowing of the IC diffraction peaks occurring on a few hundred ps timescale. The corresponding increase of the correlation length is then attributed to a domain-like coarsening of the newly created IC CDW phase [150].

Chapter 4

Ultrafast low-energy electron diffraction

In the recent decades, extending optical pump-probe schemes to x-rays or high-energy electron pulses paved the road to analyze the atomic rearrangement accompanying phase transitions or order-disorder phenomena with very high spatio-temporal resolution and, for example, has been realized in ultrafast transmission electron microscopy (UTEM) [151–153]. Due to their distinguished penetration depth, high-energy electrons or x-ray pulses are mainly sensitive to the bulk lattice, whereas the structural dynamics occurring at the sample surface remain elusive.
To enhance the surface sensitivity of these probes, both electrons and x-rays can be employed in grazing incidence scattering geometries, which are referred to as time-resolved reflection high-energy electron diffraction (tr-RHEED) [25, 27] or surface x-ray diffraction (SXRD) [17, 154]. While the latter technique is still lacking an ultrafast implementation, mostly because of the weak diffracted signals [155], significant progress has been made in terms of tr-RHEED [28, 156].

Here, one of the main challenges regarding the temporal resolution is the temporal spread of electrons impinging on the surface, due to the small angle of incidence. This has been resolved by exciting the sample with pump pulses incorporating a tilted pulse front scheme allowing for the observation of phase transitions in indium nanowires on a silicon substrate with 330 fs temporal resolution [28].
However, to conclude the lattice symmetry solely from RHEED measurements is challenging. This is particularly the case for highly decorated diffraction patterns or if several superstructures are present simultaneously. Further difficulties for RHEED may arise from its high sensitivity to the surface morphology, which is a result of the grazing incidence and the relatively large probing area [27].

A different approach for time-resolved diffraction emanates from LEED, which already serves as a standard method for surface structure determination since the 1970s [17]. As laid out in detail in Chap. 2.1, LEED features a high surface sensitivity and enables the analysis of the surface symmetry and lattice constants from a single diffraction pattern independent of the azimuthal sample orientation. Furthermore, LEED comprises an extensive theoretical framework including dynamic scattering theories, as well as methods for surface crystallography, such as Tensor-LEED. Hence, LEED is extended to ultrahigh temporal resolution by using a stroboscopic optical-pump, electron-probe scheme.

Since the development of ultrafast LEED (ULEED) is strongly connected to this work, the following sections highlight several aspects of ULEED in general and the present experimental setup in particular. This includes preceding attempts of its realization, the fundamental challenges that need to be overcome in this context, as well as the specific concepts used for the implementation of this particular time-resolved LEED experiment. Finally, the capabilities of the present ULEED setup are presented along with a characterization of its spatial and temporal resolution.

4.1 Preceding work and challenges in ultrafast LEED

Typical pump-probe-experiments are designed to trace ultrafast electronic or structural changes on their intrinsic timescales, therefore making a high temporal resolution the key ingredient. Independent of the specific setup, the latter is given by a temporal convolution of the pump and the probe pulses.

However, for most optical-pump, electron-probe instruments, the duration of the electron pulses is significantly longer than the fs laser pulses used for sample excitation. Thus, the optical excitation can be assumed as almost instantaneous and the achievable temporal resolution is solely limited by the electron pulse duration τ_e at the sample. The latter strongly depends on the kinetic energy E of the electrons and their energy spread ΔE, as well as on the propagation distance d and other effects, such as space charge broadening or different trajectories. As will be shown below, among these effects, the kinetic energy E has the highest influence on the temporal width of the electron pulses, hence, causing low-energy electron pulses to be orders of magnitude more susceptible to dispersion and other detrimental effects than their high-energy counterparts. As a consequence, it is considerably challenging to provide for ultrashort electron pulses in the range of $E = 30$ - 500 eV at a sample surface and to realize an ultrafast LEED experiment with the sufficient temporal resolution and low beam emittance.

Early efforts date back till 1984, when Becker *et al.* employed an electronically triggered LEED gun synchronized to a Q-switched pump-laser [157]. In order to investigate the transient melting of a Ge(111) surface, they studied the intensity of the specularly reflected electron beam with an effective temporal resolution of ~10 ns. Roughly seventeen years later, being aware of the need for short probe pulse propagation distances, Karrer *et al.* presented a time-resolved LEED setup including a laser-driven electron source very close to the sample [158]. Although this electron gun was predicted to provide for pulse durations in the ps range, time-resolved measurements turned out excessively arduous due to a very low electron yield at the high diffraction angles accessible. Subsequently, a modified version of this source facilitated the observation of laser-induced space-charge dynamics close to a copper surface [159].

A different approach has been pursued in two recently published works [35, 36]. Herein, ultrathin graphene samples were investigated by transmission diffraction with low-energy electrons, utilizing nanometric photocathodes as highly coherent electron sources. Yet, although the setup of Müller *et al.* is more suitable for time-resolved point projection microscopy, a non-time-resolved LEED image was also acquired [35]. On the other hand, the implementation by Gulde *et al.*, incorporating a nanoscopic photoemitter in combination with an electrostatic lens assembly, enabled the time-resolved observation of polymer crystallites melting on a free-standing graphene substrate [36]. In fact, the study by Gulde *et al.* resembles the first analysis of structural dynamics by means of ultrafast LEED with ps temporal resolution.

However, even in the light of these notable achievements, the realization of ULEED in a backscattering geometry for the analysis of solid crystal surfaces is highly desirable, but equally challenging. As stated above, the essential task is to provide for electron pulse durations τ_e at the sample position as short as possible. Neglecting pulse broadening due to space charge, as well as the effect of the acceleration regime of the electron bunches, their pulse duration τ_e in field free propagation is approximated as [158]

$$\tau_e = \frac{\Delta d}{v} + \frac{\Delta E}{2E}\frac{d}{v} \tag{4.1}$$

where d, v and E are the electron propagation distance, the velocity and the mean kinetic

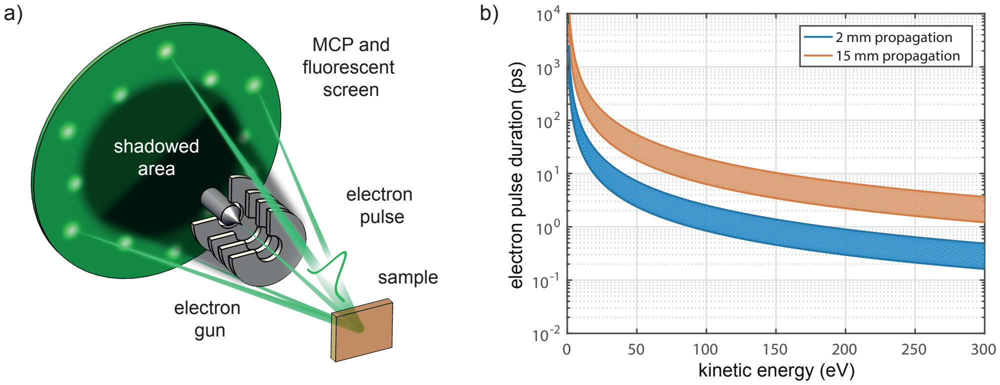

Figure 4.1: a, Sketch of a pulsed electron gun operated in a backscattering geometry. It illustrates the basic need for a small outer diameter to minimize the shadowed area on the detector screen. **b**, The electron pulse duration τ_e after $d = 2$ mm and 15 mm of field-free propagation as a function of electron energy E and for $\Delta x = 0$ is depicted in blue and orange, respectively. Lower and upper bounds of the filled regions correspond to kinetic energy spreads of $\Delta E = 0.5$ eV and 1.5 eV, respectively.

energy with the uncertainties Δd and ΔE, respectively. The pulse duration τ_e nonlinearly depends on E and inversely increases for the lower electron energies typically used in a LEED experiment. Figure 4.1b illustrates τ_e for two exemplary flight distances d and kinetic energy spreads ΔE, respectively, in the case of a perfectly collimated beam, i.e., $\Delta d = 0$. Hence, to conduct a ULEED experiment, electron energies of $E \geq 100$ eV are clearly favorable with respect to the temporal resolution. Since τ_e also increases linearly with drift distance d and energy spread ΔE, both quantities have to be minimized, as well. While ΔE is defined during the electron emission process and not trivial to control, the propagation distance d between the source and the sample merely depends on the experiment geometry. For a LEED setup operated in back reflection, at a critical distance d_c, the shadow of the gun masks the majority of the diffraction pattern recorded on the fluorescent screen (Fig. 4.1a). Hence, the shortest temporal resolution experimentally achievable is always limited by the visibility of the diffraction pattern. The only way to resolve this trade-off is to design a drastically miniaturized pulsed electron source, as will be laid out in detail in the following sections.

4.2 Pulsed electron beams from nanometric metal tips

Hitherto, the electron emission process and its influence on the pulse dispersion during the acceleration of the electrons have been omitted. For this reason, the validity of the simple approximation for the temporal pulse broadening (Eq. 4.1) will be discussed next with regard to different cathode geometries.

Commonly, ultrashort electron pulses employed in stroboscopic pump-probe schemes are generated via photoemission from metallic cathodes using fs laser pulses. To this end, usually, intense laser pulses with photon energy $h\nu$ are focused either on thin metal films having a work function Φ or on nanoscopic metal tips. Although the latter are more difficult to fabricate and delicate to handle, sharp needle photocathodes feature several advantages compared to planar metal films.

A major benefit of nanometric tips arises from the local electric field enhancement at their apex - the so-called *lightning rod effect* [160, 161]. Aside from a geometrical correction factor k, the field F_t in the direct vicinity of the tip apex biased with a potential U is approximated by that of a point charge [162, 163]

$$F_t\left(r\right) = \frac{U}{rk}\,, \tag{4.2}$$

where the dimensionless factor k just depends on the shape of the tip, e.g., radius of curvature, the opening angle, or the distance to the anode and typically ranges from 5 to 8 [162, 164]. This is in clear contrast to the plate capacitor-like geometry and thus homogeneous electric field above a planar photocathode. Accordingly, the acceleration of the photoemitted electrons in both geometries differs, which has significant influence on the temporal width τ_e of the electron bunch at final velocity. In Refs. [55] and [165] this effect is studied analytically. As a central result of these calculations, in a first-order approximation, the electrons are already sped-up to their final velocity in close vicinity of the tip, i.e., after a few tens of nm of propagation. In comparison, for the plate capacitor the acceleration is continuous resulting in a doubled time-of-flight with respect to the tip photocathode. Moreover, in the planar case, the dependence of τ_e on the initial energy spread is $\tau_e\left(\Delta E\right) \propto \sqrt{\Delta E}$, whereas for the tip geometry $\tau_e \propto \Delta E$ holds true, which is in agreement with Eq. 4.1. After acceleration in a homogeneous electric field and 3 mm propagation, depending on ΔE, the pulse duration τ_e is 50 to 100 times longer than for pulses accelerated by means of a sharp needle emitter [55].

As a consequence, it may be noted that the relatively simple approximation of Eq. 4.1 well describes the dispersion of electron pulses being emitted from sharp metal tips, whereas for the emission from flat photocathodes the acceleration regime has to be considered separately.

However, the total temporal broadening τ_{tot} not just depends on the dispersion due to the finite energy spread $\tau_{\Delta E}$ of the electrons, but also on different trajectories $\tau_{\Delta x}$ due to varying emission sites and directions, possible space-charge effects τ_{sc}, as well as the interaction time $\tau_{h\nu}$ of surface and laser pulse during the emission process. Thus, the overall electron pulse duration can be estimated by [166]

$$\tau_{tot} = \sqrt{\tau_{\Delta E}^2 + \tau_{\Delta x}^2 + \tau_{sc}^2 + \tau_{h\nu}^2} \, . \tag{4.3}$$

To quantitatively take into account $\tau_{\Delta x}$, a thorough consideration of the exact field distribution around the tip and possibly inside an employed lens assembly is necessary. Finite element simulations are a convenient way to do these calculations, as, for example, performed in Refs. [165, 167] and [24].

In addition to the intense acceleration of electron pulses in the static electric field of a biased tip, the lightning rod effect also affects the electron emission process itself by enhancing the oscillating electric field of the incident laser pulse. For a tungsten tip with a radius of curvature of $r = 20$ nm at the apex, this leads to an enhancement of $\eta \approx 3$ to 6 [168]. Higher enhancement factors η are achieved by using smaller tip radii or materials exhibiting a plasmonic resonance at the wavelength of the incident light [161]. The latter, for example, applies for a gold tip of similar curvature irradiated by 800-nm laser pulses leading to enhancement factors ranging from $\eta \approx 8$ to 14 [30, 168]. In both cases, the field enhancement is maximized for light polarized parallel to the tip symmetry axis.

A very useful application of electric field enhancement is the localization of electron emission. In the framework of the classical photoelectric effect, utilizing photon energies $h\nu$ that are larger than the work function Φ of the metal, the emission occurs over the entire illuminated area and the emitted current J is proportional to the intensity I of the incident light (Fig. 4.2a). However, this proportionality only holds for moderate fluences, since for sufficiently high laser intensities, nonlinear effects begin to contribute to the electron emission. For instance, in a multi-photon photoemission process, n photons with $h\nu < \Phi$ may cooperatively cause the emission of an electron if $nh\nu > \Phi$ is fulfilled (Fig. 4.2b). Since the probability for this emission channel increases exponentially with the number n of photons involved, the dependency of the photocurrent J on the light

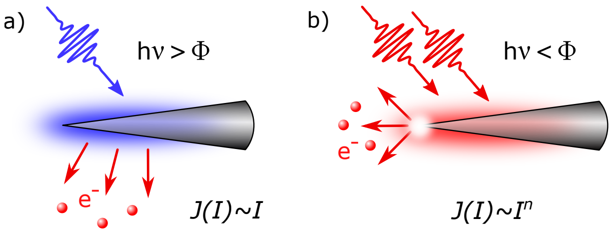

Figure 4.2: Electron photoemission from nanometric metal tips. **a**, The classical photoelectric effect leads electron emission from the entire tip surface. **b**, Multi-photon photoemission Spatially leads to localized electron emission due to electric field enhancement at the tip apex. Figure adapted from Ref. [55].

intensity I obeys $J_n \propto I^n$ [169, 170]. Consequently, multi-photon electron emission occurs more likely at sites of higher light intensity, which in this setup are spatially localized to regions of the highest electric field, namely the tip apex [30].

For even stronger electrical fields above ~1 V/nm, electron emission via optical field emission becomes possible [31]. This differs from multi-photon emission, as the potential barrier for electrons at the metal surface is periodically bent by the strong electric light field. Such a process lowers the effective work function Φ and allows for electron tunneling every optical half cycle. For ultrafast diffraction applications, however, the electron pulses generated this way have the detriment of a broad energy spectrum [171]. Hence, for the ULEED experiment, multi-photon photoemission is the favorable process to generate ultrashort electron pulses, since its maximum excess energy is given by $\Delta E_{max} = nh\nu - \Phi$. In addition, the strong localization of the electron emission site renders nanometric metal tips an ideal source for pulsed electron beams of remarkable quality. In comparison to planar photocathodes, where the emission area is limited to several μm^2 by the laser focus, it is orders of magnitude smaller in the case of optically excited needle emitters. Such strongly localized electron emission significantly improves the transverse coherence length of the generated electron pulses [32].

Hence, for the ULEED experiment presented within this work, a nanometric tungsten tip is utilized as a pulsed electron source driven by $\lambda = 400$ nm, 30-fs laser pulses via two-photon photoemission (Fig. 4.3a). Since the sharp needle photocathodes are fabricated from polycrystalline tungsten wire in a wet etching process, they exhibit a varying work function Φ_W depending on the different crystallographic directions. As Φ_W ranges from 4.47 eV for W(111) over 4.63 eV for W(100) to 5.25 eV for W(110), photoemission with two 400-nm photons leads to a maximum excess energy ranging from $\Delta E_{max} = 0.95$ eV to 1.73 eV [172].

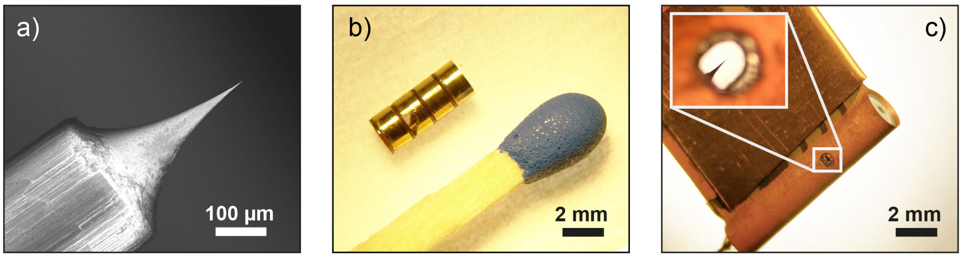

Figure 4.3: **a**, Electron micrograph of the nanometric metal tip used as photocathode. **b**, Electrostatic lens assembly consisting of four electrodes (f.l.t.r.: suppressor, extractor, lens, ground aperture) close to match as a token of scale. **c**, Miniaturized laser-driven electron gun mounted and contacted by means of a FPCB. Inset: Apex of the tip viewed trough the hole for laser irradiation.

4.3 Laser-driven miniaturized electron source

In order to reduce the electron propagation distance while maintaining the visibility of the diffraction pattern, the outer diameter at the front edge of the electron gun is the crucial quantity (cf. Fig. 4.1a). To simultaneously reduce the working distance and the shadowing of the diffraction pattern, in his master's thesis Gero Storeck developed the first generation of a miniaturized pulsed electron source [173]. This gun incorporates a nanometric tungsten tip inside an electrostatic lens assembly for electron acceleration and focusing, and it allows for pulse durations of $\tau_e \approx 10$ ps at $E_{kin} = 200$ eV and 1.4 cm propagation distance. The design of the electrostatic lens assembly consists of four metal apertures, contacted by thin copper wires, and insulating Macor spacers in between. The resulting stack of apertures is held in place by an additional Macor corpus inside a copper housing to provide for a field free exterior.

In the context of the present thesis, this electron gun has been developed further in collaboration with Gero Storeck. The changes mainly concern two aspects of the existing design:

First, to avoid charge accumulation inside the insulating ceramic washers, the combination of thin metal apertures and relatively thick spacers is replaced by cup-like electrodes and polyimide rings for insulation (Fig. 4.3b). The diameter of the electrodes, apertures and distances remains unchanged, which approximately preserves the validity of the previous calculations and numerical simulations performed by Gero Storeck [173].

Second, the solid copper housing and Macor support are switched out for a flexible printed circuit board (FPCB). The FPCB consists of a laser cut polyimide foil with chemically etched contact electrodes on the upside and a copper layer on the backside.

Subsequently, the FPCB is rolled to the desired diameter and both the lens assembly and the needle photocathode are inserted, with particular attention to a correct on-axis alignment (Fig. 4.3c). This way, the FPCB comprises three important functions:

- It serves as a slim elastic housing for the nanometric tip and electrostatic lens.
- The needle and lens assembly are immediately contacted by the circuit paths without any soldering.
- The exterior of the source is maintained field-free by a grounded copper layer on the outside.

Since the FPCB has a thickness of ~170 µm, the outer diameter of the lens assembly of 2 mm is increased by only 17 %, which allows for operational distances down to approximately 5 mm to 8 mm.

However, consisting from several sub-mm-sized components, the presented pulsed electron source represents the current limit of manual assembly. Further gun miniaturization pursued by Gero Storeck requires more involved fabrication techniques, such as optical lithography or focused ion beam (FIB) milling. The result is a complex laser-driven electron source on the µm-scale allowing for sub-mm operational distances and a temporal resolution on the order of one ps [174]. Since it is not yet routinely in use, only a few measurements employing this particular gun were available to support the findings of this work, whereas most of the data presented in Cap. 5 has been recorded utilizing the mm-scale electron source. Hence, the spatio-temporal characterization of the ULEED experiment (Sec. 4.6) will focus on the electron beam properties of the mm-sized electron source presented above.

4.4 Experimental ULEED setup

In the subsequent section, the technical realization of the ULEED experiment is laid out. Analogous to the physical layout, the following paragraphs are thematically divided into optical components, e.g., the fs laser system and the vacuum chamber to provide for clean surfaces.

4.4.1 Laser system and pump probe scheme

In order to study processes occurring at ultrafast timescales, the fs laser system constitutes a key component of the ULEED experiment. It is composed of a pulsed pump laser

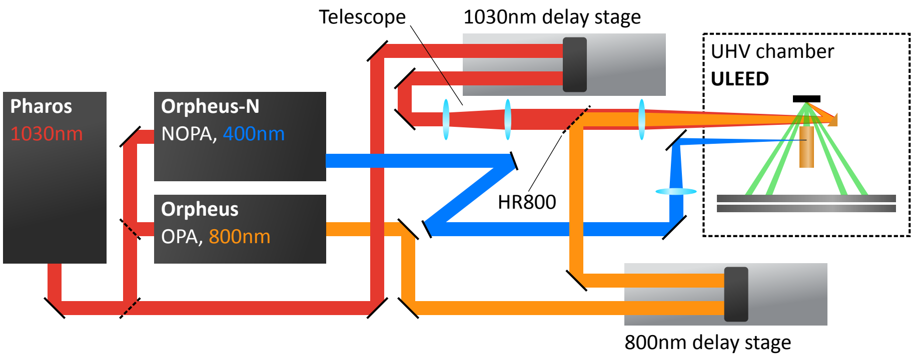

Figure 4.4: Sketch of the femtosecond laser system and the optical beam path used for the ULEED experiment. Image courtesy of J. G. Horstmann.

(Pharos), which incorporates a regenerative amplifier seeded by an internal oscillator. The emitted pulses have a central wavelength of $\lambda = 1030$ nm, a pulse duration of approximately 290 fs, and an energy of 150 µJ. A pulse picker allows one to vary the repetition rate from single shot to 100 kHz leading to a maximum output power of 15 W. Consecutively, the Pharos beam is split up to pump an optical parametric amplifier (OPA, Orpheus) and a non-collinear optical parametric amplifier (NOPA, Orphaus-N) using powers of 6.8 W and 6.45 W, respectively (Fig. 4.4). The remaining 1.54 W of Pharos output power are used to directly excite the sample by focusing it inside the UHV chamber. The time delay Δt to trigger the transient structural dynamics with respect to the electron pulse is set by means of a 30 cm delay stage including a hollow retroreflector.

The wavelengths of the NOPA and OPA can be tuned in the ranges from $\lambda = 250$ nm to 900 nm and $\lambda = 315$ nm to 16000 nm, respectively. In the current configuration, the NOPA is primarily used to generate $\lambda = 400$ nm pulses with a duration of 40 fs and 100 nJ energy, which are focused onto the nanoscopic tungsten tip to generate the electron probe pulses via 2PPE (Fig. 4.5). The OPA can be employed as an alternative source for wavelength-tunable pump pulses including a second delay stage. Since the maximum OPA output power is approximately half of the remaining Pharos pump beam, for the analysis of the structural dynamics at 1T-TaS$_2$ the 1030-nm pulses of the Pharos are used to excite the sample. In a different experimental approach, the OPA can provide for a second pump pulse with a delay Δt relative to the first one, which allows for studying the dynamics of already excited states. However, such pump-pump-probe experiments go beyond the scope this work and are discussed in detail in the work conducted by Theo Diekmann [91].

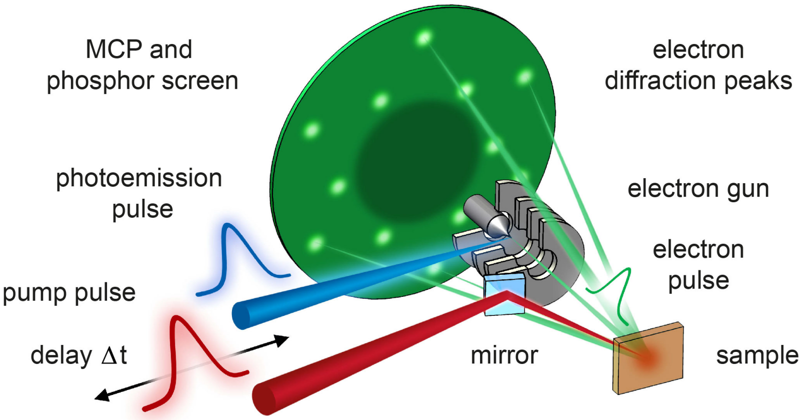

Figure 4.5: Sketch of the ULEED experiment based on an optical-pump, electron-probe scheme. Fs laser pulses (blue) generate ultrashort electron bunches (green) from a nanometric needle emitter via 2PPE, which are subsequently diffracted from a single crystalline sample that is previously excited by intense pump pulses (red). The diffracted electrons are consecutively multiplied by an MCP, post-accelerated and recorded on a phosphorous screen using a high dynamic range camera system.

Finally, both focusing optics right before the vacuum chamber are controlled via piezoelectric positioning elements allowing for few nm accuracy.

After emission from the nanometric photocathode, the electron pulse is subsequently accelerated and focused inside the electrostatic lens assembly, diffracted from the crystalline sample surface and recorded by a circular 77-mm single-electron detector (Fig. 4.5). The latter consists of two microchannel plates (MCP) in chevron configuration (open area ratio 60 %) for electron multiplication and post-acceleration in front of a phosphorous screen. Finally, the resulting diffraction pattern is imaged by a cooled high resolution and high dynamic range (4 Mpx, 16 bit) sCMOS camera and stored for further processing and analysis.

4.4.2 UHV chamber

As every experiment related to surface science, ULEED likewise demands for an extremely clean environment to avoid any kind of surface contamination. To this end, the ULEED experiment is conducted in an ultra high vacuum (UHV) chamber (Fig. 4.6) with a base pressure of $2 \cdot 10^{-10}$ mbar. To conveniently transfer samples into the UHV system, it features a load-lock including a sample storage. The central chamber offers a variety of possibilities for sample preparation and conditioning. These include an argon ion sputtering source for sample cleaning, an electron beam evaporator together with a

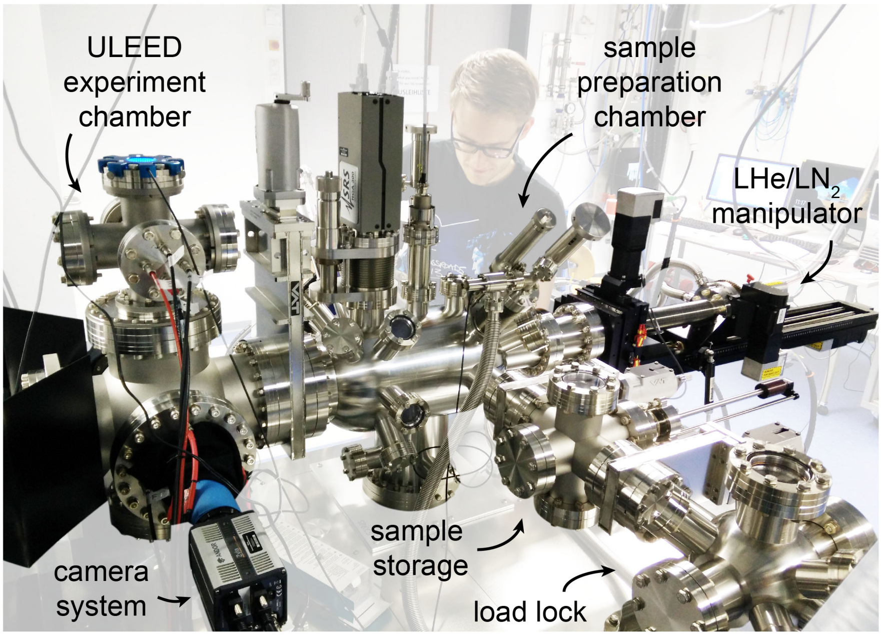

Figure 4.6: UHV chamber to provide for clean surfaces during sample preparation and the time-resolved diffraction measurements.

quartz crystal microbalance for thin film deposition, a gas inlet, a mass spectrometer for temperature programmed desorption (TPD) measurements, as well as conventional LEED setup. A separate chamber part allows for direct current annealing of semiconductor samples and evaporation of organic molecules. After preparation, samples are transferred to the actual ULEED experimental chamber by means of a motorized manipulator. It comprises an electron beam heater and cooling via a continuous-flow cryostat operated with liquid helium or nitrogen, which facilitates time-resolved LEED measurements in a wide temperature range.

4.5 Sample preparation

Provided by the group of Kai Rossnagl at the University of Kiel, the 1T-TaS$_2$ single crystals investigated within this work are grown in a chemical vapor transport process under supervision of Kerstin Hanff.

For this method, high purity tantalum and sulfur are placed in an ampule together with iodine serving as a transport agent. Then, a temperature gradient is applied to the sealed ampule for several weeks leading to vaporization at its hot end and crystallization of the TMDC at its cold end. Typical experimental conditions for the growth of 1T-TaS$_2$ are temperatures of 840°-870° C and a duration of 1000 h [117].

The samples used for the ULEED experiment consist of platelets having a diameter of 1 mm to 3 mm and a few hundred µm thickness. Using an electrically and thermally conductive two-component adhesive (H24, EPO-TEK) the crystals are subsequently glued onto sample holders, transferred into the UHV chamber via the load-lock and cleaved in-situ along its weakly bound layers. To this end an additional ceramic post is glued on top of the sample using the same epoxy adhesive. This method provides for clean single crystalline 1T-TaS$_2$ surfaces of several mm^2 in size, which are thermally coupled well to the bulk and the sample holder, respectively.

4.6 Spatio-temporal characterization of the diffraction setup

The performance of a time-resolved LEED experiment depends on two key characteristics. The first is the spatial resolution given by the emittance or coherence length of the electron beam. Considering the interplay of all experimental components, the spatial resolution is effectively limited by the transfer width of the instrument.
The second important property is the temporal resolution, which defines the timescale of the fastest structural processes that may be analyzed. For a characterization of the ULEED setup, both will be investigated in the following section.

4.6.1 Transfer width

As shown in Sec. 2.1.7, the instrument response function $T(\boldsymbol{k})$ incorporates all flaws that lead to the finite width of diffraction peaks measured at an otherwise perfect and infinitely extended crystal surface. Hence, the function $\mathcal{F}\{T(\boldsymbol{k})\} = t(\boldsymbol{r})$ defines the transfer width w_t, beyond which correlations of the surface are increasingly difficult to analyze. Since $T(\boldsymbol{k})$ not only includes the imperfectness of the electron beam, but also, e.g., spreads caused by the detector system, w_t can be viewed as a lower limit for the transversal electron beam correlation length ξ_t.

To obtain a reasonable approximation for w_t, the sharpest diffraction spots observed with the ULEED setup are assumed to originate from a defect free surface. Figure 4.7a shows an exemplary high-quality diffraction pattern of a single crystalline 1T-TaS$_2$ surface, which is recorded at room temperature with a kinetic energy of 100 eV. It displays six first-order Bragg peaks of the atomic lattice surrounded by numerous first and higher-order satellite spots originating from the long range PLD induced by the NC CDW phase. At the center of the diffraction pattern, the (00) reflex is masked by the shadow of the electron gun.

Fitting the cross section through the, e.g., $(1\bar{1})$ atomic lattice diffraction peak with a pseudo-Voigt profile (Fig. 4.7b and c) yields a full width at half maximum (FWHM) of $\Delta k = (3.0 \pm 0.04) \cdot 10^{-2}$ Å^{-1}. This width can be associated to a real-space distance via $w_t = 2\pi/\Delta k$, which gives the transfer width of $w_t = 21 \pm 3$ nm. Using the definition for the "maximum resolvable distance" $d_{max} = w_t/\sqrt{2a}$ given in Ref. [69] together with the accuracy of $a = 1.3\,\%$ (standard deviation of the fit coefficient) the current setup achieves $d_{max} \approx 128$ nm.

This high spatial resolution is basically attributed to a considerably high signal-to-noise ratio and the high dynamic range of the ULEED experiment. The fruitful combination of both allows for the observation of diffraction peaks spanning three orders of magnitude in intensity within the same diffraction pattern.
For instance, Fig. 4.7d shows a triplet of second-order CDW satellite spots. The brighter two of them are roughly two orders of magnitude weaker than the Bragg peak shown in panel b, and an even fainter one is visible in the upper left corner of panel d. Although the intensity of the former two is already relatively weak, a cross section through them can be fitted very well by means of two Lorentzian profiles. The peak-to-peak distance of $d = 0.096$ Å^{-1} is inversely proportional to the diameter D of the commensurate patches in the NC CDW phase, which amounts to

$$D = \frac{2\pi}{d} \cdot \frac{2}{\sqrt{3}} \approx 7.6\,\mathrm{nm}\,. \tag{4.4}$$

The factor of $2/\sqrt{3}$ arises from to the hexagonal arrangement of the commensurate patches and the resulting value is in good agreement with the 7.3 nm given in Ref. [115].
For sake of completeness, the transverse rms electron beam emittance ε_{rms} introduced in Sec. 2.1.7 can be deduced from the beam diameter σ_x and its angular spread σ_α. Using the width $\sigma_x = 212$ µm of the Bragg peak depicted in Fig. 4.7b on the phosphorous screen, the source-to-detector distance $d = 8$ cm and the electron energy of $E = 100$ eV, one yields $\varepsilon_{rms} \approx 11.3\,\mu\mathrm{m} \cdot \mathrm{mrad}$, which is several orders of magnitude larger than what can be achieved in, e.g., a time-resolved TEM [33], but still represents a reasonable value considering the basic components of this ULEED setup.

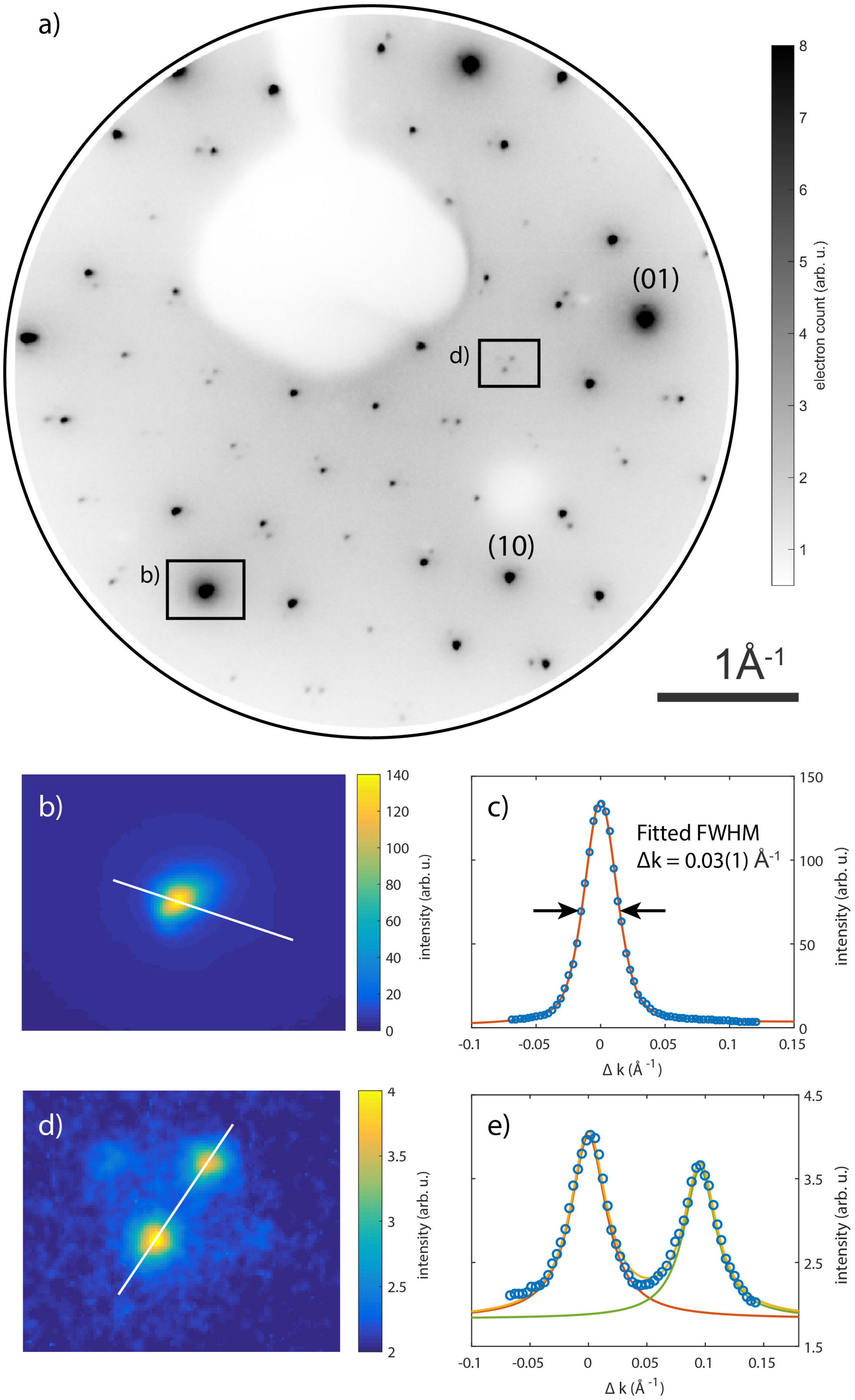

Figure 4.7: Spatial characterization of the ULEED setup. **a**, A static diffraction pattern of the 1T-TaS$_2$ surface recorded with pulsed electrons from the mm-sized source showing the NC CDW phase (E_k=100 eV, 180 s integration). **b** and **c**, Close up and cross section of the $(1\bar{1})$ atomic lattice diffraction peak. A pseudo-Voigt profile fitted to the data exhibits a FWHM of $\Delta k = 0.03(1)$ Å^{-1}. **d**, Close up displaying a triplet of second-order CDW satellite spots. **e**, A cross section through the two brighter diffraction peaks shown in **d** is fitted with the sum of two Lorentzian profiles.

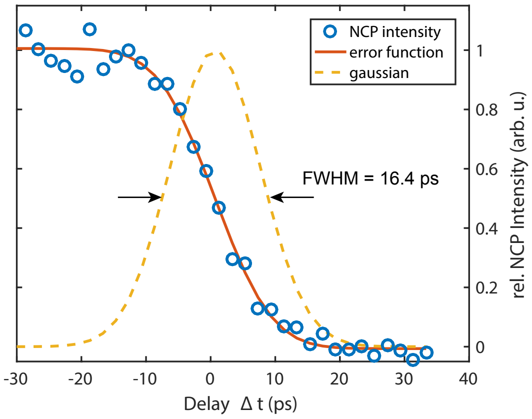

Figure 4.8: Electron pulse duration measured via the structural suppression of the NC CDW phase at a kinetic energy of $E_k = 100$ eV. Assuming an instantaneous sample excitation, the measured signal can be fitted by an error function, which allows for easily determining the width of the underlying Gaussian electron pulse profile.

4.6.2 Temporal resolution

To determine the temporal resolution of an optical-pump, electron-probe scheme, measurement of the electron pulse duration at the sample position is necessary. This can be done with several direct or indirect methods, which all provide for a cross correlation between the optical pump pulse and the incident electron pulse. Subsequently, the duration of the latter can be obtained via deconvolution. One example for a direct interaction is the Kapitza-Dirac effect [175, 176]. This experiment features interesting similarities to LEED, as the incident electrons are diffracted at a grating generated by a standing wave of light. However, this approach requires a very tightly focused electron beam as well as optical power densities on the order of 10^{15} W/m^2 [176], which are hard to achieve with a standard fs laser system.

Indirect measurements, on the other hand, encompass the modification of the electron energy via interaction with optical near fields (i.e., photon-induced near-field electron microscopy, PINEM) [153, 177], the deflection of the electron beam by a photoemitted cloud of space charge (transient electric field effect, TEF) [174, 178, 179], or the fastest structural response of a material observable after optical excitation [28, 37, 180].

In this work, the electron pulse duration is determined via the suppression of NC CDW phase in 1T-TaS$_2$ after intense laser irradiation. Since both the optical excitation and the phase transition itself occur within a few hundred fs [148], on the timescale of the electron pulse they may be approximated as a delta peak and a Heaviside function, respectively. Hence, assuming the temporal profile of the electron pulse to be a Gaussian, its convolution with the quasi instantaneous phase transition yields an error function, which is fitted to the normalized delay-dependent intensity of the NCP diffraction peaks (cf. Fig. 4.8). Under optimal conditions for $E_k = 100$ eV ($U_S = -440$ V, $U_E = +100$ V, $U_L = +361$ V, $d \approx 6$ mm propagation) the FWHM of the corresponding Gaussian profile leads to an electron pulse duration of $\tau_e = 16.4$ ps, which is mainly limited by the sample-source distance. Although this temporal resolution is not fast enough to resolve processes occurring on the few hundred fs timescale, it is still well suited to investigate, e.g., the formation of adsorbate superstructures, order-disorder phenomena, or the recovery to pre-excitation states. Specific examples could be Corannulene adsorbed on Cu(111) forming temperature-dependent superstructures [181], or, as will be discussed in the following chapter, the evolution of defects in the newly created IC CDW phase of 1T-TaS_2.

In comparison, the µm-sized electron gun developed by G. Storeck allows for a temporal resolution of $\tau_e = 1.3$ ps at $E_k = 80$ eV and $d = 400$ µm measured using the TEF effect [174], or $\tau_e = 1.4$ ps obtained from the suppression of the NC CDW phase at a kinetic energy of $E_k = 50$ eV [37].

Chapter 5

Ultrafast structural dynamics at the surface of 1T-TaS$_2$

Subsequent to the gun characterization using quasi-static diffraction patterns recorded with pulsed electrons, this chapter focuses on the structural dynamics at the surface of single crystalline 1T-TaS$_2$. To this end, the changes of the atomic lattice structure associated with the transition from the room-temperature NC CDW phase to the high temperature IC phase are traced by means of ULEED. First, the intensities of both the atomic lattice Bragg peaks and CDW superstructure peaks are studied as a function of time delay Δt and optical pump fluence F. Second, the ICP diffraction spot profiles are analyzed to quantify the transient structural disorder in the newly created IC CDW phase.

5.1 NC-IC phase transition mapped by ULEED

To repeatedly drive the 1T-TaS$_2$ surface from the NC to the IC phase, it is excited by intense laser pulses having a central wavelength of λ =1030 nm and duration of τ ≈290 fs. Since the stroboscopic pump-probe approach of ULEED requires the sample to return to its ground state between two subsequent pump pulses, the experiment is operated at a repetition rate of 25 kHz. Additionally, it is important to homogeneously excite the probed surface area. Therefore, the focus of the pump laser is expanded to a diameter of ~300 µm (FWHM), while the mm-sized gun permits focusing of the electron pulses down to ~100 µm (FWHM).

As set out theoretically in Sec. 3.1, both the NC and the IC CDW phase are characterized by PLDs which manifest themselves very differently in real space and reciprocal space,

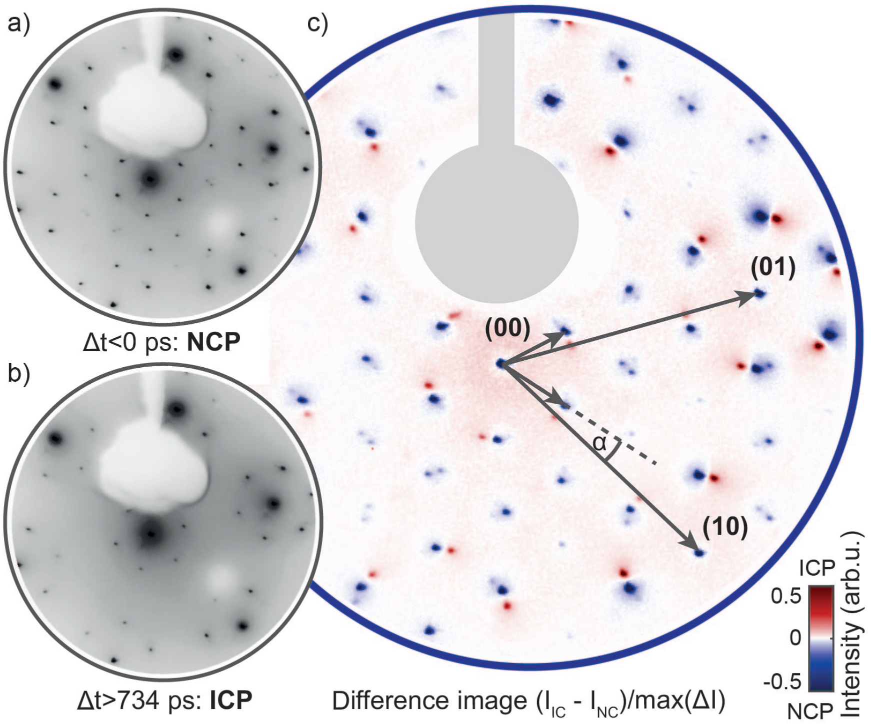

Figure 5.1: NC-IC CDW phase transition mapped in reciprocal space. **a**, LEED diffraction pattern of the nearly commensurate CDW phase measured before time zero ($E_k = 100$ eV, 180 s integration). **b**, Reciprocal lattice of the optically induced incommensurate CDW phase ($\Delta t > 734$ ps). **c**, Normalized difference image of the diffraction patterns shown in panels **a** and **b**. To illustrate the changes of the CDW satellite spots, the NC and IC phase are depicted in blue and red, respectively. During optical excitation the NCP peaks are strongly suppressed, whereas the ICP diffraction peaks appear at a relative rotation angle of $\alpha \approx -12°$. In comparison, the Bragg peaks of the atomic lattice are just suppressed due to lattice heating.

respectively. Hence, the transition between both phases has a drastic effect on the ULEED diffraction patterns, which is displayed in Fig. 5.1: Panels a and b show diffraction images of the NC and IC CDW phase recorded before and after the phase transition, respectively, whereas a normalized difference image of both diffraction patterns is presented in c. Here, the suppressed NC phase is shown in blue, while the emerging IC CDW phase is depicted in red. As the most striking feature, Fig. 5.1c illustrates that the IC phase satellite diffraction spots appear at a position rotated by $a \approx -12°$ relative to the NCP diffraction peaks. Additionally, higher order CDW satellite peaks are absent in the IC phase and the Bragg peaks of the atomic lattice are diminished due to an increased lattice temperature. To quantify these transient changes in more detail, the integrated intensity of both the NC and IC CDW peaks, as well as the atomic lattice Bragg peaks (BP) and the background (BG) are evaluated within disk-like areas as a function of delay time Δt for ten incident pump fluences ranging from $F = 0.6$ mJ/cm² to 5.7 mJ/cm². A detailed description of the intensity evaluation procedure is given in Sec. A.2 of the appendix.

As depicted in Fig. 5.2a, below $F = 2.8$ mJ/cm² the intensity of the NCP satellite peaks is decreased by up to 25 %, due to thermal heating of both the atomic lattice and the CDW lattice. In contrast, above $F \approx 3.4$ mJ/cm² the NCP diffraction peaks vanish within the temporal resolution of the electron source.

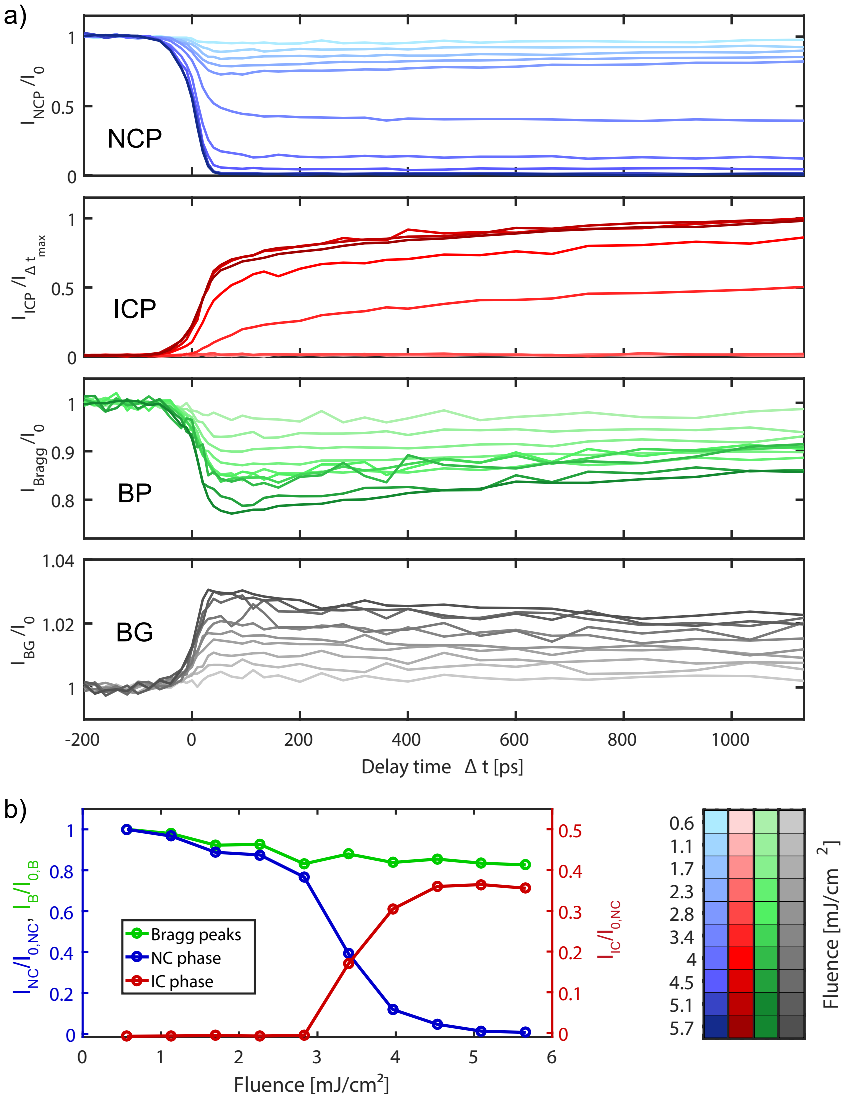

Figure 5.2: Evaluation of the delay-dependent diffraction spot intensities of the NCP, ICP, atomic lattice Bragg peaks and the background, respectively. **a**, Integrated diffraction peak intensities $I(\Delta t)$ measured for ten different incident pump fluences (bottom right). **b**, Fluence dependence of the measured CDW and Bragg diffraction peak intensities evaluated at $\Delta t > 1.1$ ns and normalized to I_{NC} and I_B at negative time delays $\Delta t < 0$, respectively.

Simultaneously, the intensity of the ICP diffraction peaks rapidly increases within a few tens of ps, which are followed by a slower rise continuing for some hundred ps. Concurrently, the intensity of the atomic lattice Bragg peaks is suppressed and the background of the diffraction pattern slightly increases, which both is a consequence of the increased lattice temperature.

Since the thermal relaxation occurs on the ns timescale (cf. evolution of Bragg peaks and background in Fig. 5.2), evaluating the CDW diffraction peak intensities at $\Delta t = 1100$ ps allows for a quasi static fluence-dependent measurement of the phase transition. The sharp fluence threshold at $F \approx 3.4$ mJ/cm^2 in Fig. 5.2b verifies a relatively homogeneous excitation of the surface area probed by the low-energy electron pulses.

5.2 Spot profile analysis

In the previous section, the focus has been laid on the temporal evolution of the integrated diffraction peak intensities. However, neither the difference image nor the delay-dependent measurements of the integrated intensity are sensitive to changes of the diffraction spot profiles. To verify that the shape of certain diffraction peaks actually changes over time, the integral and maximum of the diffraction peak intensity are compared for varying time delay Δt. Accordingly, the ratio $I_{int}\left(\Delta t\right)/I_{max}\left(\Delta t\right)$ is determined for both CDW and atomic lattice diffraction peaks by averaging over the three highest pump fluences and displayed in Fig. 5.3.

While I_{int}/I_{max} remains relatively constant over time for both the NCP and the atomic lattice Bragg peaks, it exhibits a distinct decrease for the ICP diffraction peaks after excitation. In other words, the maximum diffraction spot intensity of the IC phase increases faster than the corresponding integrated intensity. It is suspected that right after the phase transition, a substantial amount of ICP diffraction spot intensity is already present and spread out over a relatively large region in reciprocal space. Subsequently, the peaks are subject to a narrowing, thus causing a growth of I_{max}. For this reason, it is desirable to perform a detailed spot profile analysis to quantify the structural dynamics of the ICP, which lead to the surmised diffraction peak narrowing.

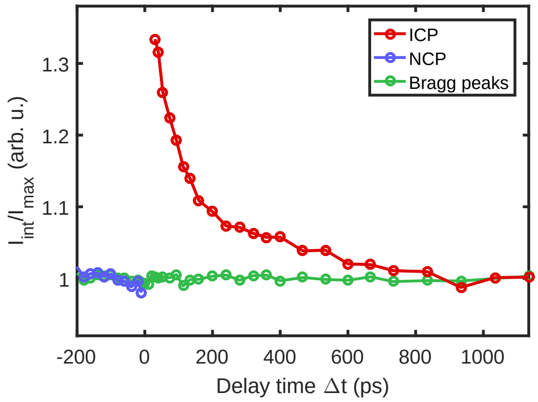

Figure 5.3: Ratio $I_{int}\left(\Delta t\right)/I_{max}\left(\Delta t\right)$ of the integrated and the maximum diffraction peak intensity for both CDW phases and the atomic lattice Bragg peaks. It indicates a reshaping of the IC CDW satellite spots directly after the phase transition.

As described in Sec. 2.1.7, the diffraction peak profile of the measured intensity $I_m\left(\boldsymbol{k}\right)$ is given by the convolution of the instrument response function $T\left(\boldsymbol{k}\right)$ and the intensity $I\left(\boldsymbol{k}\right)$ scattered at the surface assuming an infinitely sharp and collimated electron beam. Hence, to determine the contribution of the IC phase to the time-dependent width of the diffraction peaks, a deconvolution of $I\left(\boldsymbol{k}\right)$ and $T\left(\boldsymbol{k}\right)$ is necessary. If both $I\left(\boldsymbol{k}\right)$ and $T\left(\boldsymbol{k}\right)$ are either Gaussian or Lorentzian profiles, the FWHM w_m of $I_m\left(\boldsymbol{k}\right)$ is given by $\sqrt{w_{g1}^2 + w_{g2}^2}$ or the simply the sum $w_{l1} + w_{l2}$ of the two components, respectively. Here, however, the instrument function of the mm-sized electron gun is approximated by means of the sharpest atomic lattice Bragg peaks, which are well reproduced by Voigt-profiles (Sec. 4.6.1), and the ICP diffraction spots are assumed to exhibit a Lorentzian peak shape due to a random distribution of defects. Therefore, we resort to a numerical convolution

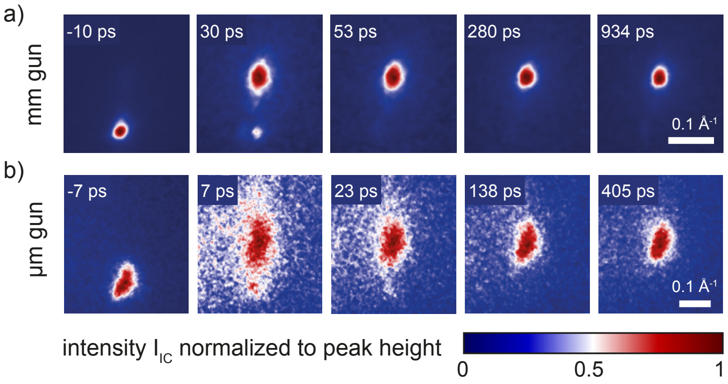

Figure 5.4: Temporal evolution of two exemplary ICP diffraction peaks after optical excitation recorded with the mm-sized (**a**) and µm-sized electron source (**b**), respectively. The diffraction peaks shown are normalized to its respective maximum value to accentuate their approximate FWHM (white region of color scale). Close to time zero and for $\Delta t < 0$, the corresponding NCP diffraction peaks are visible at the bottom of each panel as well.

of the measured (and normalized) instrument function (e.g., given by the $(1\bar{1})$ Bragg peak) with the two-dimensional analytic Cauchy distribution

$$C_{2D}\left(\boldsymbol{k}\right) = \frac{1}{2\pi\sigma_r\sigma_a}\left(1+\left(\frac{k_r}{\sigma_r}\right)^2+\left(\frac{k_a}{\sigma_a}\right)^2\right)^{-\frac{3}{2}} \tag{5.1}$$

which is fitted to the ICP diffraction spots for each delay time Δt. As illustrated in Fig. 5.4, for early delay times, the broadened ICP diffraction peaks appear elongated in azimuthal direction with respect to the adjacent atomic lattice Bragg peak. Therefore, the rotation angle φ of the elliptical profile C_{2D} is adjusted using the associated Bragg peak and remains fixed during the fit procedure. Here, σ_r and σ_a serve as fit parameters that correspond to the IC CDW contribution to the radial and azimuthal width of the ICP diffraction peaks. Further fit parameters include the peak amplitude, the two-dimensional displacements and a two-dimensional linear background to compensate for a possibly present tail of the NCP satellite spot close-by. Finally, the corresponding FWHMs $w_{r,a}$ are obtained via $w_{r,a} = 2\sigma_{r,a}\sqrt{2^{2/3}-1}$.

Since both w_r and w_a exhibit a similar temporal behavior (cf. Appendix A.3), the evolution of a spatially averaged overall contribution to the width of the IC phase diffraction peaks is given by the geometrical mean $w_{IC} = \sqrt{w_r w_a}$, and the resulting curve is displayed in Fig. 5.5. Primarily, these results include four measurements with the mm-sized electron gun for the four highest optical pump fluences above the threshold of ~3.4 mJ/cm² (blue to yellow circles), which are averaged over the six brightest ICP diffraction peaks available. However, due to the temporal resolution of this pulsed electron source, the evolution of the ICP diffraction spots can be only evaluated for delay times $\Delta t \geq 20$ ps. To corroborate the results of the mm-sized source, Fig. 5.5 also includes one dataset recorded by Gero Storeck using the µm-sized electron gun, which allows for the observation of ICP diffraction peaks already at $\Delta t \geq 2$ ps (red circles)[1].

As can by readily seen in Figs. 5.4 and 5.5, directly ensuing the phase transition, the ICP diffraction spots appear as broad peaks which rapidly get narrower over time delay Δt. More precisely, the contribution of the IC CDW to the peak width is reduced by a factor of three within 380 ps as it decreases from $w_{IC} = 0.026\,\text{Å}^{-1}$ at 20 ps to $w_{IC} \leq 0.008\,\text{Å}^{-1}$

---

[1] In this measurement, the shape of the NC and IC CDW diffraction peaks turns out relatively heterogeneous over the whole diffraction pattern due to to surface imperfections and stray fields in the vicinity of the gun. Accordingly, instead of using the sharpest Bragg peak as a global instrument function, each ICP peak is assigned an individual instrument function, i.e., a normalized representation of the associated NCP satellite spot, which also incorporates the local distortions, but is not affected by peak broadening.

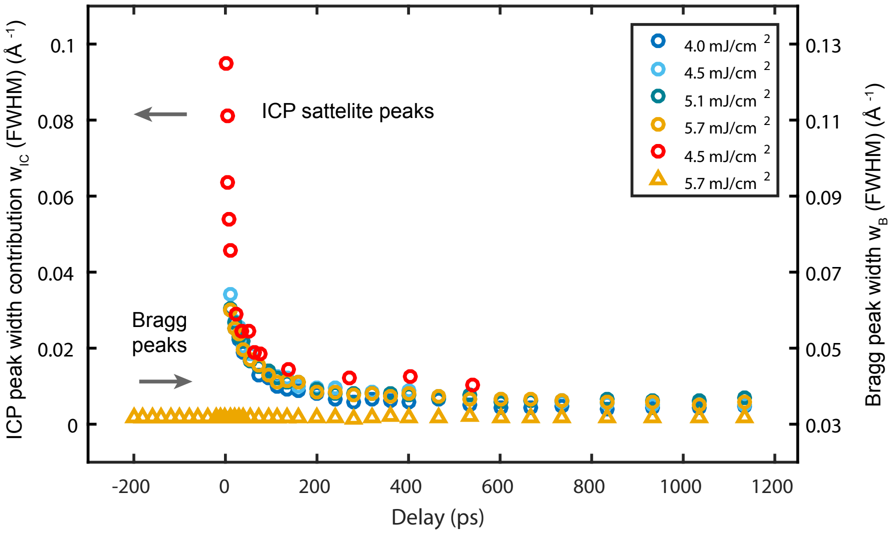

Figure 5.5: Evolution of the time-dependent CDW contribution to the width (FWHM) of the ICP satellite diffraction peaks obtained via two-dimensional fitting. The shown data consists of four measurements using the mm-sized electron source and four incident fluences above the threshold of 3.4 mJ/cm² (blue and yellow circles), as well as one dataset recorded by Gero Storeck using the µm-sized electron gun and a moderate fluence of $F \approx 4.5$ mJ/cm² (red circles). The width of the atomic lattice Bragg peaks is shown for comparison (yellow triangles). As the ICP diffraction spots get narrower over time, their width approaches the one of the atomic lattice Bragg peaks, which is not affected by the CDW phase transition.

for $\Delta t \geq 400$ ps. In the limit of long delay times, the width of the narrowing ICP satellite spots approaches the value $w_B = 0.031\,\text{Å}^{-1}$ obtained for the atomic lattice Bragg peaks[2], which are shown for one exemplary fluence (yellow triangles).

5.3 Summary and discussion

Primarily, following intense laser irradiation above 3.4 mJ/cm², the NC CDW vanishes within the temporal resolution of both electron sources employed. In comparison, UED and XRD measurements at bulk 1-TaS$_2$ indicate a suppression of the room-temperature NC phase on the timescale of 300-400 fs [148, 150], which is also a reasonable value for the surface, as individual 1-TaS$_2$ layers are only weakly coupled. Hence, further work on shortening the achievable electron pulse duration is necessary to effectively resolve the decay of the NC CDW phase.

---

[2] Simultaneously to the ICP diffraction spots, the atomic lattice Bragg peaks are fitted with two-dimensional Voigt profiles. Subsequently, the corresponding averaged FWHM w_B is acquired numerically. The width of the atomic lattice Bragg peaks turns out independent of time delay Δt and the applied pump fluence F.

As a second consequence of the phase transition, ICP diffraction peaks appear at positions rotated by ~12° relative to the decaying NCP spots. Measurements using the mm-sized electron source (Fig. 5.2) indicate a fast rise of the integrated intensity I_{IC} shortly after time-zero up to $\sim 75\,\%$ of the signal recorded at 1 ns. This rapid surge of I_{IC} is followed by a slower increase on the timescale of a few hundred ps. The latter growth of I_{IC} may be attributed to an elevated surface temperature, which cools on the ns timescale superimposed by a contribution of IC CDW phasons, which lower the CDW diffraction peak intensity via an additional Debye-Waller factor. This is corroborated by measurements of T. Diekmann [91], which indicate a phason temperature T_ϕ that is substantially higher than the corresponding temperature T_p of the phonon system after optical excitation. In his measurements, the relaxation of T_ϕ occurs within a few hundred ps, comparable to the ICP intensity increase shown in Fig. 5.2.

Moreover, the time frame directly following the CDW phase transition exhibits intriguing structural dynamics with respect to the shape of the emerging ICP satellite spots. Specifically, the ICP diffraction peaks are suspected to be broadened shortly after time-zero and to subsequently tighten over time, due to a decreasing ratio of the integrated and maximum diffraction peak intensities I_{int} and I_{max}, respectively. This narrowing process is confirmed and quantified by a delay-dependent spot profile analysis that utilizes a two-dimensional deconvolution to separate the CDW induced peak broadening from the instrument function. Consequently, the strongly extended diffraction spot profiles ensuing the CDW phase transition indicate a considerable amount of disorder in the newly created IC CDW phase, which significantly reduces the CDW correlation length ξ_{IC}. The latter is linked to the width w_{IC} via

$$\xi_{IC}\left(\Delta t\right) = \frac{2\pi}{w_{IC}\left(\Delta t\right)}\,. \tag{5.2}$$

Hence, the ICP correlation length increases as the CDW disorder declines over time. For instance, the correlation length is $\xi_{IC} = 24$ nm at $\Delta t = 20$ ps and grows to $\xi_{IC} \geq 78$ nm for $\Delta t \geq 400$ ps. To obtain a comprehensive overview of the temporal evolution of $\xi_{IC}\left(\Delta t\right)$, Fig. 5.6 shows a double-logarithmic plot of the correlation length versus delay time. As $\xi_{IC}\left(\Delta t\right)$ exhibits a linear increase in the double-logarithmic plot, its growth obeys a power-law behavior, i.e.,

$$\xi_{IC}\left(\Delta t\right) \propto \Delta t^{m}. \tag{5.3}$$

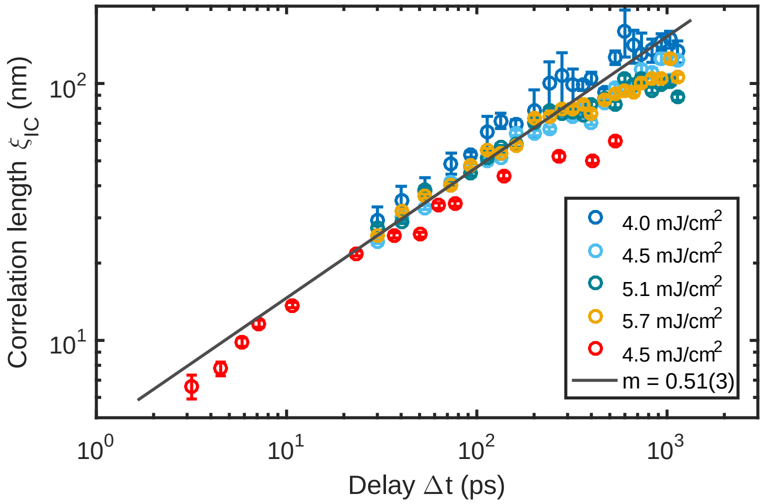

Figure 5.6: Double-logarithmic plot of the IC CDW correlation length ξ_{IC} vs. time delay Δt. The first four pump fluences (blue to yellow circles) correspond to a set of measurements using the mm-sized electron gun. The fifth dataset (red circles) resembles a measurement conducted by G. Storeck by means of the µm-sized electron source.

The exponent m is determined by a linear fit to the logarithmized data and delay times. Because the increase of $\xi_{IC}\left(\Delta t\right)$ tends to saturate for long delay times, the time interval for the regression is restricted to $\Delta t \leq 405$ ps. By this means, the linear fit yields a growth exponent of $m = 0.51 \pm 0.03$. To further discuss the physical meaning of this power-law behavior, a deeper understanding of the nature and the origin of the IC CDW disorder is required, which will be addressed in the remainder of this section and the next chapter.

Usually, defects in the crystal lattices of bulk material or surface superstructures can be attributed to a random distribution of uncorrelated domains (cf. Sec. 2.2.1) or point-like defects, such as impurities or vacancies. For CDWs, the situation may be somewhat different. Here, the existence of domain walls requires a certain degree of commensurability between the CDW and the underlying atomic lattice, as described in Sec. 2.4.3. This way, the elastic energy required for a domain wall can be compensated by locking the CDW to the atomic lattice inside a specific domain. An instructive example for such kind of CDW is the NC phase featuring finite phase jumps (discommensurations) which separate commensurate patches. In comparison, the IC CDW phase can be considered as “free floating” with respect to the atomic lattice provided that CDW pinning at lattice impurities can be neglected. Hence, sharp phase jumps (or domain walls) between different sites of the sample will immediately flatten out, leaving behind regions of slowly varying phase, which may be viewed as frozen-in or $\omega = 0$ phasons.

However, in contrast to domain walls, the “free floating” IC CDW phase permits the existence of topological point defects inside the hexagonal CDW lattice (Sec. 2.4.3). Similar to a domain structure, such topological defects have immediate influence on the translational correlation function and limit ξ_{IC}. Thus, the strongly broadened ICP diffraction peaks following the CDW phase transition indicate a large number of topological defects in the CDW lattice. Accordingly, the observed increase of ξ_{IC} may be rather attributed to a decreasing defect density ρ_d than a domain coarsening process including well defined domain walls.

Possible mechanisms that allow for the appearance of dislocation defects in a hexagonal CDW lattice are twofold. First, previously bound dislocation pairs of opposite winding number may be released thermally, as predicted by KTHNY-theory (Sec. 2.4.2). Alternatively, topological defects in the IC CDW might arise from the NC-IC phase transition itself. As the sample is globally driven above the ICP transition temperature in the probed region, phase differences between various sites of emerging IC CDW order are inevitable. In the process of leveling out these phase inconsistencies, dislocation defects appear within circularly linked areas of the IC CDW lattice.

To further investigate the role of topological defects for the highly disordered IC CDW phase, the following chapter presents a numerical simulation of the ICP relaxation dynamics in real space using a time-dependent Ginzburg-Landau approach.

Chapter 6

Simulation of IC CDW dynamics

The previous experimental results indicate that shortly after the NC to IC CDW phase transition, the charge modulation at the surface of 1T-TaS$_2$ is subject to a substantial amount of transient disorder. To elucidate the temporal evolution of this effect, a numerical model for the dynamics of the high-temperature CDW phase is presented in this chapter. The triple IC CDW is described in terms of a Landau free-energy functional, which enables introducing equations of motion for the three complex order parameters $\psi_j\left(\boldsymbol{r},t\right)$ by means of a time-dependent Ginzburg-Landau approach. The numerical solution of the resulting coupled differential equations is realized via Matlab using a split-operator Fourier method.

6.1 Landau free-energy functional for triple CDWs

A widely used starting point to study the behavior of systems undergoing an order-disorder phase transition at a critical temperature T_c is the phenomenological Landau theory [78]. In this mean field approach, the so-called Landau free energy F of the system is expressed in terms of a suitably chosen order parameter $\psi\left(\boldsymbol{r},t\right)$ which is $\psi=0$ for $T>T_c$ and $\psi\neq0$ for $T<T_c$. For example, in the Ising model of a ferromagnet, a possible order parameter is the local magnetization density $m\left(\boldsymbol{r},t\right)$. The free-energy functional of the corresponding Ginzburg-Landau form then reads [182]

$$F=\int \mathrm{d}\boldsymbol{r}\left[\frac{1}{2}\left(\nabla m\right)^2+V\left(m\right)-Hm\right]\,, \tag{6.1}$$

where $V\left(m\right)$ represents a temperature-dependent double well potential with minima corresponding to the two equilibrium states of the sample. The gradient term in Eq. 6.1

incorporates the elastic energy stored in the transition region between two adjacent areas of opposite magnetization [100], and H accounts for a potentially present external magnetic field.
To analyze the evolution of the order parameter for a system driven out of equilibrium, a possible approach is to assume that locally the rate of displacement of the order parameter, e.g., $\dot{m} = \mathrm{d}m/\mathrm{d}t$, is directly proportional to the thermodynamic force given by the variational derivative $\delta F/\delta m$ of the free-energy functional [182], i.e.,

$$\frac{\mathrm{d}\psi}{\mathrm{d}t} = -\frac{\delta F}{\delta \psi}\,. \tag{6.2}$$

This is also known as the time-dependent Ginzburg-Landau equation of motion for non-conserved scalar order parameters [100, 182]. For simplicity, the proportionality constant determining the time scale of the dynamics in Eq. 6.2 has been absorbed into the time derivative.

This concept may be adopted to also describe the non-equilibrium dynamics of the IC CDW in 1T-TaS$_2$. To this end, it is advantageous to use the charge-density modulation $\alpha(\boldsymbol{r})$ as the natural order parameter (cf. Sec. 2.3), which can be described in terms of three complex components $\alpha(\boldsymbol{r}) = \mathrm{Re}\left[\psi_1(\boldsymbol{r}) + \psi_2(\boldsymbol{r}) + \psi_3(\boldsymbol{r})\right]$ [79]. The resulting Landau free-energy functional F_{IC} used within this work is a simplified version of the one introduced by McMillan in Ref. [79] and studied by Nakanishi and Shiba in Refs. [121] and [183], respectively. F_{IC} is composed of four contributions, which will be described in more detail below. The complete free-energy functional reads

$$\begin{aligned} F_{IC} \;=\; & \int \mathrm{d}\boldsymbol{r} \Bigg[\sum_j a \left|\left(\boldsymbol{q}_j \cdot \nabla - i\boldsymbol{q}_j^2\right)\psi_j\right|^2 + \sum_j b \left|\boldsymbol{q}_j \times \nabla\psi_j\right|^2 \\ & + \sum_j c\left(\frac{2}{3}|\psi_j|^3 - g\left(1-\frac{d}{c}\right)|\psi_j|^2\right) + d\left(\psi_1\psi_2\psi_3 + \psi_1^*\psi_2^*\psi_3^*\right)\Bigg], \end{aligned} \tag{6.3}$$

where $\boldsymbol{q}_j$ $(j = 1, 2, 3)$ denotes the equilibrium wavevectors of the three complex order parameters ψ_j, which are rotated by an angle of 120° relative to each other.

The first two terms of the free-energy functional F_{IC} adjust the local wavelength and direction of $\psi_j(\boldsymbol{r}, t)$, respectively, to be ideally the value given by $\boldsymbol{q}_j$. Hence, the energy cost associated with an imperfect periodicity or alignment of ψ_j is proportional to two independent elasticity constants, which are given by the coefficients a and b, respectively [79].

The third term in Eq. 6.3 balances the amplitude $|\psi_j|$ of the three complex contributions to the CDW modulation. It adjusts $\psi_j\left(\boldsymbol{r},t\right)$ in a way that $|\psi_j|$ converges to a finite value g for all three contributions.

Finally, the fourth term of F_{IC} can be considered as a phasing energy. Accordingly, in order to form rotationally symmetric charge accumulations, the phasing energy minimizes if the complex phases $\varphi_j = \arg\left(\psi_j\right)$ add up to an integer multiple of 2π (cf. Sec. 2.3). Furthermore, the phasing term constitutes the sole coupling between the three complex contributions to the charge-density modulation $\alpha\left(\boldsymbol{r}\right)$.

In this context, the coefficients c and d determine the strength of the amplitude and phasing term of F_{IC}, respectively, while the ratio of a and b, defines the nature of the pitchfork dislocations in each complex order parameter ψ_j. Since a and b are proportional to the half axes of the elliptical dislocations cores, for $a \ll b$ the dislocations prefer to move parallel to its Burgers vector (glide), whereas for $a \gg b$ the defects rather slide perpendicular to the associated Burgers vector (climb) [99].

Extending the equation of motion (Eq. 6.2) to complex order parameters, it should be noted that the free-energy F is a real quantity and depends on $|\psi|^2 = \psi\psi^*$. Therefore, Eq. 6.2 then reads

$$\frac{\mathrm{d}\psi}{\mathrm{d}t} = -\frac{\delta F}{\delta\psi^*}\,. \tag{6.4}$$

Hence, the temporal behavior of the three complex order parameters $\psi_j\left(\boldsymbol{r},t\right)$ with $j = 1,2,3$ is determined by a set of three coupled non-linear partial differential equations (PDE), which are given by

$$\begin{aligned}\frac{\delta F_{IC}}{\delta\psi_j^*} \quad = \quad & -a\left(\boldsymbol{q}_j\cdot\nabla - \boldsymbol{i}\boldsymbol{q}_j^2\right)^2\psi_j \,+\, b\left(\left(\boldsymbol{q}_j\cdot\nabla\right)^2 - \boldsymbol{q}_j^2\Delta\right)\psi_j \\ & \qquad\qquad +\,c\left(|\psi_j| - g\left(1-\frac{d}{c}\right)\right)\psi_j \,+\, d\left(\psi_{j+1}^*\psi_{j+2}^*\right) = -\frac{\mathrm{d}\psi_j}{\mathrm{d}t}\,.\end{aligned} \tag{6.5}$$

Since an analytic solution of Eq. 6.5 is infeasible, the temporal evolution of $\psi_j\left(\boldsymbol{r},t\right)$ will be studied numerically. To this end, the numerical procedure and its results are discussed in detail in the remainder of this chapter.

6.2 Numerical implementation

Split-operator Fourier method

Careful consideration of Eq. 6.5 yields striking similarity to the classical nonlinear Schrödinger equation (NLSE), which, e.g., is used to describe the propagation and dispersion of a particle wave function and given by

$$i\hbar\frac{\partial\psi}{\partial t} = -\frac{\hbar^2}{2m}\frac{\partial^2\psi}{\partial x^2} + \gamma\left|\psi\right|^2\psi\,. \tag{6.6}$$

A common way to numerically solve the NLSE is the so-called *split operator Fourier method* (SOFM) [184, 185]. This approach may be also used to analyze the temporal evolution of the three coupled complex order parameters $\psi_j\left(\boldsymbol{r},t\right)$ given by Eq. 6.5, as will be shown in the following paragraph.

To solve the coupled equations of motion in Eq. 6.5, the latter are split into three parts each, of which two terms depend linearly and nonlinearly on ψ_j, plus a third constant term [186]. That is

$$\frac{\partial\psi_j}{\partial t} = \hat{D}\psi_j + \hat{N}\psi_j + \hat{C}\,, \tag{6.7}$$

where $\hat{D}$, $\hat{N}$and $\hat{C}$ denote a dispersive, nonlinear and constant operator, respectively. Hence, the three parts are given by

$$\frac{\partial\psi_j}{\partial t} = \hat{D}\psi_j = \left[a\left(\boldsymbol{q}_j\cdot\nabla - i\boldsymbol{q}_j^2\right)^2 - b\left(\left(\boldsymbol{q}_j\cdot\nabla\right)^2 - \boldsymbol{q}_j^2\Delta\right)\right]\psi_j\,, \tag{6.8}$$

$$\frac{\partial\psi_j}{\partial t} = \hat{N}\psi_j = -c\left(\left|\psi_j\right| - g\left(1-\frac{d}{c}\right)\right)\psi_j\,, \tag{6.9}$$

$$\frac{\partial\psi_j}{\partial t} = \hat{C} = -d\left(\psi_{j+1}^*\psi_{j+2}^*\right)\,. \tag{6.10}$$

Then, propagating Eq. 6.5 for a small time step Δt requires successive evaluation of Eqs. 6.8 to 6.10, which have the analytical solutions

$$\psi_j^D\left(\boldsymbol{r},t+\Delta t\right) = \exp\left(\hat{D}\Delta t\right)\psi_j\left(\boldsymbol{r},t\right) \tag{6.11}$$

$$\psi_j^N\left(\boldsymbol{r},t+\Delta t\right) = \exp\left(\hat{N}\Delta t\right)\psi_j\left(\boldsymbol{r},t\right) \tag{6.12}$$

$$\psi_j^C\left(\boldsymbol{r},t+\Delta t\right) = \hat{C}\Delta t + \psi_j\left(\boldsymbol{r},t\right) \tag{6.13}$$

Since the nonlinear operator $\hat{N}$ is just a scalar, the two components $\psi_j^N\left(t+\Delta t\right)$ and $\psi_j^C\left(t+\Delta t\right)$ can be easily obtained in real space. In contrast, this does not hold for the dispersion operator $\hat{D}$ due to the gradient terms. A possible approach is to transform the problem to Fourier space, which reads

$$\tilde{\psi}_j\left(\boldsymbol{k},t\right)=\mathcal{F}\left[\psi_j\left(\boldsymbol{r},t\right)\right]\,, \tag{6.14}$$

and to calculate the analytic solution of $\tilde{\psi}_j^D\left(\boldsymbol{k},t+\Delta t\right)$. Here the gradient operators become scalars, i.e., $\nabla\rightarrow i\boldsymbol{k}$, which allows for a similar evaluation of the dispersion step. Subsequently, the real space wave function $\psi_j^D\left(\boldsymbol{r},t+\Delta t\right)$ is obtained via inverse Fourier transformation

$$\psi_j^D\left(\boldsymbol{r},t+\Delta t\right)=\mathcal{F}^{-1}\left[\exp\left(\hat{D}\left(i\boldsymbol{k}\right)\Delta t\right)\mathcal{F}\left[\psi_j\left(\boldsymbol{r},t\right)\right]\right]\,. \tag{6.15}$$

Thus, solving the equations of motion for the three complex order parameters (i.e., Eq. 6.5) demands consecutive evaluation of Eqs. 6.11 to 6.13, in which the solution of the previous step serves as input for the following one. During this procedure, each step is computed for $j=1,2,3$ simultaneously.

The numerical implementation of these equations of motion using the SOFM vividly illustrates that the time-dependent Ginzburg-Landau approach for the evolution of $\psi_j\left(\boldsymbol{r},t\right)$ is analogous to an overdamped oscillator model, where all spectral components of ψ_j different from $\boldsymbol{q}_j$ simply decay exponentially over time.

Details of the numerical implementation

The IC CDW dynamics is modeled on a two-dimensional domain of ~100 nm in width, corresponding to a spatial grid composed of 2^{10} support points in both directions. The necessity to calculate the 2D Fourier transform $\mathcal{F}\left[\psi_j\left(\boldsymbol{r},t\right)\right]$ during each propagation step demands use of periodic boundary conditions. Thus, the size of the simulation domain in x and y direction has to be an integer multiple of λ_{IC} and $2\lambda_{IC}/\sqrt{(3)}$, respectively.

Since a particular interest of this numerical simulation is to study the transient disorder in the IC CDW phase directly following the NC-IC phase transition, the charge modulation of the NC phase is chosen as the initial condition. Therefore, the three complex order parameters ψ_j^{NC} are calculated as described by Nakanishi and Shiba in Ref. [121], which is based on including higher harmonics of the wavevectors $\boldsymbol{q}_j^*=\boldsymbol{q}_j^{IC}-\boldsymbol{q}_j^{C}$, where $\boldsymbol{q}_j^{IC}$ and $\boldsymbol{q}_j^{C}$ denote the equilibrium wavevectors of the IC and C phase, respectively. These higher

harmonics induce a smoothly varying modulation of ψ_j^C, which is far from sinusoidal, thus, giving ψ_j^{NC} its domain-like structure (cf. Fig. 6.1a).
However, since $\boldsymbol{q}_j^{IC}$ and $\boldsymbol{q}_j^{C}$ have different lengths and are rotated by an angle of 13.9° relative to each other, it is impossible to cover the whole simulation domain with the NC CDW phase while fulfilling periodic boundary conditions. For this reason, ψ_j^{NC} is modified by a windowing function, which smoothly sets the charge modulation amplitude to zero at the edges of the simulation domain. The decay of the windowing function has a FWHM of 5 nm, and it uniformly disappears as the IC charge-density modulation approaches the periodic simulation domain boundaries. Furthermore, a finite amount of Gaussian amplitude and phase noise is applied to ψ_j^{NC} in order to account for the disorder introduced by an optical pump pulse. This noise features a correlation length of ~2.4 nm, as well as peak-to-peak values of 50 % and π for the amplitude and phase, respectively[1].

The coefficients a, b, c and d of Eq. 6.5 used for this specific numerical simulation are based on the experimental findings presented in Chap. 5 and have the values $a = 6/\left|\boldsymbol{q}_j^{IC}\right|^4 \text{ps}^{-1}$, $b = a/2$, $c = 1 \text{ ps}^{-1}$ and $d = -0.25 \text{ ps}^{-1}$. For instance, the ratio $a/b = 2$ represents the elongation of the ICP diffraction peaks in the azimuthal direction, as also observed experimentally. The amplitude g of the IC phase charge-density modulation is determined via $g = J_1\left(\boldsymbol{q}_j^{IC} \cdot \boldsymbol{A}\right) \approx 0.051$ [89], where J_1 denotes the first-order Bessel function and $\boldsymbol{A}$ is the atomic displacement amplitude.

6.3 IC CDW dynamics and topological defect annihilation

After setting the initial simulation conditions to the NCP charge-density modulation superimposed by amplitude and phase noise, the system of the three coupled PDEs freely propagates towards the minimum of the free-energy functional F_{IC}. The evolution of this system towards an undistorted CDW with wavevectors $\boldsymbol{q}_j^{IC}$ can be seen as series of several consecutive stages, which are displayed in Fig. 6.1 at four exemplary time steps. The top panels of Fig. 6.1 represent the real-space charge-density modulation $\alpha(\boldsymbol{r})$ composed of the three complex order parameters ψ_j $(j = 1, 2, 3)$, whereas the bottom left insets show the phase $\varphi_1 = \arg(\psi_1)$, which has been corrected for the oscillatory components caused by $\boldsymbol{q}_1^{IC}$. This way, phase singularities of ψ_1 become readily discernible.

---

[1] To preserve the correct phase relation between the three complex components ψ_j^{NC}, is it essential to make sure that the phase noise applied to each ψ_j^{NC} adds up to zero at every grid point $\boldsymbol{r}$.

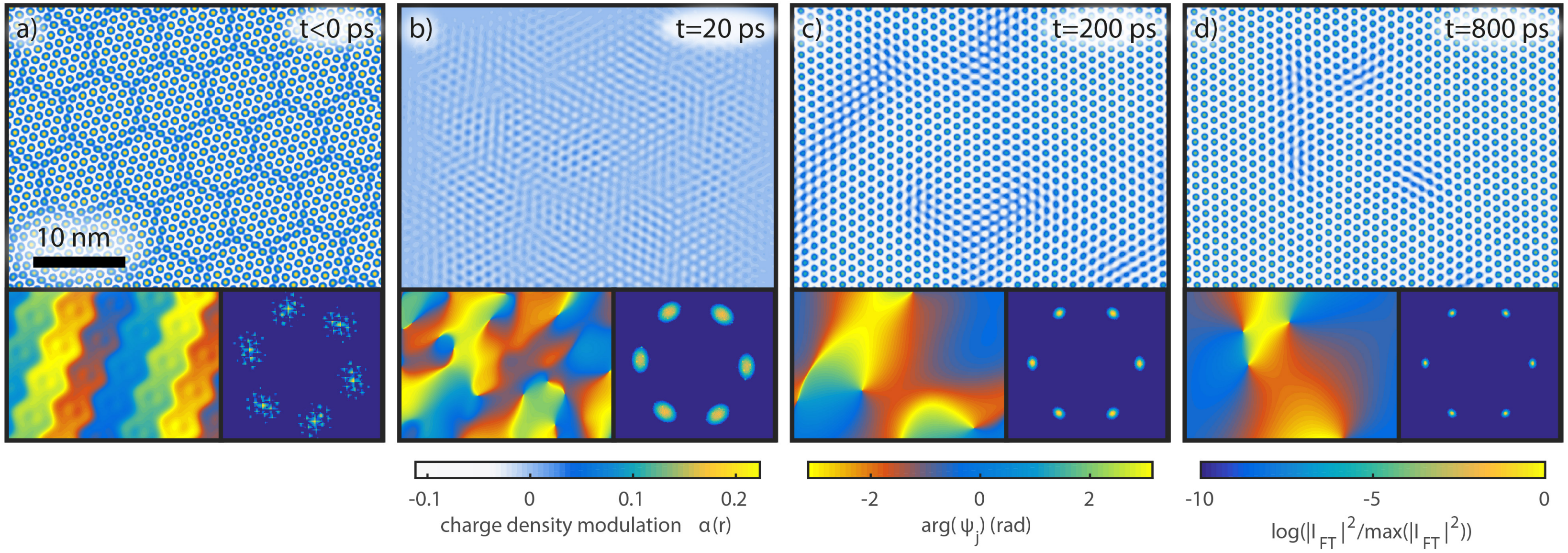

Figure 6.1: Numeric modeling of CDW dynamics associated with the NC-IC phase transition and the subsequent IC phase ordering. **a**, The initial condition for the numeric simulation is given by the NCP charge-density modulation. The windowing function of ψ_j^{NC} is not depicted, as the shown charge-density modulation just represents a subset of the simulation. **b** to **d**, Evolution of the IC CDW phase during its propagation to the minimum defined by F_{IC}. The real space charge modulation $\alpha\left(\boldsymbol{r}\right)$ is shown in the top panels, whereas the bottom left insets display the phase $\varphi_1 = \arg\left(\psi_1\right)$ corrected for oscillations caused by $\boldsymbol{q}_1^{IC}$. As can be seen in panels **b** to **d**, shortly after the phase transition, the exemplary order parameter ψ_1 is subject to a pronounced transient disorder, which manifests in numerous phase singularities of φ_1. Furthermore, the bottom right insets display a normalized representation of the squared Fourier magnitudes of $\alpha\left(\boldsymbol{r}\right)$, which are derived by averaging over ten independent simulation runs using randomly distorted starting conditions ψ_j^{NC}. In analogy to the ULEED diffraction signal, panels **b** to **d** show drastically broadened peaks, which subsequently get narrower over simulation time. The three color scales (f.l.t.r.) correspond to the IC CDW charge-density modulation $\alpha\left(\boldsymbol{r}\right)$, to the phase φ_1 of the first complex order parameter ψ_1 and to the squared Fourier magnitudes of $\alpha\left(\boldsymbol{r}\right)$, respectively.

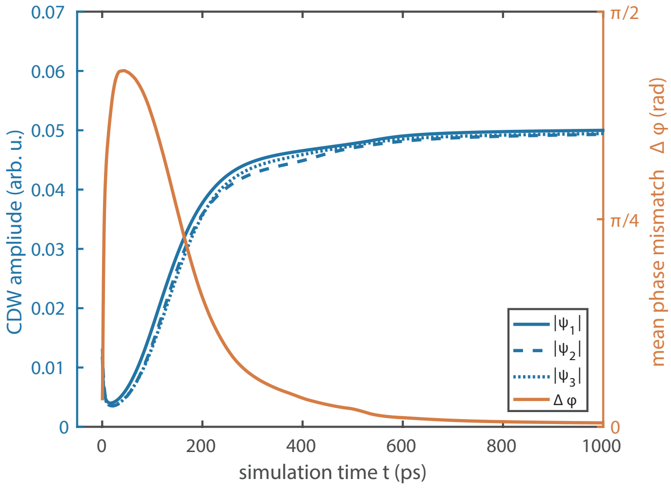

Figure 6.2: Temporal evolution of the spatially averaged amplitudes of the three complex order parameters ψ_j^{IC} and the mean phase mismatch $\Delta\varphi$ between the respective components.

Moreover, to analyze the temporal behavior of the correlation length ξ_{IC}, the normalized squared Fourier magnitudes of $\alpha\left(\boldsymbol{r}\right)$ are also calculated. After averaging over ten independent evolutions, these are displayed in the bottom right insets of Fig. 6.1.

Within the first stage of the IC CDW dynamics, covering a few tens of ps after time zero, the charge-density modulation amplitude rapidly decreases and becomes particularly low at sites of the former NCP discommensurations. Such a strongly suppressed modulation amplitude promotes the appearance of numerous pitchfork dislocations in each of the the complex order parameters ψ_j, which simultaneously leads to local dephasing of the individual components ψ_j relative to each other. Both effects can be seen in Fig. 6.1b, as well as in Fig. 6.2. Here, the latter shows the amplitudes of the individual components $|\psi_j|$ together with a spatially averaged phase mismatch $\Delta\varphi\left(t\right)$ between the three complex order parameters $\psi_j\left(\boldsymbol{r},t\right)$ that is calculated via

$$\Delta\varphi\left(t\right)=\left\langle\left|\sum_j \arg\left(\psi_j\left(\boldsymbol{r},t\right)\right) \bmod 2\pi\right|\right\rangle . \qquad (6.16)$$

Subsequently, on the timescale of a few hundred ps, the independent pitchfork dislocations begin to merge and cause the formation of larger regions of ψ_j that are defect free, but still elastically deformed. In this context, it is important to note that the pitchfork dislocations are mobile inside each ψ_j and propagate via glide and climb motions. Along the way, they attract or repel each other depending on their winding number or Burgers vector, respectively, as described in Sec. 2.4.3. At this stage, the defect free regions are successively characterized by a growing CDW amplitude and a correct phase relationship between the complex contributions ψ_j.

As the total number pitchfork dislocations deceases over time, the interaction of dislocations located in different ψ_j and coupled via the phasing term of F_{IC}, turns out increasingly important. More precisely, two dislocations based in ψ_j and ψ_k will approach each to reduce the phasing energy. This way, two pitchfork dislocations form a topological defect of the hexagonal CDW lattice, as described in Sec. 2.4.3.

For this reason, topological defects of the triple CDW likewise attract or repel each other, depending on the winding numbers or Burgers vectors of their constituents. The latter also determine whether two topological defects of the triple CDW can completely annihilate or, alternatively, recombine to a new one if only two of the four constituent pitchfork dislocations have a counterpart inside the other topological defect.

For a more detailed analysis of the influence the topological defects have on the CDW correlation length ξ_{IC}, two approaches are pursued. The first is to count the total number $N_j(t)$ of pitchfork dislocations inside each ψ_j and assume a homogeneous defect distribution. Then, the correlation length ξ_{IC} is determined from the topological defect density

$$\varrho_D(t) = \frac{1}{2A}\sum_j N_j(t) \quad \text{via} \quad \xi_{IC}(t) = 1/\sqrt{\varrho_D(t)}, \tag{6.17}$$

where A is the area of the simulation domain. The complete procedure to numerically identify and characterize the dislocation defects in terms of their Burgers vectors is described in Sec. A.5 of the appendix.

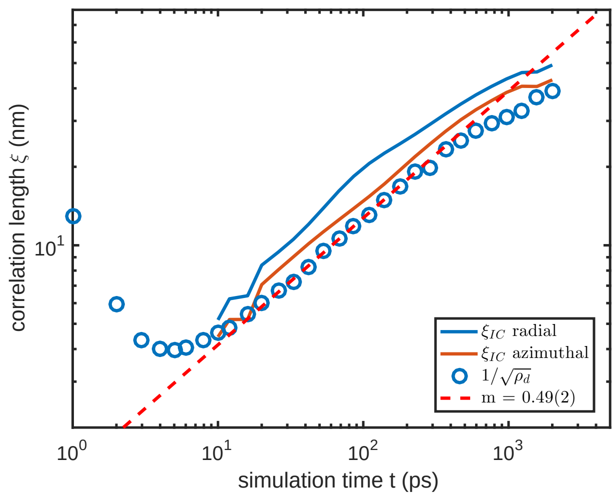

Figure 6.3: Double logarithmic plot of the correlation length ξ_{IC} versus simulation time t. The correlation length of the modeled IC CDW is obtained from both the area density ρ_d of the topological defects (blue circles) and the inverse width of the squared Fourier magnitudes in radial and azimuthal directions (blue and red lines). A fit to the data for $25\,\mathrm{ps} \le t \le 350\,\mathrm{ps}$ (red dashed line) yields a power-law behavior $\xi_{IC}(t) \propto t^m$ with an exponent of $m = 0.49 \pm 0.02$.

Simultaneously, for each time step, the correlation length $\xi_{IC}(t)$ of $\alpha(\boldsymbol{r})$ is obtained by calculating and analyzing the squared Fourier magnitudes $I(\boldsymbol{r}, t) = |\mathcal{F}[\alpha(\boldsymbol{r}, t)]|^2$ of the IC charge-density modulation. Analogous to the investigation of the experimentally yielded diffraction patterns, the radial and azimuthal widths w (FWHM) of the Fourier components are determined by two-dimensional fitting. Subsequently, the correlation length $\xi_{IC}(t)$ is obtained via $\xi_{IC}(t) = 2\pi/w(t)$.

To examine the temporal evolution of $\xi_{IC}(t)$ inside the simulated IC charge-density modulation, Fig. 6.3 shows a double logarithmic plot of the correlation lengths ξ_{IC} obtained from both approaches, i.e., $\rho_d(t)$ and the time-dependent Fourier magnitudes. It is readily seen that, directly after NC-IC CDW phase transition at time zero, ξ_{IC} is strongly suppressed by a large number of topological defects. This can be explained by considering the temporal evolution of the charge-density modulation. As the system tries to locally map the NC charge-density modulation to the one of the ICP, the overall charge modulation is subject to a significant amount of elastic strain, which is reduced via unbinding pairs of topological defects.

Subsequently, while these defects annihilate over time, the correlation length again increases following a power-law behavior

$$\xi_{IC}(t) \propto t^m \,. \tag{6.18}$$

The exponent m is determined via a fit to the data from the time-dependent defect density $\rho_d(t)$ in the range $t = 25$ ps to 350 ps. This yields $m = 0.49 \pm 0.02$, which indicates a very similar behavior as experimentally observed for the IC CDW diffraction peak widths. Equally, the power-law growth of the IC CDW correlation length can be verified by analyzing the squared Fourier magnitudes of the simulated IC charge modulation displayed as blue and red line in Fig. 6.3.

For simulation times $t \gtrsim 400$ ps, the growth of correlation length is decelerating. This effect may be explained by a reduced mobility of the partial (pitchfork) dislocations once two of them each are tied together forming a topological defect of the triple CDW.

Chapter 7

Relaxation dynamics of 1T-TaS$_2$

The preceding chapters focused on the structural dynamics associated with the transition from the room-temperature NC to the high-temperature IC phase in 1T-TaS$_2$. However, it is equally interesting to study the sample's relaxation from the ICP to the pristine NC ground state, as this process allows for characterizing the emergence of a well-ordered CDW that is widely registered to the atomic lattice.

Hence, the following chapter presents two additional experimental approaches that extend the capabilities of ULEED and simultaneously serve as a starting point for further studies of 1T-TaS$_2$ and similar sample systems.

7.1 Time-resolved recovery of the NC CDW phase

Typically, pump-probe experiments obtain their high temporal precision from harnessing the enormous speed of light and mechanically varying the optical path length, e.g., by very accurate linear translation stages. However, the available time delays are limited to a few ns depending on the finite length of the respective translation stage. For the ULEED setup presented in Sec. 4.4, the 30 cm translation stage defines a maximum time delay of $\Delta t = 2$ ns[1].

Considering the time-dependent diffraction peak signals presented in Sec. 5.1, the ICP intensity is still subject to a slight increase at $\Delta t = 1$ ns, and the atomic lattice Bragg peaks just indicate a subtle reduction of the sample temperature within this time window. Therefore, it is impossible to analyze the relaxation of the 1T-TaS$_2$ surface within the accessible 2 ns. Hence, to cover the full interval of 8 µs between two subsequent pump

---

[1] In principle, extension of the maximum delay time is possible by elongating the optical path length on the stage using additional roundtrips, but this also multiplies the impact of the imprecision the linear stage has on the delay-dependent beam pointing.

pulses of a setup operated at 125 kHz, a different method to generate time-delayed optical pump pulses is necessary.

7.1.1 Experimental setup

An alternative approach to delaying laser pulses using mechanical translation stages is the electronic control of the emission time. This requires a second pulsed laser system, which can be actively switched by an external trigger signal.

In the present configuration of ULEED used to study the recovery of the NC CDW phase, the fs laser-system for electron pulse generation is supplemented by an actively switched diode-pumped solid state (DPSS) laser for sample excitation. This laser systems consists of a RegA 9000 regenerative amplifier seeded by a Mantis oscillator, both pumped by a Verdi V18 CW laser. Similar to the setup presented in Sec. 4.4, its resulting 800 nm pulses (~5 µJ pulse energy, 90 fs duration) are frequency doubled and focused onto the apex of the nanometric tungsten photocathode inside the mm-sized electron source.

In contrast to the setup described in Sec. 4.4, the sample excitation is realized by an electro-optically Q-switched Helios DPSS laser. It operates at a fixed repetition rate of 125 kHz and emits 0.85 ns pulses at a central wavelength of 532 nm and 30 µJ pulse energy. An electronic delay generator (DG535, SRS) provides for the exact timing of the pump pulses. Using the fs laser system as a reference signal, the delay generator allows for arbitrary time delays in the 8 µs interval between two successive probe pulses. Thus, the temporal resolution of this setup is determined by the timing precision of both the DPSS laser and the delay generator, which leads to an overall jitter of approximately 3 ns. A motorized variable attenuator in front of the vacuum chamber facilitates a large number of fully automated measurements at different pump fluences F. Figure 7.1 displays a schematic representation of the complete setup.

7.1.2 Results and discussion

Using the present configuration of the ULEED setup, a set of time-resolved diffraction measurements has been conducted at pump fluences ranging from $F = 1.2$ to $3.0\ \mathrm{mJ/cm^2}$ and for time delays spanning the whole interval between two consecutive probe pulses. Subsequently, the integrated intensities of the NC and IC CDW diffraction peaks, the atomic lattice Bragg peaks and the background are analyzed for each time delay Δt and depicted in Fig. 7.2.

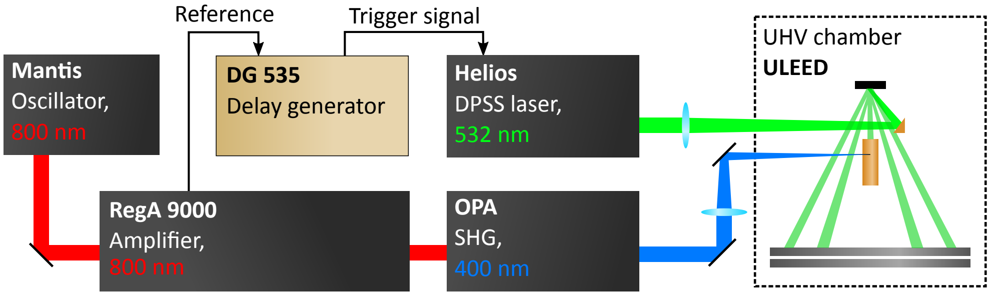

Figure 7.1: The ULEED setup used to analyze the relaxation dynamics of NC CDW phase at the surface of 1T-TaS_2. In order to generate pump-probe time delays ranging from several ns to µs, the sample is excited by an additional diode-pumped solid state laser, which is actively triggered by an electronic delay generator.

Considering the signals of the NC and IC phase diffraction peaks, a prominent feature is the pronounced fluence dependence of the CDW relaxation to the NC ground state. After excitation at time-zero, it takes up to several hundreds of ns for both CDW phases to (partially) recover to their initial value. Fitting the data with the convolution of a Gaussian excitation pulse and an exponential decay leads to recovery time constants τ ranging from 20 to 50 ns for $F < 1.5$ mJ/cm^2 and 700 to 1050 ns for $F \geq 2.4$ mJ/cm^2 for the NC and IC phase, respectively. These time constants correspond to an intensity decay to 1/e and are shown in Fig. 7.2e. Moreover, τ is characterized by a notable threshold behavior around $F = 2$ mJ/cm^2.

In stark contrast, the integrated intensities of the atomic lattice Bragg peaks and background exhibit a distinctly faster recovery. As already surmised from the data recorded with higher temporal resolution in Sec. 5.1, the suppression and relatively quick relaxation of the atomic lattice Bragg peaks and the background corresponds to a thermal equilibration of the sample on the ns timescale. Averaging the relaxation constants of the Bragg peak intensity over all pump fluences yields $\tau_{BP} = 14.6 \pm 1.3$ ns, which is almost two orders of magnitude faster than the recovery of the NC and IC phases at fluences above 2.4 mJ/cm^2.

Furthermore, Figures 7.2a and b indicate that, for high pump fluences, parts of the excited surface area remain in the IC phase even for time delays $\Delta t < 0$ ns. This observation can be understood by interpreting the present fluence-dependent measurements as a series of pump-probe experiments conducted at successively elevated base temperatures T_B, which may also explain the very long recovery time constants for the CDW at high pump fluence.

Hence, the fluence-dependent measurements can be divided into three regimes:

- Initially, for pump fluences $F < 1.3$ mJ/cm^2, the NCP diffraction peaks are only affected by a thermal suppression, which relaxes on the same timescale as required for diffusive cooling. Simultaneously, a cumulative temperature increase leads to an equilibrium NCP intensity decreased by up to 8 % compared to the intensity of the pristine NCP diffraction peaks.

- Following excitation in the range $1.3\,\mathrm{mJ/cm^2} \leq F \leq 2.1\,\mathrm{mJ/cm^2}$, successively larger amounts of the sample surface are driven to the IC phase, as can be seen from the maximum of the ICP intensity in Fig. 7.2b. Still, these regions completely recover to the NC ground state within less than 200 ns, which is before the arrival of the next pump pulse (cf. Fig. 7.2e).

- Finally, for excitation fluences of $F \geq 2.2$ mJ/cm^2, the IC CDW only partially recovers to NCP ground state between two consecutive pump pulses, and the NCP and ICP relaxation constants τ exhibit a significant increase.

This complex behavior has several reasons and can be explained by the following physical picture: Due to a slightly inhomogeneous excitation profile, the lateral size of the transformed sample area grows with increasing pump fluences, thus, giving rise to the successively increasing maximum ICP intensities.

Furthermore, the sample surface is subject to a fluence-dependent base temperature T_B, which locally reaches $T_{IC} = 353$ K at $F = 2$ mJ/cm^2. This causes a static CDW phase transition, which manifests in ICP diffraction peaks even present at $\Delta t < 0$ ns.

The elevated base temperature has a direct influence on the CDW relaxation time constants τ. Approaching T_{IC} at the surface, the temperature gradients between the excited area and the underlying bath gradually decrease and cause a slowed diffusive cooling. Moreover, at a base temperature close to T_{IC}, the CDW phase transition is driven to significantly deeper layers of the sample while the optically injected heat diffuses into the bulk. As a result, it takes drastically longer for the NC CDW to grow back to the sample surface.

In summary, resulting from an elevated base temperature T_B at a laser repetition rate of $f = 125$ kHz, the recovery time constants τ of the NC and IC CDW diffraction signals are ranging from tens of ns to a few µs. This effect is attributed to a decelerated diffusive cooling in combination with a diverging NC-to-IC transformation depth.

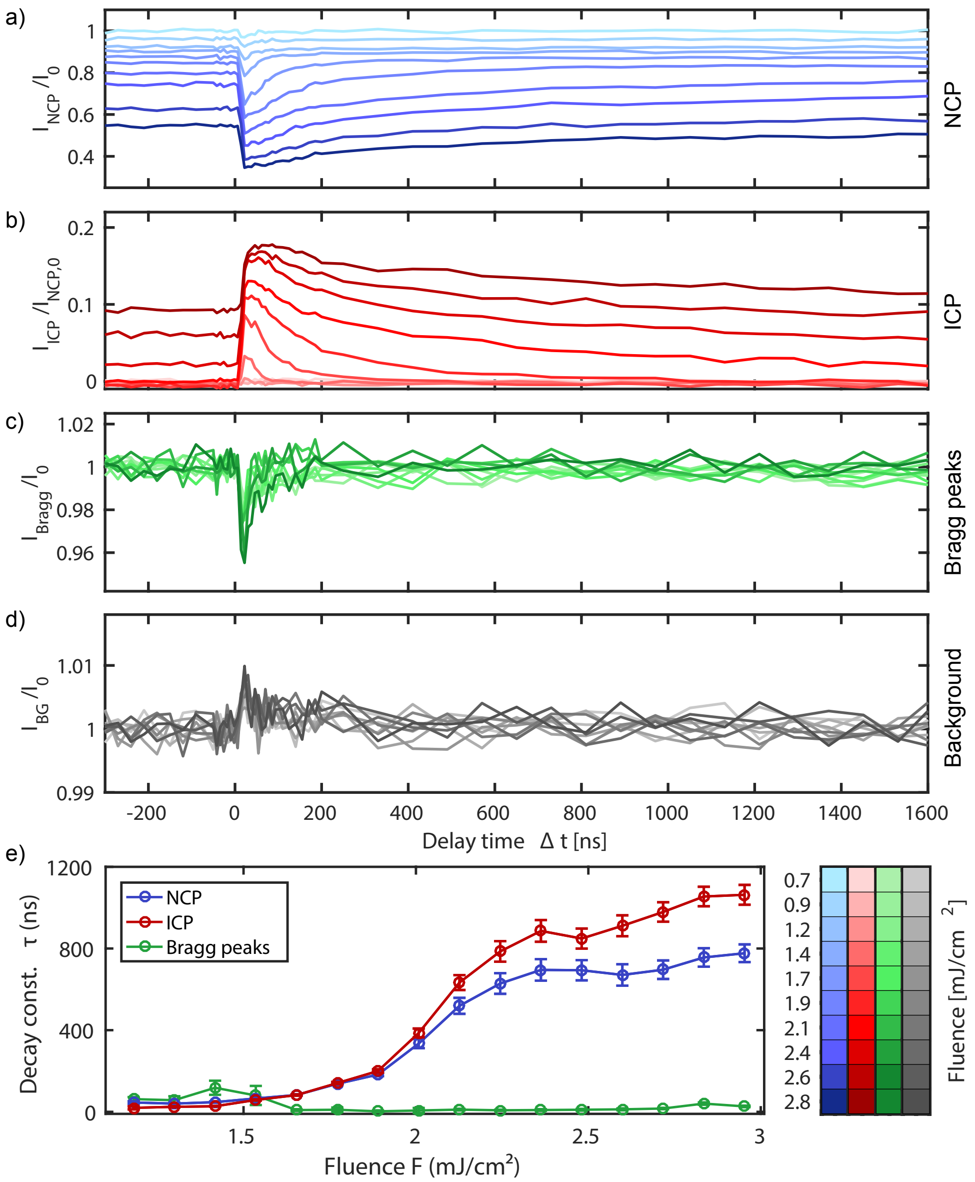

Figure 7.2: Fluence-dependent measurement of the CDW recovery to the NCP ground state. **a** - **d**, Delay-dependent integrated intensities of the NCP and ICP satellite spots, the atomic lattice diffraction peaks, as well as the diffuse background, respectively. **e**, Relaxation time constants τ obtained from **a** to **c** by fitting with the convolution of a Gaussian excitation pulse and an exponential decay. The relaxation to the original NC CDW ground state exhibits a pronounced fluence dependence indicated by time constants τ spanning almost two orders of magnitude.

7.2 Probabilistic switching of the chiral NC CDW orientation

For the C and the NC phase of 1T-TaS$_2$, the CDW superstructure unit cell is rotated by 13.9° relative to the atomic lattice due to the (3×1)-commensurability condition (cf. Sec. 3.1). As there is no preferred rotation direction, generally, both superstructure orientations are equally possible. Depending on their orientation, Wilson *et al.* coined the terminology of α and β-type domains for counterclockwise and clockwise rotated CDW superstructures, respectively (see Fig. 7.3a) [76]. Since these regions only differ in their orientation, with otherwise identical properties, they are also referred to as twin domains or mirror domains [76]. Such chiral CDWs are not just restricted to 1T-TaS$_2$, but also have been observed in 1T-TiSe$_2$ via STM [187] or in 1T-TaSe$_2$ and 4Hb-TaS$_2$ by TEM measurements [76].

To identify these two types of CDW order at the surface of 1T-TaS$_2$, ULEED constitutes an ideal technique, since it is highly sensitive to the lattice geometry and simultaneously features a very confined electron beam. The latter allows one to identify single domains of ~100 µm in diameter, whereas a conventional LEED system would just yield the spatially averaged surface geometry. Due to the high quality of the 1T-TaS$_2$ samples at hand, most of the investigated crystals exhibit just one CDW orientation at their surface, typically being 1-2 mm^2 in size. In comparison, samples intrinsically showing both α and β-type NCP domains (Fig. 7.3b) are relatively rare.

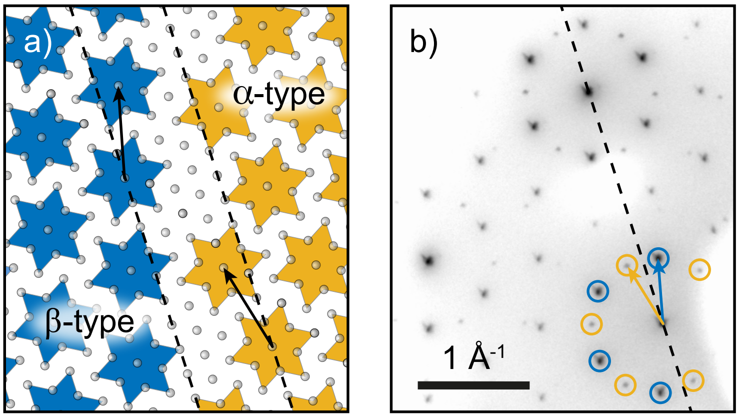

Figure 7.3: Twin domains present in the NC and C phase. **a**, The domains of charge accumulations are rotated by 13.9° either counterclockwise or clockwise relative to the atomic lattice and are referred to as α-type or β-type, respectively [76]. **b**, ULEED diffraction pattern of the C phase simultaneously exhibiting α and β-type domains, which are marked with yellow and blue circles, respectively. The diffraction pattern is recorded at $T = 180$ K, $E_{kin} = 100\,\text{eV}$ and 60 s integration time.

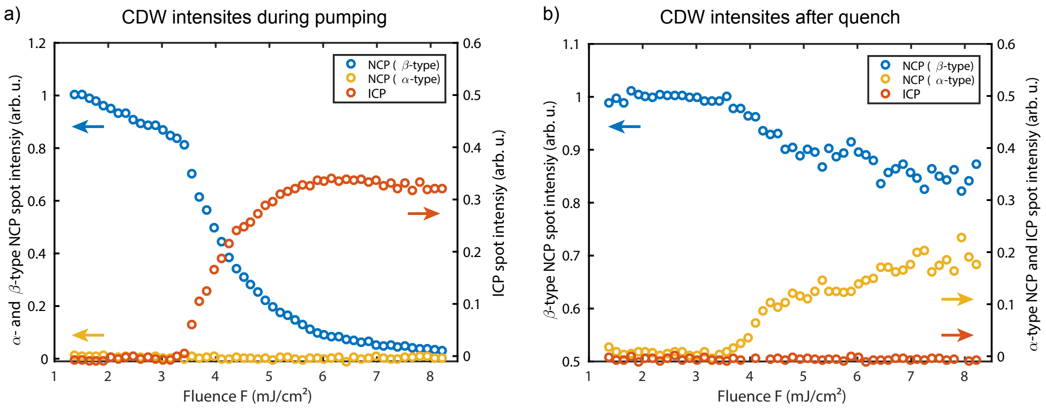

Figure 7.4: Quenching the IC CDW order induces twin domains of the symmetry equivalent α and β-type NC phases. **a**, Intensities of the CDW satellite diffraction peaks during optical excitation as a function of incident pump fluence F. **b**, CDW spot intensities after quenching the IC phase. Above fluences of $F \gtrsim 4$ mJ/cm^2, a fraction of the pristine β-type NC CDW phase is converted to the α-type, while the sum of both intensities remains constant. After each excitation-quench-cycle the sample is annealed at a moderate fluence of $F = 3.4$ mJ/cm^2 for 20 s, which completely restores the β-type NCP in the probed volume.

However, it is possible to induce the simultaneous growth of both α and β-domains in the NC CDW phase via quenching from the high-temperature IC phase. To this end, using the experimental setup shown in Fig. 7.1, a sample exclusively exhibiting the β-type NCP is continuously driven to the ICP using intense laser irradiation for 20 s. Subsequently blocking the pump beam within 2 ms by an optical shutter leads to a rapid temperature decrease. As a result, for pump fluences $F \gtrsim 4$ mJ/cm^2, several domains of the formerly absent α-type NC phase are created in the probed surface area, as can be seen in Fig. 7.4b. Since the growth of both chiral NC phases occurs probabilistic, the surface area of the newly created α-type NCP is subject to significant variations. The overall intensity diffracted into the NCP satellite spots, however, remains conserved.

For a comprehensive overview, Figure 7.4a shows the CDW diffraction peak intensities during optical heating, which are recorded at negative time delays (i.e., the electron pulse arrives before the optical pump pulse). Here, particular attention should be paid to the threshold fluences for the rise of the IC phase during heating (Fig. 7.4a) and the appearance of α-type NCP domains upon cooling (Fig. 7.4b). Comparison of both threshold fluences leads to the conclusion that a significant amount of the sample needs to be continuously driven to the IC phase to effectively create NCP twin domains by quenching.

To repeatedly study the NCP growth from the IC phase, after each quench the initial situation of the sample fully exhibiting the β-type NC phase has to be restored. This is achieved by optical annealing at moderate laser intensities. Thus, every excitation-quench-cycle is completed by a final annealing step at $F = 3.4$ mJ/cm^2 for another 20 s. Fluence-dependent scans indicate a minimum fluence of $F \approx 2.4$ mJ/cm^2 necessary to completely restore the original NCP orientation. Hence, the recovery of the β-type NC phase is promoted by a temporary excitation to the IC phase, which completely relaxes to the NCP within one excitation period.

Real-space analysis of chiral NCP domains

Since ULEED is limited to a reciprocal-space investigation of the surface lattice structure, it is highly desirable to also study the previously observed growth of both α and β-type NCP domains in real space. Therefore, thin 1T-TaS$_2$ flakes are analyzed in a TEM, which allows for in-situ single-shot laser excitation of the sample and, hence, is ideally suited to address this task. A further advantage of transmission electron microscopy arises from its simultaneous access to both the reciprocal and real space structure of a sample. This opens up the possibility of dark-field imaging. Here, an aperture is placed in the diffraction plane to exclusively capture electrons that are diffracted into a particular Bragg peak and to reject all other transmitted electrons. In the following, the selected electrons form a real space image in which only sample areas with a particular crystallographic orientation generate contrast. Hence, by choosing individual NCP satellite spots for dark-field imaging, the real space distribution of both α and β-type NCP domains can be visualized (cf. Fig. 7.5a).

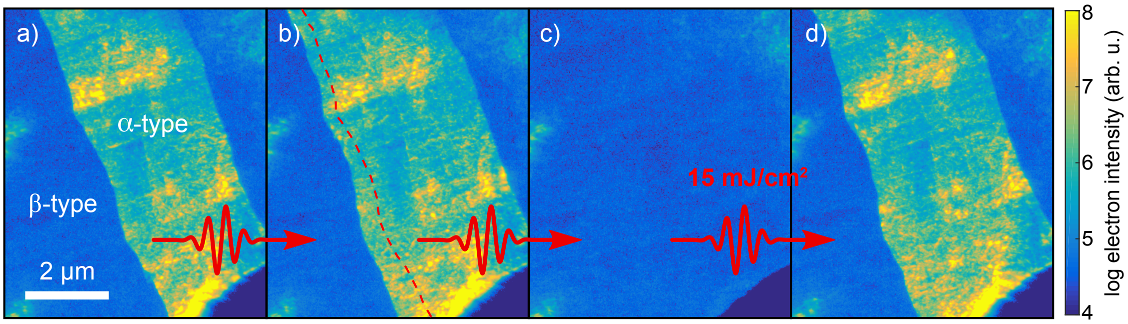

Figure 7.5: Structural changes of the NC phase induced by a series of single-shot laser pulses. Panels **a** to **d** show TEM micrographs of a thin 1T-TaS$_2$ sample at room temperature. The specific shape of domains exhibiting different orientations (α and β-type) is studied by means of dark-field imaging. Triggered by intense single-pulse laser excitation (15 mJ/cm^2, 800 nm) the domains alter their shape or even disappear.

To verify the probabilistic nature of the NCP domain growth, a fixed sample area is optically excited and imaged in a series of TEM micrographs. After recording each frame, a single fs-laser pulse ($\lambda_c = 800$ nm) pumps the region of interest at a fluence of $F = 15$ mJ/cm^2. As a result of the intense laser irradiation, the considered NCP domains alter their shape in subsequent images (Fig. 7.5b) or even disappear completely (panel c). Due to the excitation scheme employing individual laser pulses, it is not possible to reproducibly switch the sample back to the overall β-type NC phase.

Furthermore, considering the shape of several α-type NCP domains, their emergence seems to be seeded at the supporting Cu-TEM mesh, which can be seen in the lower right corners of Figs. 7.5a-d. This supports the assumption that the cooling rate plays a decisive role for the occurrence of NCP twin domains, since these areas feature a significantly better thermal coupling.

Chapter 8

Discussion

In the previous Chapters, the successful implementation of ULEED in a backscattering geometry has been demonstrated by mapping a CDW structural phase transition and the following phase-ordering kinetics. As a central result, the observed coarsening of the ICP correlation length ξ_{IC} subsequent to the optically induced NC-IC phase transition is attributed to a variable density of topological defects present in the CDW lattice. To corroborate this conclusion, a numerical modeling of the equilibrating IC CDW has been conducted.

In the following section, the experimental findings will be discussed in the context of the numerical simulation. Additionally, the results of the NCP relaxation dynamics accessible via the two alternative excitation schemes presented in Chap. 7 are put in relation to the foregoing measurements.

ICP phase-ordering kinetics

By analyzing the ICP diffraction spot profiles as a function of delay time Δt for the four highest pump fluences F (cf. Fig. 5.6), two major statements can be made about the temporal evolution of the CDW correlation length $\xi_{IC}(\Delta t)$:

- Directly after the NC-IC phase transition, the correlation length ξ_{IC} and, hence, the density of topological defects is independent of the applied pump fluence F.
- The subsequent CDW phase-ordering process obeys the power law $\xi_{IC}(\Delta t) \propto \Delta t^{1/2}$.

The first observation indicates that, ensuing the NC-IC phase transition, the density of topological defects is predominantly determined by the charge-density configuration of the room-temperature NC phase. As there is no continuous deformation that globally maps the patched texture of the NC state to the IC CDW, the situation in the newly created IC phase is that of a quench. Since the ICP charge modulation simultaneously emerges locally all over the excited surface area, regions separated by causality can exhibit an arbitrary phase mismatch. When these regions meet, dislocations of the CDW lattice are inevitable. This behavior is also known as the Kibble-Zurek mechanism, which describes the formation of topological defects (e.g., domain walls, lines, point defects) by quenching a system through a second-order phase transition [95, 188, 189].

In the cosmological context of Kibble, "separation by causality" refers to the speed of light [188], whereas for condensed matter systems, as proposed by Zurek, information spreads at the speed of sound in the respective material [95]. However, one should note that, compared to the Kibble-Zurek mechanism, the NC-IC phase transition is first-order [121, 124], and, more importantly, the density of topological defects should not depend on the quench rate.

Similar to the experimental observations, the numerical simulation indicates a massive generation of topological defects shortly after quenching the IC CDW from an excited, but defect-free NC state. As can be seen in Fig. 8.1, the ICP correlation length $\xi_{IC}\left(\Delta t\right)$ deduced from the dislocation density $\varrho_D\left(\Delta t\right)$ rapidly drops at early simulation times. Consequently, the subsequent phase-ordering kinetics of the IC CDW are mainly driven by annihilation and recombination of topological defects.

The microscopic mechanism for the observed coarsening of the IC CDW correlation length ξ_{IC} after the NC-IC phase transition is also addressed in two further works utilizing time-resolved x-ray and electron diffraction at the bulk of 1T-TaS$_2$ [148, 150]. Although Haupt *et al.* find some indication for an ICP diffraction peak narrowing, they are lacking a quantitative analysis of the coarsening process and just attribute the local origin of the IC phase to the NCP discommensurations [148].

In comparison, in a time-resolved x-ray diffraction experiment, Laulhé *et al.* observe a growth of the correlation length ξ_{IC} following the same power-law behavior $\xi_{IC} \propto \Delta t^{1/2}$ [150]. However, they associate the growth of the ICP correlation length ξ_{IC} to the coarsening of CDW domains separated by well-defined domain walls and neglect the ability of the "free floating" ICP to easily slide across the atomic lattice.

For numerous coarsening phenomena following a quench, the characteristic length scale L of the system (e.g., the correlation length or average domain size) obeys a power-law scaling, i.e., $L\left(t\right) \propto t^{\nu}$, which is also referred to as *dynamic scaling* [190].

In this framework, the growth exponent ν turns out to be independent of the particular investigated system, but is simply determined by the system's dimensionality d, the number n of components involved to describe the order parameter, as well as the question whether the chosen order parameter is conserved or non-conserved.

For the ICP phase-ordering kinetics, both experiment and simulation lead to an exponent of $\nu \approx 1/2$, which corresponds to the dynamics of a non-conserved order parameter. Mathematically, the coarsening of a system characterized by a non-conserved order parameter is also referred to as *model A* dynamics and is described by the Allen-Cahn equation [97, 100]. For domain walls, this approach may be heuristically understood by considering their mean curvature K [100]. Then, K is proportional to the driving force F (surface tension) and therefore scales with the wall velocity v of a growing domain. If the system can be described by a single characteristic length scale $L(t)$, this leads to $v \propto \mathrm{d}L/\mathrm{d}t$ and $K \propto 1/L$, which finally yields $L(t) \propto t^{1/2}$ by integration [100]. In comparison, the dynamics of conserved order parameters are rather described by the Cahn-Hillard equation (so-called *model B*), which gives a power law of $L(t) \propto t^{1/3}$ and, for instance, explains the spinodal decomposition of alloys.

Generally, the situation of phase-ordering in an incommensurate CDW via topological defect annihilation is analogous to the coarsening of a quenched XY-model mediated by vortex-antivortex annihilation. In both cases, the considered system is two dimensional ($d = 2$) and features a two-component or complex order parameter ($n = 2$), respectively. However, compared to the defect dynamics in CDWs, vortex-antivortex annihilation in the XY-model has been investigated more thoroughly both theoretically and experimentally in a variety of sample systems, which include thin films of nematic liquid crystals, as well as colloid crystals [101, 191–195]. Here, for long evolution times, the correlation length typically grows proportional to $t^{1/2}$, or, in an alternative view, the absolute defect number N decreases as $N(t) \propto t^{-1}$ [194, 196]. On the other hand, for the special case of $d = n = 2$ and a non-conserved order parameter, the need for a logarithmic correction factor mainly affecting the early time regime has been predicted theoretically and verified by several experiments [190, 193, 197–200]. Accounting for a slower increase of the correlation length shortly after the quench, the modified power law then reads [101]

$$L(t) \propto \left(t/\log\left(t/t_0\right)\right)^{1/2} . \tag{8.1}$$

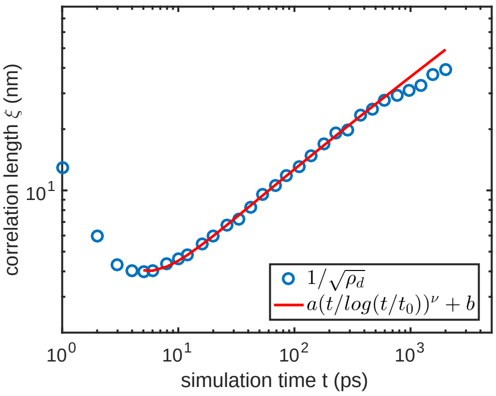

Figure 8.1: The correlation length $\xi_{IC}\,(t)$ obtained from the simulated defect density ρ_d is fitted by a power-law scaling including a log-correction. The decay of the correlation length at early simulation times can be explained by unbinding of topological defects due to massive elastic strain in the considered CDW.

However, the present experimental data cannot distinguish whether this also applies for the observed power-law growth of the correlation length in the IC CDW, since the current temporal resolution of the mm-sized electron source is limited to a few tens of ps. To resolve this question, further measurements using the µm-sized electron gun are necessary.

In comparison, the evolution of the correlation length ξ_{IC} obtained from the numerical simulation seems to be well described by Eq. 8.1. As can be seen in Fig. 8.1, for early simulation times, the correlation length is strongly suppressed by numerous topological defects appearing to reduce the elastic strain energy of the CDW, whereas for late evolution times the expected power-law growth dominates. To better describe the transition regime, a power law including the logarithmic correction factor is fitted to the simulation data. The regression yields an exponent of $\nu = 0.48 \pm 0.05$, which is slightly smaller than the previous results. The fit has been restricted to the time interval $5\,\text{ps} \leq t \leq 400\,\text{ps}$, since for later times the growth of the correlation length is significantly slowed down. Interestingly, the kink around 400 ps corresponds to the coupling of the partial dislocation defects (located in individual contributions ψ_j of the triple CDW). Consequently, this means a higher mobility of the partial dislocations as long as the phasing of the individual components ψ_j relative to each other is not completed yet.

To summarize, the numerical simulation presented within this work is well suited to qualitatively capture some important aspects of the IC CDW dynamics. For instance, it illustrates the inevitable occurrence of topological defects during equilibration, as well as their subsequent annihilation, which obeys the typical dynamic scaling behavior. However, in its current form, it is hard to extract quantitative results from the numerical model, since the values used for the coefficients of the free-energy functional F_{IC} (Eq. 6.3) are chosen in a way to correspond to both the experimentally observed elongation of the diffraction spots and the correlation length $\xi_{IC}(t)$ deduced from the diffraction patterns. A superior approach would include the free-energy functional proposed by Nakanishi and Shiba in Ref. [121]. This way, using temperature-dependent coefficients for the individual contributions to F_{IC}, the emergence of all three CDW phases should be observable by varying the system temperature. However, a numerical implementation of this approach turns out more challenging than for the presently used free-energy functional and may be the subject of future research.

Similarly, further studies are necessary to investigate the role of phasonic contributions to the ICP dynamics. Since the current numerical approach neglects all possible oscillatory responses, so far, phasons merely appear as static ($\omega \approx 0$) distortions of the CDW in the vicinity of topological defects. Moreover, the potential energy released during defect annihilation is rapidly dissipated, whereas naturally one would expect a pronounced energy transfer to phason and amplitudon excitations.

Therefore, it should be subject of further investigations to disentangle the phason contribution in both the ULEED diffraction patterns of the IC phase and the numerical simulation.

Additionally, it remains an intriguing open question whether the IC CDW phase affected by numerous dislocation defects can be considered as a transient hexatic phase. To this end, typically, one evaluates the translational and orientational correlation functions g_T and g_6 by examining the real space structure and verifies the existence of a quasi long-range orientational order and an exponentially decaying translational order, respectively. Specifically for 1T-TaS$_2$, such a hexatic phase has been created artificially via impurity doping using varying amounts of Nb [201]. Subsequently, the increasing number of dislocation defects and the successive decay of both correlation functions were simultaneously analyzed by means of STM.

Using diffractive methods, the presence of a hexatic phase is typically indicated by diffraction peaks that are strongly broadened in azimuthal direction. This is demonstrated by both x-ray scattering experiments and TEM measurements conducted at thin films of layered liquid crystals [202–205]. Here, the magnitude of the resulting azimuthal broadening depends on number of layers in the film (“stacked hexatic”) [205], as well as on the interaction of topological defects [206]. While thermally activated topological defects lead to strongly elongated diffraction peaks, as observed for smectic liquid crystals, uncorrelated topological defects correspond to an azimuthal broadening ratio of approximately 2:1 [206]. This broadening ratio corresponds well to the azimuthally elongated IC CDW spot profiles we observe in the time-resolved measurements, and it supports to the assumption of topological defects appearing due to a quench from the NC CDW phase. However further measurements and a more elaborated spot profile analysis would be necessary to validate this hypothesis.

NCP relaxation dynamics

While the main part of this work deals with the ultrafast structural changes happening on the ps timescale immediately after sample excitation, the two alternative pump-probe schemes presented in Chap. 7 provide access to the relaxation dynamics occurring within ns or even µs. Specifically, both schemes are employed to study the recovery of the pristine NC CDW phase between to successive pump pulses.
In this context, two important observations can be made:

- The recovery of the NC phase is strongly dependent on the applied optical pump fluence F, and it exhibits decay constants τ ranging from tens of ns up to a few µs. The decay constants τ rapidly increase as a substantial part of the excited sample surface is driven cumulatively into the high temperature IC phase.
- By quenching a sample, which is continuously pumped to the IC CDW phase, both symmetrically equivalent NC phases (α and β-type) appear in a probabilistic manner.

Both findings can be explained by considering the heat dissipation. Since the optically excited volume spans several hundred µm in diameter and just a few tens of nm in depth, the majority of the optically injected energy diffuses perpendicular to the layers, although the thermal conductivity of 1T-TaS$_2$ parallel to layers is roughly about a factor of ten higher than for the out-of-plane direction. Thus, if the time between two subsequent pump pulses is shorter than the sample requires to thermally equilibrate at its surface, the sample surface will cumulatively heat to an elevated base temperature depending on the applied pump fluence F and the repetition rate f, as also described in Sec. 7.1.2. For 1T-TaS$_2$ excited at the relatively high repetition rate of 125 kHz, by approaching a base temperature of 353 K, this has the consequence of a diverging transformation depth of the NC-IC phase transition. In combination with the slowed thermal diffusion due to the smaller temperature gradients, this gives rise to the drastically increased recovery times τ of the NC phase compared to low fluences. Hence, if the sample is continuously driven to the high-temperature IC phase, for the NCP, the required time to grow back to the surface exceeds the period between two successive excitation pulses, e.g, 8 µs for $f = 125$ kHz. Consequently, by quenching the sample from such an optically induced continuous ICP state, the long recovery time of the NC ground state facilitates the growth of both symmetrically equivalent α and β-type NCP orientations at the surface due to spontaneous nucleation at crystal defects or other impurities.

Interestingly, the generation of NCP twin domains is completely reversible by annealing the sample at a fluence, which briefly drives the CDW to the IC phase, but allows for a recovery within one excitation cycle. Thus, the surface of 1T-TaS$_2$ can be switched between a single crystalline NCP state and a probabilistic multi-domain state in a controlled manner, which bears some similarity to the all-optical switching of magnetized thin films [207].

In a recent publication, the reversible generation of domain boundaries between the two symmetry-equivalent NCP ground states has been also studied using MeV UED [208]. Here, the CDW amplitude mode frequency was found to be dependent on the amount of disorder induced in the NCP in terms of a domain wall network.

Challenges of ULEED implementations

Since this work covers the first application of ULEED in a backscattering geometry to study structural dynamics at surfaces, it is instructive to briefly discuss the experimental challenges of both its implementation in general and the analysis of 1T-TaS$_2$ in particular.

As the laser-driven electron source constitutes an integral component of the present ULEED experiment, its development is a continuously ongoing process. In this light, considerable work on the electron gun miniaturization was done by Gero Storeck in the context of his master's thesis and PhD work [173, 174]. It laid the foundation for the presently used mm-sized electron source and its four-electrode electrostatic lens-assembly. However, in order to avoid electrostatic stray fields and charging during operation, following this work, it took several iterations to identify the optimal electrode and insulator geometries and materials, respectively. The same applies for the design of the lens-assembly housing. As a result, the FPCB that has been developed in the context of the present thesis comprises a thin, but robust housing, which includes the electrical contacts and maintains a field-free exterior of the gun.Another challenge arises from identifying the spatio-temporal overlap of the laser excitation pulse and the electron probe pulse on the sample surface. In contrast to transmission electron diffraction, the backscattering geometry does not allow for directly locating the probed surface area of a few hundred µm^2 in size by means of a shadow image. A possible solution is to scan the electron beam over the mm-sized sample surface and to use the sample edges as reference positions. After achieving the spatial overlap, both pulses likewise need to coincide temporally. For optimizing the spatio-temporal overlap, it is beneficial to optically induce some structural changes, which have a pronounced influence on the diffraction pattern and, thus, can be easily recognized even using short integration times. In this context, the laser repetition rate f plays a crucial role: If it is chosen too low, the integration time gets very long due to the poor electron yield. On the other hand, if f is too high, the sample will simply heat up cumulatively, as discussed in the previous chapter. Hence, the delicate interplay of the repetition rate f, the applied pump fluence F and the thermal coupling of the sample to its environment sets a well-defined range of excitation conditions suitable to study the sought-after structural dynamics. Specifically, for cleaved samples consisting of layered structures, such as 1T-TaS$_2$, the thermal coupling of the topmost layers may be problematic. Cleaving such crystals often turns out not very reproducible, as it strongly depends on the defects at the sample edges. Hence, sometimes the outermost layers loose their connection to the bulk and easily heat up cumulatively during optical excitation. This is a possible explanation for the slightly different phase-transition threshold fluences that occur in the measurements of Sec. 5.1 and Sec. 7.1.2, respectively.

Another challenge, particularly concerning 1T-TaS$_2$, arises from the analysis of the time-resolved diffraction patterns. Here, the NCP and ICP diffraction peaks appear close to each other in k-space, and both are simultaneously visible within the window of temporal resolution after laser excitation. Consequently, it is difficult to discriminate the intensity of the remaining NCP satellite spot from the faint emerging ICP peak. This is additionally complicated by the fact that the latter reflex is very strongly broadened. For a better temporal resolution available with the µm-sized electron gun, at early delay times Δt, the ICP diffraction peak even extends beyond the position of the adjacent NCP peak, which makes a very careful analysis of both the intensity as well as the peak profile even more important.

Chapter 9

Conclusion

9.1 Summary

The present thesis comprises the first implementation of ULEED in a backscattering geometry, as well as its successful application to reveal the incommensurate CDW phase ordering kinetics at the surface of 1T-TaS$_2$. To this end, a novel electron source has been developed, which possesses the following key characteristics:

- Having an outer diameter of ~2 mm, the laser-driven electron gun allows for working distances of a few mm from the investigated sample surface.
- Utilizing a nanometric photocathode, a minimal electron pulse duration of 16.4 ps has been realized at an electron energy of 100 eV.
- Facilitated by the sharp needle photoemitter, the pulsed electron beam exhibits a remarkable transversal coherence. For the whole ULEED experiment, this leads to a transfer width of $w_t = 21 \pm 3$ nm, or, taking into account the signal-to-noise ratio, a maximum resolvable distance of $d_{max} \approx 128$ nm.

Moreover, the miniaturized laser-driven electron gun features further advantages that also make the ULEED setup interesting for a quasi-static operation. Besides the aforementioned outstanding k-space resolution, this includes the following aspects:

- The highly confined electron beam leads to a very small probing area. Whereas a conventional LEED system typically has a beam diameter of roughly 1 mm, the ULEED experiment is capable of analyzing single crystallites of only a few tens of µm in size.

- Despite the smaller beam diameter, the investigated surfaces are exposed to a very low electron dose, which is several orders of magnitude smaller compared to a LEED system with a standard phosphorous screen. Hence, the pulsed electron source is ideally suited to analyze very sensitive samples, such as bio-molecule adsorbates or polymer crystallites on a graphene substrate [36].

Generally, because of its backscattering geometry, ULEED is characterized by a significantly better thermal coupling of the investigated sample surface than it is the case for most other UED experiments probing thin films with high-energy electrons. This particular feature enables the use of relatively high repetition rates, which in turn lead to an increased signal-to-noise ratio, or, alternatively, allow for reducing the integration time of the individual diffraction patterns.

To demonstrate the capabilities of ULEED, the structural dynamics induced by CDWs at the surface of 1T-TaS$_2$ have been the subject of thorough investigations. Here, particular attention is paid to the transition from the NC to the IC CDW phase and its subsequent recovery. The central results can be summarized as follows:

- Repetitively driving the sample surface from the NC to the IC state requires an optical pump fluence of $F \approx 3.4$ mJ/cm^2 at a repetition rate of 25 kHz. As the CDW phase transition occurs significantly faster than the presently accessible temporal resolution, it cannot be resolved using the mm-sized electron source.
- Immediately after the phase transition, drastically broadened ICP diffraction peaks indicate a strongly reduced CDW correlation length ξ_{IC}. The subsequent narrowing of the peaks is traced over time using a spot profile analysis revealing a power-law scaling of the correlation length, i.e., $\xi_{IC}(\Delta t) \propto \Delta t^{1/2}$.
- The disorder in the “free-floating” IC CDW can be attributed to point-like topological defects, i.e., dislocations of the hexagonal CDW lattice. The unperturbed CDW recovers via annihilation of defects and antidefects, which is analogous to the coalescence of vortices in the XY-model.
- The observed scaling behavior has found to be independent of the applied pump fluence. Hence, the present topological defects are rather created as a result of the CDW phase transition than released thermally.
- A modified excitation scheme operated at 125 kHz enables the observation of a NC-IC phase transition reaching deeper into the bulk. In this regime, a quench causes the simultaneous formation of both symmetry-equivalent NCP ground states.

Finally, to corroborate the experimental findings, a numerical simulation of ICP charge-ordering kinetics has been conducted.

- This modeling qualitatively reproduces the appearance of topological defects during the IC CDW relaxation from a highly disordered state or the NC phase, respectively.
- Facilitated by the possibility to study the topological defect annihilation dynamics in real space, the temporal evolution of the associated correlation length likewise exhibits a power-law scaling featuring the same exponent of $\nu = 1/2$.

To summarize, this thesis introduces ULEED as a versatile tool for surface science and demonstrates the capability of this technique to trace transient structural disorder and phase-ordering kinetics. These results can be transformed to numerous other sample systems exhibiting so-far elusive fundamental physical phenomena at their surfaces.

9.2 Outlook

Taking 1T-TaS_2 as a starting point, this novel technique opens the door for the time-resolved analysis of an enormous wealth of sample systems, such as other TMDCs, heterostructures hereof or further CDW materials. Specific examples for the former include epitaxially grown layers of $MoSe_2$ on MoS_2 or HOPG substrates, likewise exhibiting IC and C CDW phases [209], as well as Au nanoparticles deposited on thin MoS_2 films, which allow for a reversible switching between its 1T and 2H polymorphs [210]. Further promising sample systems comprise the one-dimensional CDWs present in, e.g., Au nanowires on vicinal Si surfaces [211–213] or In nanowires grown on Si(111), which also have been previously studied by tr-RHEED [28]. Another intriguing material is the so-called “purple bronze” $K_{0.9}Mo_6O_{17}$, which exhibits a distinct surface CDW having a different critical temperature than the CDW present in the bulk [214]. Apart from layered structures and CDWs, exciting fundamental dynamics may also include structural phase transitions at the surface of quasicrystals [215] and the temperature-dependent formation of organic adsorbate superstructures on metal or semiconductor substrates [181, 216, 217].

Going beyond the vast number of possible future sample systems, further prospects for ULEED are the ongoing enhancement of the temporal resolution, as well as the application of more sophisticated excitation schemes.

Here, the continued gun miniaturization pursued by Gero Storeck paves the road for a routine use of the µm-sized electron source allowing for single ps temporal resolution [174].

An alternative, but also worthwhile approach is to enhance the temporal resolution of the mm-sized electron gun by means of ultrafast streaking or radio-frequency compression. Regarding the optical excitation of the surface, future experiments might include laser pulses featuring a wavelength and polarization precisely tailored to resonantly drive selected phonon modes. Alternatively, well-timed excitation pulse trains may be employed to coherently enhance or suppress cooperative atomic motions. Such excitation spectroscopy has the great advantage of being relatively independent of the temporal resolution determined by the electron source, since only the reaction product is probed in dependence on the time delay between successive laser pulses.

A more complex application for ULEED constitutes time-resolved surface crystallography. As the theoretical background to determine the surface structure unit cell from a set of energy dependent diffraction patterns is already well-proven for static LEED [59], the remaining challenges are rather of technical nature. First, a higher dielectric strength of the miniaturized source turns out necessary to use electron energies up to a few hundreds of eV. Secondly, energy-dependent measurements lead to broad range of electron propagation times. Hence, to maintain the spatio-temporal overlap of the laser and electron pulse, the optical path length in one of the two arms needs to be continuously adapted. While the latter difficulty is merely a question of adjustment, the former should be overcome in a future version of mm-sized electron gun, finally allowing for the time-resolved measurement of subtle atomic rearrangements with outstanding spatial accuracy.

To conclude, the successful realization of ULEED in a backscattering geometry opens a wide range of experimental possibilities. Aiming for disentangling the diverse ultrafast electronic and structural responses of surfaces driven highly out of equilibrium, ULEED represents an excellent complement to methods exclusively probing the electronic degrees of freedom, such as time-resolved ARPES [22, 113]. On the other hand, its remarkable sensitivity to long-range ordering phenomena make ULEED a highly complementary approach to methods focusing on the dynamics of the local structure, as it is the case for time-resolved STM [218]. In this context, the relatively simple and low-cost implementation renders ULEED an ideal tool for a broad scientific community and offers a significant upgrade of already existing time-resolved experiments.

Appendix A

Supplementary material

A.1 Preprocessing of the ULEED diffraction patterns

Generally, in a LEED experiment the directions of constructive interference are defined by the intersections of the reciprocal lattice “rods” with the surface of the Ewald sphere (cf. Sec. 2.1.4). Since the ULEED setup uses a planar imaging MCP detector instead of a hemispherical phosphorous screen, as in a conventional LEED system, the recorded diffraction patterns are subject to a pronounced pincushion distortion. Thus, particularly the areas of the diffraction pattern close to the edge of the MCP are elongated in radial direction. This effect is enhanced by a deceleration voltage applied to the MCP front plate in order to suppress inelastically scattered electrons.

For this reason, before their analysis, the diffraction patterns are distortion corrected. This procedure is realized in Matlab by means of a simulated annealing approach. It includes manual selection of all atomic lattice Bragg peaks and CDW satellite spots. Subsequently, the distance differences between equal diffraction peaks are minimized using a 2D polynomial transformation.

Additionally to the distortion correction, the overall intensity of the diffraction images is normalized to account for fluctuations of the electron yield. The latter may be caused by the fact that the nonlinear photoemission process inside the pulsed electron source is very sensitive to changes of the laser intensity or beam pointing. However, typically, intensity variations remain on the order of a few percent.

Finally, a 2D median filter removes so-called hot pixels caused by the camera, which would have a significant influence on the measured intensity of relatively weak diffraction spots. Hence, for each pixel of the diffraction pattern, this filter returns the median value of its eight adjacent neighbors.

A.2 Diffraction peak intensity evaluation

To evaluate the intensity of the atomic lattice Bragg peaks and CDW satellite spots inside each diffraction pattern recorded at time delays Δt, first, the approximate positions of the peaks are marked manually. Subsequently, further positional refinement is done by fitting each diffraction spot with a 2D Gaussian to correctly identify its center of mass. For the actual intensity analysis, disk- and ring-like masks are placed around each peak. While the mean intensity measured within the ring around the peak serves as a background correction, the integrated and maximum diffraction spot intensities are obtained from the mean and maximum values inside the disk-like mask. For the analysis of the NC-IC CDW phase transition, it is important to carefully choose the sizes of the respective masks, as both types of CDW satellite spots are located very close to each other. Consequently, separation of the integrated intensities may turn out particularly challenging, if both types of CDW peaks are simultaneously present due to a low temporal resolution and/or if the peaks merge because of an insufficient spatial resolution. For the evaluation of the diffracted intensities recorded with the mm-sized and µm-sized electron source, the radii of the disk-like masks are 0.058Å^{-1} (20 pixels) and 0.066Å^{-1} (30 pixels), respectively, whereas the ring for background correction is 3 pixels wide for both measurements.

Finally, the measured intensity evolutions of the individual diffraction peaks are normalized and averaged over all available spots of equal diffraction order.

A.3 Two-dimensional spot profile analysis

To study the temporal evolution of the ICP diffraction peaks, a time-resolved spot profile analysis is performed. To this end, the IC CDW satellite spots are fitted with a 2D convolution of the respective instrument function and an elliptical Lorentzian profile (cf. Sec. 5.2). Since the ICP peaks appear to be broadened in the azimuthal direction with respect to the nearest atomic lattice Bragg peak, for each fit, the orientation of the elliptical Lorentzian contribution is determined by the position of the corresponding Bragg peak (Fig. 5.1). Fig. A.1 shows the inverse of the fitted widths w_r and w_a (FWHM) in radial and azimuthal direction depicted as circles and triangles, respectively. During the diffraction peak narrowing, the ellipticity of the peaks (i.e., the ratio of w_r and w_a) remains relatively constant, which manifests as a constant offset in Fig. A.1.

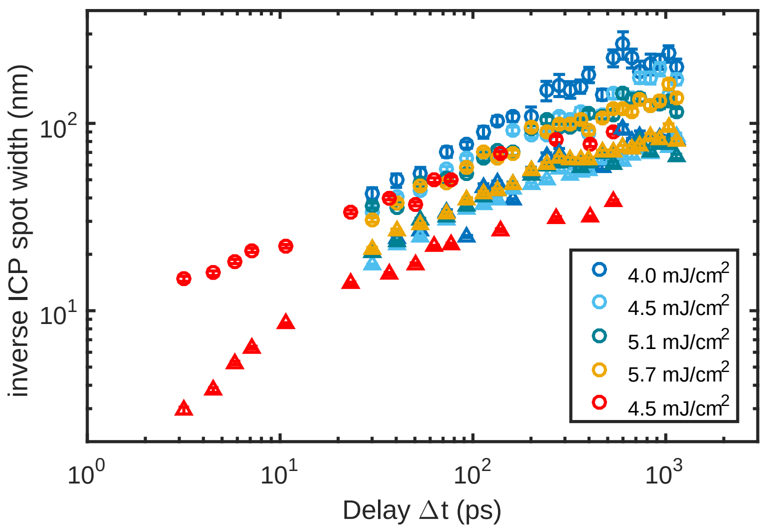

Figure A.1: The inverse of the widths (FWHM) w_r and w_a of the IC CDW diffraction peaks in radial and azimuthal direction is depicted as circles and triangles, respectively. In a double logarithmic plot vs. delay time Δt both quantities exhibit a similar temporal evolution. The vertical offset relates to a constant ellipticity ratio of both diffraction spot semi-axes, which correspond to the radial and azimuthal direction with respect to the adjacent atomic lattice Bragg peak.

A.4 Static transition to the commensurate CDW phase

Upon cooling below 180 K, the CDW modulation in 1T-TaS$_2$ undergoes a transition from the NC to the C CDW phase, as described in Sec. 3.1. Starting in the room-temperature NC phase, the CDW is characterized by an almost regular hexagonal pattern of commensurate patches. During cooling these patches grow in size, thus causing the previously split CDW satellite diffraction spots to merge. This process can be observed well by means of ULEED due to the large transfer width of this instrument. It is depicted in Fig. A.2 for four exemplary temperatures.

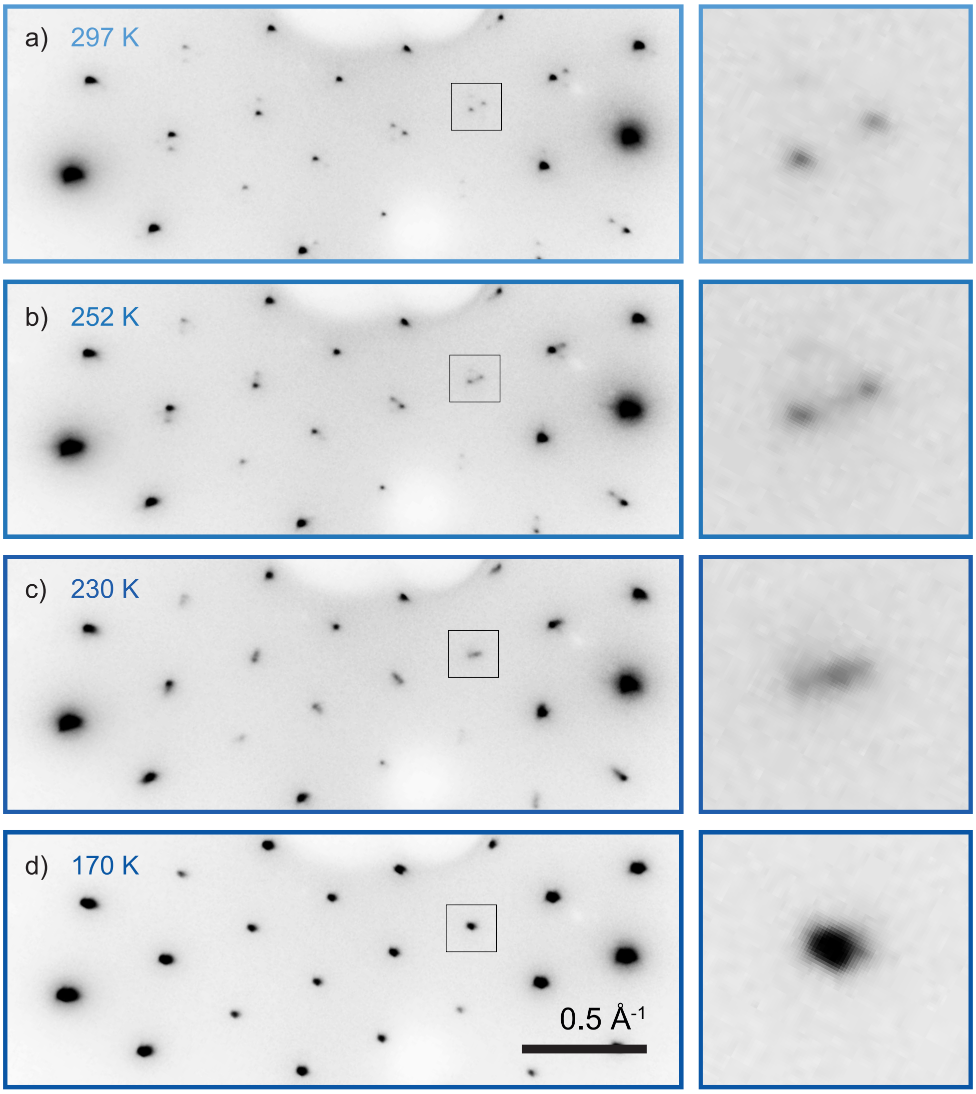

Figure A.2: ULEED diffraction patterns recorded at the surface of 1T-TaS$_2$ during cooling from the NC CDW phase (**a** - **c**) to the C CDW phase (**d**) (180 s integration time). As the commensurate patches of the NC phase grow with lower temperatures, the distance between previously split CDW diffraction peaks decreases, as depicted in the close-ups on the right side of panel **a** to **c**. Diffraction patterns courtesy of J. G. Horstmann and T. Diekmann.

A.5 Characterization of topological defects in numeric simulation

In order to study the temporal evolution of topological defects in the triple IC CDW, it is necessary to identify all pitchfork dislocations inside each of the three complex order parameters ψ_j and to assign them with their correct Burgers vectors.
Therefore, the following procedure is carried out for each contribution ψ_j:

1. The complex phase $\arg\left(\psi_j\left(\boldsymbol{r}\right)\right)$ is corrected for the fast oscillatory components caused by $\boldsymbol{q}_j^{IC}$ inside the unit cell of the CDW lattice. The result is a phase map $\varphi_j\left(\boldsymbol{r}\right)$, which features singularities at the cores of the pitchfork dislocations independent of their winding number.
2. The phase is integrated while traversing around each pixel in $\varphi_j\left(\boldsymbol{r}\right)$ on a closed contour. To this end, four replicas of $\varphi_j\left(\boldsymbol{r}\right)$ are shifted by 1 px in x, y, $-x$ and $-y$ direction, respectively, and summed up. Due to the periodic boundary conditions of ψ_j, circular shifts of the simulation domain maintain conservation of defects at its edge.
3. Regions featuring an accumulated phase difference of 2π are associated to dislocation defects with a Burgers vectors pointing in $\boldsymbol{q}_j^{IC}$ direction. Correspondingly, a phase difference of -2π resembles an anti-defect having a Burgers vector in $-\boldsymbol{q}_j^{IC}$ direction.
4. If several adjacent pixel exhibit a phase difference of $\pm 2\pi$, the centroid of the respective area is calculated and all respective pixels are counted as a single dislocation defect.

This way, all pairs of pitchfork dislocations (also denoted as vortex-antivortex pairs) in ψ_j can be identified and assigned to their Burgers vectors. It is worth noting that, due to the periodic boundary conditions, the numbers of defects and anti-defects are identical at all times. To form a topological defect of the triple CDW, two dislocations of ψ_j and ψ_k need come across each other. Then, the Burgers vector of the new defect simply results from vector addition of the two constituents.

Appendix B

Abbreviations and Symbols

B.1 Abbreviations

AES	Auger electron spectroscopy
ARPES	angle-resolved photoelectron spectroscopy
BP	Bragg peaks
BZ	Brillouin zone
CDW	charge-density wave
CP	commensurate phase
DPSS	diode-pumped solid state
FIB	focused ion beam
FPCB	flexible printed circuit board
fs	femtosecond
FWHM	full width at half maximum
HHG	high harmonic generation
HOPG	highly oriented pyrolytic graphite
ICP	incommensurate phase
IMFP	inelastic mean free path
KTHNY	Kosterlitz, Thouless, Halperin, Nelson, Young
LEED	low-energy electron diffraction
LEEM	low-energy electron microscopy
MCP	microchannel plate
mm	millimeter
NCP	nearly commensurate phase
NLSE	nonlinear Schrödinger equation

nm	nanometer
NOPA	noncollinear optical parametric amplifier
OPA	optical parametric amplifier
PDE	partial differential equation
PES	photoemission spectroscopy
PLD	periodic lattice distortion
ps	picosecond
RHEED	reflection high-energy electron diffraction
SOFM	split-operator Fourier method
SPA	spot profile analysis
SXRD	surface x-ray diffraction
TEF	transient electric field
TMDC	transition metal dichalcogenide
TP	triclinic phase
TPD	temperature programmed desorption
UED	ultrafast electron diffraction
UHV	ultrahigh vacuum
ULEED	ultrafast low-energy electron microscopy
ULEEM	ultrafast low-energy electron microscope
UTEM	ultrafast transmission electron microscopy
XRD	x-ray diffraction

B.2 Symbols

α	angle, charge density modulation, chiral CDW ground state
β	chiral CDW ground state
γ	angle, probability
Δ	band gap
ε	emittance
η	field enhancement
θ	bond angle
λ	wavelength
Λ	inelastic mean free path of electrons
μ	chemical potential

ν	angle, frequency
ξ	coherence length, correlation length
ρ	charge density, defect density
σ	angular spread, momentum spread
τ	temporal spread, decay constant
ϕ	complex amplitude, phase
φ	phase
χ	electronic susceptibility
Φ	pair correlation function, work function
ψ	wave function, complex order parameter
ω	frequency
Ω	solid angle

$\boldsymbol{a}_i$	lattice vector
$\boldsymbol{a}_i^*$	reciprocal lattice vector
a	lattice parameter, accuracy
A	area
$\boldsymbol{b}$	superstructure lattice vector, Burgers vector
B	brightness
c	speed of light
C	Cauchy distribution
$\hat{C}$	constant operator
d	distance, dimension
$\hat{D}$	dispersive operator
D	domain diameter
e	electron charge
E	(kinetic) energy
f	scattering amplitude, repetition rate, Fermi-Dirac distribution
F	force, field strength, pump fluence, free energy
$\lvert F\rvert^2$	unit cell form factor
$\mathcal{F}$	Fourier transform
g	electron-phonon coupling constant
g_6	orientational correlation function
g_T	translational correlation function

$\boldsymbol{G}$	reciprocal lattice vector
h	Planck's constant
H	magnetic field
I	intensity, current
$\boldsymbol{J}$	current
J_1	first-order Bessel function
$\boldsymbol{k}$	wave vector
k	tip geometry factor
k_B	Boltzmann constant
$\boldsymbol{K}$	scattering vector
K_A	Franck's constant
L	distance, closed contour
m	mass, magnetization density
M	transfer Matrix
n	components of topological defect
$\hat{N}$	nonlinear operator
p	momentum, probability
$\boldsymbol{q}$	wave vector
$\boldsymbol{r}$	real space vector
r	radius
$\boldsymbol{R}_{mn}$	position in 2D lattice
R	distance
s	spin
$\|S\|^2$	lattice structure factor
t	time, transfer function
T	temperature, instrument response function
$\boldsymbol{u}$	atomic displacement
U	potential
v	velocity
V	potential
w	(transfer) width, winding number

Bibliography

[1] U. Bovensiepen, H. Petek, and M. Wolf. *Dynamics at Solid State Surfaces and Interfaces: Volume 1 - Current Developments*. John Wiley & Sons, 2010. Cited on pages 1, 3 and 23.

[2] H. Petek and S. Ogawa. Femtosecond time-resolved two-photon photoemission studies of electron dynamics in metals. *Progress in Surface Science*, 56(4):239–310, 1997. Cited on pages 1 and 23.

[3] M. Wolf. Femtosecond dynamics of electronic excitations at metal surfaces. *Surface Science*, European Conference on Surface Science 377:343–349, 1997. Cited on pages 1 and 23.

[4] U. Höfer, I. L. Shumay, C. Reuß, U. Thomann, W. Wallauer, and T. Fauster. Time-Resolved Coherent Photoelectron Spectroscopy of Quantized Electronic States on Metal Surfaces. *Science*, 277(5331):1480–1482, 1997. Cited on pages 1 and 23.

[5] G. Binnig, H. Rohrer, C. Gerber, and E. Weibel. Surface Studies by Scanning Tunneling Microscopy. *Physical Review Letters*, 49(1):57–61, 1982. Cited on pages 1 and 8.

[6] L. J. Clarke. *Surface crystallography: an introduction to low energy electron diffraction*. A Wiley-Interscience publication. Chichester [u.a.]: Wiley, 1985. Cited on pages 1, 2, 8, 9, 16, 23 and 24.

[7] A. K. Geim and K. S. Novoselov. The rise of graphene. *Nature Materials*, 6(3):183–191, 2007. Cited on page 1.

[8] K. Rossnagel. On the origin of charge-density waves in select layered transition-metal dichalcogenides. *Journal of Physics: Condensed Matter*, 23(21):213001, 2011. Cited on pages 1, 28, 29, 30, 31, 33, 34, 35, 51, 52, 57 and 58.

[9] J. A. Wilson, F. J. Di Salvo, and S. Mahajan. Charge-density waves in metallic, layered, transition-metal dichalcogenides. *Physical review letters*, 32(16):882, 1974. Cited on pages 1 and 51.

[10] J. M. Kosterlitz and D. J. Thouless. Ordering, metastability and phase transitions in two-dimensional systems. *Journal of Physics C: Solid State Physics*, 6(7):1181, 1973. Cited on pages 1 and 37.

[11] H. E. Hall and W. F. Vinen. The Rotation of Liquid Helium II. I. Experiments on the Propagation of Second Sound in Uniformly Rotating Helium II. *Proceedings of the Royal Society A: Mathematical, Physical and Engineering Sciences*, 238(1213):204–214, 1956. Cited on page 1.

[12] H. E. Hall and W. F. Vinen. The Rotation of Liquid Helium II. II. The Theory of Mutual Friction in Uniformly Rotating Helium II. *Proceedings of the Royal Society A: Mathematical, Physical and Engineering Sciences*, 238(1213):215–234, 1956. Cited on page 1.

[13] T. Shinjo. Magnetic Vortex Core Observation in Circular Dots of Permalloy. *Science*, 289(5481):930–932, 2000. Cited on page 1.

[14] J. E. Moore. The birth of topological insulators. en. *Nature*, 464:194–198, 2010. Cited on pages 1 and 37.

[15] M. Z. Hasan and C. L. Kane. Colloquium: Topological insulators. *Reviews of Modern Physics*, 82(4):3045–3067, 2010. Cited on pages 1 and 37.

[16] H. Kroemer. Nobel Lecture: Quasielectric fields and band offsets: teaching electrons new tricks. *Reviews of Modern Physics*, 73(3):783–793, 2001. Cited on page 2.

[17] K. Wandelt. *Surface and Interface Science, Volume 1: Concepts and Methods*. Weinheim: Wiley-VCH, 2012. Cited on pages 2, 8, 23, 63 and 64.

[18] M. A. V. Hove, W. H. Weinberg, and C.-M. Chan. *Low-energy electron diffraction: experiment, theory and surface structure determination*. Springer-Verlag, 1986. Cited on pages 2, 9 and 16.

[19] E. Bauer. Low energy electron microscopy. *Reports on Progress in Physics*, 57(9):895, 1994. Cited on page 2.

[20] H. Conrad, G. Ertl, and E. E. Latta. Adsorption of hydrogen on palladium single crystal surfaces. *Surface Science*, 41(2):435–446, 1974. Cited on page 3.

[21] S. Eich, A. Stange, A. V. Carr, J. Urbancic, T. Popmintchev, M. Wiesenmayer, K. Jansen, A. Ruffing, S. Jakobs, T. Rohwer, S. Hellmann, C. Chen, P. Matyba, L. Kipp, K. Rossnagel, M. Bauer, M. M. Murnane, H. C. Kapteyn, S. Mathias, and M. Aeschlimann. Time- and angle-resolved photoemission spectroscopy with optimized high-harmonic pulses using frequency-doubled Ti:Sapphire lasers. *Journal of Electron Spectroscopy and Related Phenomena*, 195:231–236, 2014. Cited on page 3.

[22] L. Perfetti, P. A. Loukakos, M. Lisowski, U. Bovensiepen, H. Berger, S. Biermann, P. S. Cornaglia, A. Georges, and M. Wolf. Time Evolution of the Electronic Structure of 1T-TaS2 through the Insulator-Metal Transition. *Physical Review Letters*, 97(6):067402, 2006. Cited on pages 3, 60 and 122.

[23] J. C. Petersen, S. Kaiser, N. Dean, A. Simoncig, H. Y. Liu, A. L. Cavalieri, C. Cacho, I. C. E. Turcu, E. Springate, F. Frassetto, L. Poletto, S. S. Dhesi, H. Berger, and A. Cavalleri. Clocking the Melting Transition of Charge and Lattice Order in 1T-TaS2 with Ultrafast Extreme-Ultraviolet Angle-Resolved Photoemission Spectroscopy. *Physical Review Letters*, 107(17):177402, 2011. Cited on pages 3 and 60.

[24] A. Paarmann, M. Gulde, M. Müller, S. Schäfer, S. Schweda, M. Maiti, C. Xu, T. Hohage, F. Schenk, C. Ropers, and R. Ernstorfer. Coherent femtosecond low-energy single-electron pulses for time-resolved diffraction and imaging: A numerical study. *Journal of Applied Physics*, 112(11):113109, 2012. Cited on pages 3 and 68.

[25] H. E. Elsayed-Ali and J. W. Herman. Picosecond time-resolved surface-lattice temperature probe. *Applied Physics Letters*, 57(15):1508–1510, 1990. Cited on pages 3 and 63.

[26] S. Schäfer, W. Liang, and A. H. Zewail. Structural dynamics and transient electric-field effects in ultrafast electron diffraction from surfaces. *Chemical Physics Letters*, 493(1–3):11–18, 2010. Cited on page 3.

[27] S. Wall, B. Krenzer, S. Wippermann, S. Sanna, F. Klasing, A. Hanisch-Blicharski, M. Kammler, W. G. Schmidt, and M. Horn-von Hoegen. Atomistic Picture of Charge Density Wave Formation at Surfaces. *Physical Review Letters*, 109(18):186101, 2012. Cited on pages 3 and 63.

[28] T. Frigge, B. Hafke, T. Witte, B. Krenzer, C. Streubühr, A. Samad Syed, V. Mikšić Trontl, I. Avigo, P. Zhou, M. Ligges, D. von der Linde, U. Bovensiepen, M. Horn-von Hoegen, S. Wippermann, A. Lücke, S. Sanna, U. Gerstmann, and W. G. Schmidt. Optically excited structural transition in atomic wires on surfaces at the quantum limit. *Nature*, 544(7649):207–211, 2017. Cited on pages 3, 28, 63, 78 and 121.

[29] S. Schäfer, W. Liang, and A. H. Zewail. Structural dynamics of surfaces by ultrafast electron crystallography: Experimental and multiple scattering theory. *The Journal of Chemical Physics*, 135(21):214201, 2011. Cited on page 3.

[30] C. Ropers, D. R. Solli, C. P. Schulz, C. Lienau, and T. Elsaesser. Localized Multiphoton Emission of Femtosecond Electron Pulses from Metal Nanotips. *Physical Review Letters*, 98(4):043907, 2007. Cited on pages 4, 68 and 69.

[31] P. Hommelhoff, Y. Sortais, A. Aghajani-Talesh, and M. A. Kasevich. Field Emission Tip as a Nanometer Source of Free Electron Femtosecond Pulses. *Physical Review Letters*, 96(7):077401, 2006. Cited on pages 4 and 69.

[32] D. Ehberger, J. Hammer, M. Eisele, M. Krüger, J. Noe, A. Högele, and P. Hommelhoff. Highly Coherent Electron Beam from a Laser-Triggered Tungsten Needle Tip. *Physical Review Letters*, 114(22):227601, 2015. Cited on pages 4 and 69.

[33] A. Feist, N. Bach, N. Rubiano da Silva, T. Danz, M. Möller, K. E. Priebe, T. Domröse, J. G. Gatzmann, S. Rost, J. Schauss, S. Strauch, R. Bormann, M. Sivis, S. Schäfer, and C. Ropers. Ultrafast transmission electron microscopy using a laser-driven field emitter: Femtosecond resolution with a high coherence electron beam. *Ultramicroscopy*, 176:63–73, 2017. Cited on pages 4, 20 and 76.

[34] E. Quinonez, J. Handali, and B. Barwick. Femtosecond photoelectron point projection microscope. *Review of Scientific Instruments*, 84(10):103710, 2013. Cited on page 4.

[35] M. Müller, A. Paarmann, and R. Ernstorfer. Femtosecond electrons probing currents and atomic structure in nanomaterials. *Nature Communications*, 5:5292, 2014. Cited on pages 4 and 65.

[36] M. Gulde, S. Schweda, G. Storeck, M. Maiti, H. K. Yu, A. M. Wodtke, S. Schafer, and C. Ropers. Ultrafast low-energy electron diffraction in transmission resolves

polymer/graphene superstructure dynamics. *Science*, 345(6193):200–204, 2014. Cited on pages 4, 10, 65 and 120.

[37] S. Vogelgesang, G. Storeck, J. G. Horstmann, T. Diekmann, M. Sivis, S. Schramm, K. Rossnagel, S. Schäfer, and C. Ropers. Phase ordering of charge density waves traced by ultrafast low-energy electron diffraction. *Nature Physics*, 14(2):184–190, 2018. Cited on pages 4, 78 and 79.

[38] R. K. Gehrenbeck. Electron diffraction: fifty years ago. *Physics today*, 31(1):34–41, 1978. Cited on pages 7 and 8.

[39] M. Born. Physical Aspects of Quantum Mechanics. *Nature*, 119:354, 1927. Cited on page 8.

[40] C. Davisson and L. H. Germer. The Scattering of Electrons by a Single Crystal of Nickel. *Nature*, 119(2998):558, 1927. Cited on page 8.

[41] G. P. Thomson and A. Reid. Diffraction of Cathode Rays by a Thin Film. *Nature*, 119:890, 1927. Cited on page 8.

[42] *The Nobel Prize in Physics 1937*. Cited on page 8.

[43] W. Ehrenberg. A new method of investigating the diffraction of slow electrons by crystals. *The London, Edinburgh, and Dublin Philosophical Magazine and Journal of Science*, 18(122):878–901, 1934. Cited on page 8.

[44] J. J. Lander, J. Morrison, and F. Unterwald. Improved Design and Method of Operation of Low Energy Electron Diffraction Equipment. *Review of Scientific Instruments*, 33(7):782–783, 1962. Cited on pages 8 and 16.

[45] C. Bai. *Scanning Tunneling Microscopy and Its Application*. Springer Science & Business Media, 2000. Cited on page 8.

[46] *The Nobel Prize in Physics 1986*. Cited on page 8.

[47] M. P. Seah and W. A. Dench. Quantitative electron spectroscopy of surfaces: A standard data base for electron inelastic mean free paths in solids. *Surface and Interface Analysis*, 1(1):2–11, 1979. Cited on page 9.

[48] T. Fauster, L. Hammer, K. Heinz, and A. Schneider. *Oberflächenphysik, Grundlagen und Methoden*. Berlin, Boston: De Gruyter, 2013. Cited on pages 10 and 23.

[49] M. Henzler and W. Göpel. *Oberflächenphysik des Festkörpers*. Vieweg+Teubner Verlag, 1994. Cited on pages 11, 12, 16, 18, 22, 25, 26 and 27.

[50] W. Demtröder. *Experimentalphysik 2: Elektrizität und Optik*. 5 edition, Berlin; Heidelberg: Springer, 2008. Cited on page 12.

[51] C. Kittel. *Einführung in die Festkörperphysik*. Oldenbourg Wissenschaftsverlag, 2013. Cited on pages 12 and 40.

[52] R. Gross and A. Marx. *Festkörperphysik*. 2., akt. Aufl. edition, Berlin, Boston: De Gruyter Oldenbourg, 2014. Cited on pages 15, 16, 24 and 40.

[53] M. J. Stern, L. P. René de Cotret, M. R. Otto, R. P. Chatelain, J.-P. Boisvert, M. Sutton, and B. J. Siwick. Mapping momentum-dependent electron-phonon coupling and nonequilibrium phonon dynamics with ultrafast electron diffuse scattering. *Physical Review B*, 97(16):165416, 2018. Cited on page 16.

[54] L. Waldecker, R. Bertoni, H. Hübener, T. Brumme, T. Vasileiadis, D. Zahn, A. Rubio, and R. Ernstorfer. Momentum-Resolved View of Electron-Phonon Coupling in Multilayer WSe2. *Physical Review Letters*, 119(3):036803, 2017. Cited on page 16.

[55] S. Schweda. *Entwicklung eines Experiments zur zeitaufgelösten Beugung niederenergetischer Elektronen*. MA thesis. Georg-August-University Göttingen, 2013. Cited on pages 17, 67 and 69.

[56] P. Zahl and M. Horn-von Hoegen. Third-generation conical spot profile analyzing low-energy electron diffraction. *Review of Scientific Instruments*, 73(8):2958–2962, 2002. Cited on page 17.

[57] U. Scheithauer, G. Meyer, and M. Henzler. A new LEED instrument for quantitative spot profile analysis. *Surface Science*, 178(1):441–451, 1986. Cited on pages 17 and 18.

[58] C. Klein, T. Nabbefeld, H. Hattab, D. Meyer, G. Jnawali, M. Kammler, F.-J. M. zu Heringdorf, A. Golla-Franz, B. H. Müller, T. Schmidt, M. Henzler, and M. Horn-von Hoegen. Lost in reciprocal space? Determination of the scattering condition in spot profile analysis low-energy electron diffraction. *Review of Scientific Instruments*, 82(3):035111, 2011. Cited on page 17.

[59] M. A. v. Hove and S. Y. Tong. *Surface Crystallography by LEED: Theory, Computation and Structural Results*. Springer Series in Chemical Physics. Berlin Heidelberg: Springer-Verlag, 1979. Cited on pages 18 and 122.

[60] M. Reiser. *Theory and Design of Charged Particle Beams*. 2 edition edition, Weinheim: Wiley-VCH, 2008. Cited on pages 19 and 20.

[61] A. Septier. *Applied charged particle optics*. Advances in electronics and electron physics : Supplement 13A. New York [u.a.]: Academic Press, 1980. Cited on pages 19 and 20.

[62] D. R. Frankl. Comments on “coherence length and/or transfer width?”. *Surface Science*, 84(2):L485–L488, 1979. Cited on page 21.

[63] D. B. Williams and C. B. Carter. *Transmission Electron Microscopy: A Textbook for Materials Science*. Springer Science & Business Media, 2009. Cited on page 21.

[64] W. Lauterborn and T. Kurz. *Coherent Optics: Fundamentals and Applications*. 2 edition, Advanced Texts in Physics. Berlin Heidelberg: Springer-Verlag, 2003. Cited on page 21.

[65] T. van Oudheusden, E. F. de Jong, S. B. van der Geer, W. P. E. M. O. ’t Root, O. J. Luiten, and B. J. Siwick. Electron source concept for single-shot sub-100 fs electron diffraction in the 100 keV range. *Journal of Applied Physics*, 102(9):093501, 2007. Cited on page 21.

[66] R. L. Park, J. E. Houston, and D. G. Schreiner. The LEED Instrument Response Function. *Review of Scientific Instruments*, 42(1):60–65, 1971. Cited on page 22.

[67] J. E. Houston and R. L. Park. Low-energy electron diffraction from imperfect structures. *Surface Science*, 21(2):209–223, 1970. Cited on pages 22 and 27.

[68] T. M. Lu and M. G. Lagally. The resolving power of a low-energy electron diffractometer and the analysis of surface defects. *Surface Science*, 99(3):695–713, 1980. Cited on page 22.

[69] K. D. Gronwald and M. Henzler. Epitaxy of Si(111) as studied with a new high resolving LEED system. *Surface Science*, 117(1):180–187, 1982. Cited on pages 22 and 76.

[70] L. Merz and K.-H. Ernst. Unification of the matrix notation in molecular surface science. *Surface Science*, 604(11-12):1049–1054, 2010. Cited on pages 23 and 53.

[71] A. Ichimiya and P. I. Cohen. *Reflection High-Energy Electron Diffraction*. Cambridge, U.K. ; New York: Cambridge University Press, 2004. Cited on page 27.

[72] H. Fröhlich and F. R. S. On the theory of superconductivity: the one-dimensional case. *Proc. R. Soc. Lond. A*, 223(1154):296–305, 1954. Cited on pages 28, 29 and 34.

[73] R. E. Peierls. *Quantum Theory of Solids*. Oxford Classic Texts in the Physical Sciences. Oxford, New York: Oxford University Press, 2001. Cited on pages 28, 29 and 31.

[74] N. P. Ong and P. Monceau. Anomalous transport properties of a linear-chain metal: NbSe3. *Physical Review B*, 16(8):3443–3455, 1977. Cited on page 28.

[75] P. Monçeau, N. P. Ong, A. M. Portis, A. Meerschaut, and J. Rouxel. Electric Field Breakdown of Charge-Density-Wave-Induced Anomalies in NbSe3. *Physical Review Letters*, 37(10):602–606, 1976. Cited on page 28.

[76] J. A. Wilson, F. J. D. Salvo, and S. Mahajan. Charge-density waves and superlattices in the metallic layered transition metal dichalcogenides. *Advances in Physics*, 24(2):117–201, 1975. Cited on pages 28, 51, 52, 53, 59 and 106.

[77] S. Roth and D. Carroll. *One-Dimensional Metals: Conjugated Polymers, Organic Crystals, Carbon Nanotubes and Graphene*. 3 edition edition, Weinheim: Wiley-VCH, 2015. Cited on pages 28, 32, 33 and 35.

[78] N. Goldenfeld. *Lectures on phase transitions and the renormalization group*. Addison-Wesley, Advanced Book Program, 1992. Cited on pages 28 and 91.

[79] W. L. McMillan. Landau theory of charge-density waves in transition-metal dichalcogenides. *Physical Review B*, 12(4):1187–1196, 1975. Cited on pages 28, 29, 35, 46, 47, 48, 52 and 92.

[80] G. Grüner. The dynamics of charge-density waves. *Reviews of modern physics*, 60(4):1129, 1988. Cited on pages 30, 33 and 36.

[81] J. Sólyom. *Fundamentals of the Physics of Solids: Volume 3 - Normal, Broken-Symmetry, and Correlated Systems*. 2011 edition edition, Berlin ; New York: Springer, 2011. Cited on pages 31, 35, 45, 46 and 54.

[82] T. Frigge. *Ultraschnelle strukturelle Nichtgleichgewichtsdynamik des optisch angeregten Si(111)(8x2)->(4x1)-In Phasenübergangs*. PhD thesis. Duisburg: Universität Duisburg-Essen, 2016. Cited on page 31.

[83] W. Kohn. Image of the Fermi Surface in the Vibration Spectrum of a Metal. *Physical Review Letters*, 2(9):393, 1959. Cited on pages 31 and 33.

[84] R. H. Friend and D. Jerome. Periodic lattice distortions and charge density waves in one- and two-dimensional metals. *Journal of Physics C: Solid State Physics*, 12(8):1441, 1979. Cited on page 32.

[85] R. Stedman, L. Almqvist, G. Nilsson, and G. Raunio. Fermi Surface of Lead from Kohn Anomalies. *Physical Review*, 163(3):567–574, 1967. Cited on page 34.

[86] R. Stedman and G. Nilsson. Observations on the Fermi Surface of Aluminum by Neutron Spectrometry. *Physical Review Letters*, 15(15):634–637, 1965. Cited on page 34.

[87] E. Tosatti. Displacive reconstruction phase transitions of clean transition metal and semiconductor surfaces. *Modern Trends in the Theory of Condensed Matter*:501–530, 1980. Cited on page 34.

[88] N. F. Mott. The Basis of the Electron Theory of Metals, with Special Reference to the Transition Metals. *Proceedings of the Physical Society. Section A*, 62(7):416, 1949. Cited on page 35.

[89] A. W. Overhauser. Observability of Charge-Density Waves by Neutron Diffraction. *Physical Review B*, 3(10):3173–3182, 1971. Cited on pages 35 and 96.

[90] L. D. Chapman and R. Colella. Experimental Evidence from X-Ray Diffraction for Phase Excitations in Solids. *Physical Review Letters*, 52(8):652–655, 1984. Cited on pages 36, 56 and 59.

[91] T. Diekmann. *Incommensurate charge-density wave dynamics in 1T-TaS2 probed by ultrafast LEED.* MA thesis. Göttingen: Georg-August-University Göttingen, 2017. Cited on pages 36, 72 and 88.

[92] N. D. Mermin. The topological theory of defects in ordered media. *Reviews of Modern Physics*, 51(3):591–648, 1979. Cited on pages 37, 38 and 41.

[93] *The Nobel Prize in Physics 2016*. Cited on page 37.

[94] J. P. Sethna. Order parameters, broken symmetry, and topology. *arXiv preprint cond-mat/9204009*, 1992. Cited on pages 37, 39 and 40.

[95] W. H. Zurek. Cosmological experiments in superfluid helium? *Nature*, 317(6037):505–508, 1985. Cited on pages 37 and 112.

[96] T. Eggebrecht, M. Möller, J. G. Gatzmann, N. Rubiano da Silva, A. Feist, U. Martens, H. Ulrichs, M. Münzenberg, C. Ropers, and S. Schäfer. Light-Induced Metastable Magnetic Texture Uncovered by in situ Lorentz Microscopy. *Physical Review Letters*, 118(9):097203, 2017. Cited on page 37.

[97] P. M. Chaikin and T. C. Lubensky. *Principles of Condensed Matter Physics*. Cambridge University Press, 2000. Cited on pages 37, 38, 39, 40, 47, 48, 50 and 113.

[98] A. Y. Kitaev. Fault-tolerant quantum computation by anyons. *Annals of Physics*, 303(1). arXiv: quant-ph/9707021:2–30, 2003. Cited on page 38.

[99] D. Hull. *Introduction to Dislocations*. 5. Auflage. edition, Amsterdam: Butterworth-Heinemann, 2011. Cited on pages 40, 48 and 93.

[100] A. J. Bray. Theory of phase-ordering kinetics. *Advances in Physics*, 51(2):481–587, 2002. Cited on pages 41, 92 and 113.

[101] A. Jelić and L. F. Cugliandolo. Quench dynamics of the 2d XY model. *Journal of Statistical Mechanics: Theory and Experiment*, 2011(02):P02032, 2011. Cited on pages 41 and 113.

[102] G. Gompper and M. Schick, eds. *Soft Matter*. Weinheim, Germany: Wiley-VCH Verlag GmbH & Co. KGaA, 2007. Cited on pages 42, 43 and 48.

[103] D. R. Nelson and B. I. Halperin. Dislocation-mediated melting in two dimensions. *Physical Review B*, 19(5):2457–2484, 1979. Cited on page 42.

[104] N. D. Mermin and H. Wagner. Absence of Ferromagnetism or Antiferromagnetism in One- or Two-Dimensional Isotropic Heisenberg Models. *Physical Review Letters*, 17(22):1133–1136, 1966. Cited on page 42.

[105] V. Narayan, N. Menon, and S. Ramaswamy. Nonequilibrium steady states in a vibrated-rod monolayer: tetratic, nematic, and smectic correlations. *Journal of Statistical Mechanics: Theory and Experiment*, 2006(01):P01005, 2006. Cited on page 43.

[106] R. Pindak, D. E. Moncton, S. C. Davey, and J. W. Goodby. X-Ray Observation of a Stacked Hexatic Liquid-Crystal B Phase. *Physical Review Letters*, 46(17):1135–1138, 1981. Cited on page 43.

[107] C. Eisenmann, U. Gasser, P. Keim, and G. Maret. Anisotropic Defect-Mediated Melting of Two-Dimensional Colloidal Crystals. *Physical Review Letters*, 93(10):105702, 2004. Cited on pages 43 and 44.

[108] A. L. Thorneywork, J. L. Abbott, D. G. A. L. Aarts, P. Keim, and R. P. A. Dullens. Bond-orientational order and Frank's constant in two-dimensional colloidal hard spheres. *Journal of Physics: Condensed Matter*, 30(10):104003, 2018. Cited on pages 43 and 44.

[109] U. Gasser. Crystallization in three- and two-dimensional colloidal suspensions. en. *Journal of Physics: Condensed Matter*, 21(20):203101, 2009. Cited on page 44.

[110] T.-H. Kim and H. W. Yeom. Topological Solitons versus Nonsolitonic Phase Defects in a Quasi-One-Dimensional Charge-Density Wave. *Physical Review Letters*, 109(24):246802, 2012. Cited on page 45.

[111] T. Ritschel, J. Trinckauf, G. Garbarino, M. Hanfland, M. v. Zimmermann, H. Berger, B. Büchner, and J. Geck. Pressure dependence of the charge density wave in 1T-TaS2 and its relation to superconductivity. *Physical Review B*, 87(12):125135, 2013. Cited on page 51.

[112] B. Sipos, A. F. Kusmartseva, A. Akrap, H. Berger, L. Forró, and E. Tutiš. From Mott state to superconductivity in 1T-TaS2. *Nature Materials*, 7(12):960, 2008. Cited on pages 51, 58 and 59.

[113] C. Sohrt, A. Stange, M. Bauer, and K. Rossnagel. How fast can a Peierls–Mott insulator be melted? *Faraday Discussions*, 171(0):243–257, 2014. Cited on pages 51, 58, 59, 60 and 122.

[114] N. Erasmus, M. Eichberger, K. Haupt, I. Boshoff, G. Kassier, R. Birmurske, H. Berger, J. Demsar, and H. Schwoerer. Ultrafast Dynamics of Charge Density Waves in 4Hb-TaSe2 Probed by Femtosecond Electron Diffraction. *Physical Review Letters*, 109(16):167402, 2012. Cited on page 52.

[115] A. Spijkerman, J. L. de Boer, A. Meetsma, G. A. Wiegers, and S. van Smaalen. X-ray crystal-structure refinement of the nearly commensurate phase of 1T-TaS2 in (3+2)-dimensional superspace. *Physical Review B*, 56(21):13757–13767, 1997. Cited on pages 52, 53, 54, 56 and 76.

[116] R. M. A. Lieth. *Preparation and Crystal Growth of Materials with Layered Structures2*. Springer Science & Business Media, 1977. Cited on page 52.

[117] S. Hellmann, C. Sohrt, M. Beye, T. Rohwer, F. Sorgenfrei, M. Marczynski-Bühlow, M. Kalläne, H. Redlin, F. Hennies, M Bauer, A. Föhlisch, L. Kipp, W. Wurth, and K. Rossnagel. Time-resolved x-ray photoelectron spectroscopy at FLASH. *New Journal of Physics*, 14(1):013062, 2012. Cited on pages 52, 60 and 75.

[118] A. Patane and N. Balkan, eds. *Semiconductor Research*. Vol. 150. Springer Series in Materials Science. Berlin, Heidelberg: Springer Berlin Heidelberg, 2012. Cited on page 52.

[119] E. A. Wood. Vocabulary of Surface Crystallography. *Journal of Applied Physics*, 35(4):1306–1312, 1964. Cited on page 52.

[120] S. Tanda and T. Sambongi. X-ray study of the new charge-density-wave phase in 1T-TaS2. *Synthetic Metals*, 11(2):85–100, 1985. Cited on pages 53, 54 and 59.

[121] K. Nakanishi and H. Shiba. Domain-like Incommensurate Charge-Density-Wave States and the First-Order Incommensurate-Commensurate Transitions in Layered Tantalum Dichalcogenides. I. 1T-Polytype. *Journal of the Physical Society of Japan*, 43(6):1839–1847, 1977. Cited on pages 54, 56, 57, 92, 95, 112 and 115.

[122] W. L. McMillan. Theory of discommensurations and the commensurate-incommensurate charge-density-wave phase transition. *Physical Review B*, 14(4):1496–1502, 1976. Cited on page 54.

[123] Y. Yamada and H. Takatera. Origin of the stabilization of the nearly commensurate phase in 1T-TaS2. *Solid State Communications*, 21(1):41–44, 1977. Cited on pages 54 and 59.

[124] R. Manzke, T. Buslaps, B. Pfalzgraf, M. Skibowski, and O. Anderson. On the phase transitions in 1T-TaS2. *EPL (Europhysics Letters)*, 8(2):195, 1989. Cited on pages 54, 57 and 112.

[125] R. E. Thomson, B. Burk, A. Zettl, and J. Clarke. Scanning tunneling microscopy of the charge-density-wave structure in 1T-TaS 2. *Physical Review B*, 49(24):16899, 1994. Cited on page 54.

[126] F. J. Di Salvo, D. E. Moncton, and J. V. Waszczak. Electronic properties and superlattice formation in the semimetal TiSe2. *Physical Review B*, 14(10):4321–4328, 1976. Cited on page 57.

[127] S. Hellmann, M. Beye, C. Sohrt, T. Rohwer, F. Sorgenfrei, H. Redlin, M. Kalläne, M. Marczynski-Bühlow, F. Hennies, M. Bauer, A. Föhlisch, L. Kipp, W. Wurth, and K. Rossnagel. Ultrafast Melting of a Charge-Density Wave in the Mott Insulator 1T-TaS2. *Physical Review Letters*, 105(18):187401, 2010. Cited on pages 57 and 60.

[128] K. Rossnagel and N. V. Smith. Spin-orbit coupling in the band structure of reconstructed 1T-TaS2. *Physical Review B*, 73(7):073106, 2006. Cited on page 57.

[129] P. Fazekas and E. Tosatti. Charge carrier localization in pure and doped 1T-TaS2. *Physica B+C*, 99(1):183–187, 1980. Cited on pages 58 and 59.

[130] T. Pillo, J. Hayoz, H. Berger, R. Fasel, L. Schlapbach, and P. Aebi. Interplay between electron-electron interaction and electron-phonon coupling near the Fermi surface of 1T-TaS2. *Physical Review B*, 62(7):4277–4287, 2000. Cited on page 58.

[131] F. Zwick, H. Berger, I. Vobornik, G. Margaritondo, L. Forró, C. Beeli, M. Onellion, G. Panaccione, A. Taleb-Ibrahimi, and M. Grioni. Spectral Consequences of Broken Phase Coherence in 1T-TaS2. *Physical Review Letters*, 81(5):1058–1061, 1998. Cited on page 58.

[132] T. Ritschel, J. Trinckauf, K. Koepernik, B. Büchner, M. v. Zimmermann, H. Berger, Y. I. Joe, P. Abbamonte, and J. Geck. Orbital textures and charge density waves in transition metal dichalcogenides. *Nature Physics*, 11(4):328–331, 2015. Cited on page 58.

[133] I. Vaskivskyi, J. Gospodaric, S. Brazovskii, D. Svetin, P. Sutar, E. Goreshnik, I. A. Mihailovic, T. Mertelj, and D. Mihailovic. Controlling the metal-to-insulator relaxation of the metastable hidden quantum state in 1T-TaS2. *Science Advances*, 1(6):e1500168, 2015. Cited on page 59.

[134] I. Vaskivskyi, I. A. Mihailovic, S. Brazovskii, J. Gospodaric, T. Mertelj, D. Svetin, P. Sutar, and D. Mihailovic. Fast electronic resistance switching involving hidden charge density wave states. *Nature Communications*, 7:11442, 2016. Cited on page 59.

[135] L. Stojchevska, I. Vaskivskyi, T. Mertelj, P. Kusar, D. Svetin, S. Brazovskii, and D. Mihailovic. Ultrafast Switching to a Stable Hidden Quantum State in an Electronic Crystal. *Science*, 344(6180):177–180, 2014. Cited on pages 59 and 61.

[136] J. Ravnik, I. Vaskivskyi, T. Mertelj, and D. Mihailovic. Real-time observation of the coherent transition to a metastable emergent state in 1T-TaS2. *arXiv:1711.09710 [cond-mat]*. arXiv: 1711.09710, 2017. Cited on pages 59 and 60.

[137] S. Uchida and S. Sugai. Infrared and Raman studies on commensurate CDW states in transition metal dichalcogenides. *Physica B+C*, 105(1):393–399, 1981. Cited on page 59.

[138] *The Nobel Prize in Physics 2010*. Cited on page 59.

[139] L. Perfetti, P. A. Loukakos, M. Lisowski, U. Bovensiepen, M. Wolf, H. Berger, S. Biermann, and A. Georges. Femtosecond dynamics of electronic states in the Mott insulator 1T-TaS2 by time resolved photoelectron spectroscopy. *New Journal of Physics*, 10(5):053019, 2008. Cited on page 60.

[140] S. Hellmann, T. Rohwer, M. Kalläne, K. Hanff, C. Sohrt, A. Stange, A. Carr, M. Murnane, H. Kapteyn, L. Kipp, M. Bauer, and K. Rossnagel. Time-domain classification of charge-density-wave insulators. *Nature Communications*, 3:1069, 2012. Cited on pages 60 and 61.

[141] J. Demsar, L. Forró, H. Berger, and D. Mihailovic. Femtosecond snapshots of gap-forming charge-density-wave correlations in quasi-two-dimensional dichalcogenides 1T-TaS2 and 2H-TaSe2. *Physical Review B*, 66(4):041101, 2002. Cited on page 60.

[142] Y. Toda, K. Tateishi, and S. Tanda. Anomalous coherent phonon oscillations in the commensurate phase of the quasi-two-dimensional 1T-TaS2 compound. *Physical Review B*, 70(3):033106, 2004. Cited on page 60.

[143] N. Dean, J. C. Petersen, D. Fausti, R. I. Tobey, S. Kaiser, L. V. Gasparov, H. Berger, and A. Cavalleri. Polaronic Conductivity in the Photoinduced Phase of 1T-TaS2. *Physical Review Letters*, 106(1):016401, 2011. Cited on page 60.

[144] A. Mann, E. Baldini, A. Odeh, A. Magrez, H. Berger, and F. Carbone. Probing the coupling between a doublon excitation and the charge-density wave in TaS2 by ultrafast optical spectroscopy. *Physical Review B*, 94(11):115122, 2016. Cited on page 60.

[145] P. Kusar, T. Mertelj, V. V. Kabanov, J.-H. Chu, I. R. Fisher, H. Berger, L. Forró, and D. Mihailovic. Anharmonic order-parameter oscillations and lattice coupling in strongly driven 1T-TaS2 and TbTe3 charge-density-wave compounds: A multiple-

pulse femtosecond laser spectroscopy study. *Physical Review B*, 83(3):035104, 2011. Cited on page 60.

[146] M. Eichberger, H. Schäfer, M. Krumova, M. Beyer, J. Demsar, H. Berger, G. Moriena, G. Sciaini, and R. J. D. Miller. Snapshots of cooperative atomic motions in the optical suppression of charge density waves. *Nature*, 468(7325):799–802, 2010. Cited on page 61.

[147] T.-R. T. Han, F. Zhou, C. D. Malliakas, P. M. Duxbury, S. D. Mahanti, M. G. Kanatzidis, and C.-Y. Ruan. Exploration of metastability and hidden phases in correlated electron crystals visualized by femtosecond optical doping and electron crystallography. *Science Advances*, 1(5):e1400173, 2015. Cited on page 61.

[148] K. Haupt, M. Eichberger, N. Erasmus, A. Rohwer, J. Demsar, K. Rossnagel, and H. Schwoerer. Ultrafast Metamorphosis of a Complex Charge-Density Wave. *Physical Review Letters*, 116(1), 2016. Cited on pages 61, 78, 87 and 112.

[149] C. Laulhé, L. Cario, B. Corraze, E. Janod, T. Huber, G. Lantz, S. Boulfaat, A. Ferrer, S. Mariager, J. Johnson, S. Grübel, A. Lübcke, G. Ingold, P. Beaud, S. Johnson, and S. Ravy. X-ray study of femtosecond structural dynamics in the 2D charge density wave compound 1T-TaS2. *Physica B: Condensed Matter*, 460:100–104, 2015. Cited on page 61.

[150] C. Laulhé, T. Huber, G. Lantz, A. Ferrer, S. O. Mariager, S. Grübel, J. Rittmann, J. A. Johnson, V. Esposito, A. Lübcke, L. Huber, M. Kubli, M. Savoini, V. L. R. Jacques, L. Cario, B. Corraze, E. Janod, G. Ingold, P. Beaud, S. L. Johnson, and S. Ravy. Ultrafast Formation of a Charge Density Wave State in 1T-TaS2: Observation at Nanometer Scales Using Time-Resolved X-Ray Diffraction. *Physical Review Letters*, 118(24):247401, 2017. Cited on pages 61, 87 and 112.

[151] W. E. King, G. H. Campbell, A. Frank, B. Reed, J. F. Schmerge, B. J. Siwick, B. C. Stuart, and P. M. Weber. Ultrafast electron microscopy in materials science, biology, and chemistry. *Journal of Applied Physics*, 97(11):111101, 2005. Cited on page 63.

[152] D. A. Plemmons, P. K. Suri, and D. J. Flannigan. Probing Structural and Electronic Dynamics with Ultrafast Electron Microscopy. *Chemistry of Materials*, 27(9):3178–3192, 2015. Cited on page 63.

[153] A. Feist, K. E. Echternkamp, J. Schauss, S. V. Yalunin, S. Schäfer, and C. Ropers. Quantum coherent optical phase modulation in an ultrafast transmission electron microscope. *Nature*, 521(7551):200–203, 2015. Cited on pages 63 and 78.

[154] R. Feidenhans'l. Surface structure determination by X-ray diffraction. *Surface Science Reports*, 10(3):105–188, 1989. Cited on page 63.

[155] J. Gustafson, M. Shipilin, C. Zhang, A. Stierle, U. Hejral, U. Ruett, O. Gutowski, P.-A. Carlsson, M. Skoglundh, and E. Lundgren. High-Energy Surface X-Ray Diffraction for Fast Surface Structure Determination. *Science*:1246834, 2014. Cited on page 63.

[156] A. Hanisch-Blicharski, A. Janzen, B. Krenzer, S. Wall, F. Klasing, A. Kalus, T. Frigge, M. Kammler, and M. Horn-von Hoegen. Ultra-fast electron diffraction at surfaces: From nanoscale heat transport to driven phase transitions. *Ultramicroscopy*, Frontiers of Electron Microscopy in Materials Science 127:2–8, 2013. Cited on page 63.

[157] R. S. Becker, G. S. Higashi, and J. A. Golovchenko. Low-Energy Electron Diffraction during Pulsed Laser Annealing: A Time- Resolved Surface Structural Study. *Physical Review Letters*, 52(4):307–310, 1984. Cited on page 65.

[158] R. Karrer, H. J. Neff, M. Hengsberger, T. Greber, and J. Osterwalder. Design of a miniature picosecond low-energy electron gun for time-resolved scattering experiments. *Review of Scientific Instruments*, 72(12):4404, 2001. Cited on page 65.

[159] C. Cirelli, M. Hengsberger, A. Dolocan, H. Over, J. Osterwalder, and T. Greber. Direct observation of space charge dynamics by picosecond low-energy electron scattering. *EPL (Europhysics Letters)*, 85(1):17010, 2009. Cited on page 65.

[160] A. Bouhelier. Field-enhanced scanning near-field optical microscopy. *Microscopy Research and Technique*, 69(7):563–579, 2006. Cited on page 67.

[161] A. V. Ermushev, B. V. Mchedlishvili, V. A. Oleĭnikov, and A. V. Petukhov. Surface enhancement of local optical fields and the lightning-rod effect. *Quantum Electronics*, 23(5):435, 1993. Cited on pages 67 and 68.

[162] H. D. Beckey, H. Krone, and F. W. Roellgen. Comparison of tips, thin wires and sharp metal edges as emitters for field ionization mass spectrometry. *Journal of Physics E: Scientific Instruments*, 1(2):118, 1968. Cited on page 67.

[163] R. Gomer. *Field Emissions and Field Ionization*. AVS Classics in Vacuum Science and Technology. AIP-Press, 1993. Cited on page 67.

[164] M. K. Miller, A. Cerezo, M. G. Hetherington, and G. D. W. S. FRS. *Atom Probe Field Ion Microscopy*. Monographs on the Physics and Chemistry of Materials. Oxford, New York: Oxford University Press, 1996. Cited on page 67.

[165] M. Gulde. *Development of an ultrafast low-energy electron diffraction setup*. Dissertation. Göttingen: Georg-August-University, 2014. Cited on pages 67 and 68.

[166] A. Gahlmann, S. Tae Park, and A. H. Zewail. Ultrashort electron pulses for diffraction, crystallography and microscopy: theoretical and experimental resolutions. *Physical Chemistry Chemical Physics*, 10(20):2894, 2008. Cited on page 68.

[167] R. Bormann, S. Strauch, S. Schäfer, and C. Ropers. An ultrafast electron microscope gun driven by two-photon photoemission from a nanotip cathode. *Journal of Applied Physics*, 118(17):173105, 2015. Cited on page 68.

[168] C. C. Neacsu, G. A. Reider, and M. B. Raschke. Second-harmonic generation from nanoscopic metal tips: Symmetry selection rules for single asymmetric nanostructures. *Physical Review B*, 71(20):201402, 2005. Cited on page 68.

[169] J. H. Bechtel, W. Lee Smith, and N. Bloembergen. Two-photon photoemission from metals induced by picosecond laser pulses. *Physical Review B*, 15(10):4557–4563, 1977. Cited on page 69.

[170] R. Yen, J. Liu, and N. Bloembergen. Thermally assisted multiphoton photoelectric emission from tungsten. *Optics Communications*, 35(2):277–282, 1980. Cited on page 69.

[171] G. Herink, D. R. Solli, M. Gulde, and C. Ropers. Field-driven photoemission from nanostructures quenches the quiver motion. *Nature*, 483(7388):190–193, 2012. Cited on page 69.

[172] R. W. Strayer, W. Mackie, and L. W. Swanson. Work function measurements by the field emission retarding potential method. *Surface Science*, 34(2):225–248, 1973. Cited on page 69.

[173] G. Storeck. *Development of an Ultrafast Electron Source for Low Energy Electron Diffraction*. MA thesis. Göttingen: Georg-August-University, 2014. Cited on pages 70 and 117.

[174] G. Storeck, S. Vogelgesang, M. Sivis, S. Schäfer, and C. Ropers. Nanotip-based photoelectron microgun for ultrafast LEED. *Structural Dynamics*, 4(4):044024, 2017. Cited on pages 71, 78, 79, 117 and 121.

[175] P. H. Bucksbaum, D. W. Schumacher, and M. Bashkansky. High-Intensity Kapitza-Dirac Effect. *Physical Review Letters*, 61(10):1182–1185, 1988. Cited on page 78.

[176] D. L. Freimund, K. Aflatooni, and H. Batelaan. Observation of the Kapitza-Dirac effect. *Nature*, 413(6852):142–143, 2001. Cited on page 78.

[177] B. Barwick, D. J. Flannigan, and A. H. Zewail. Photon-induced near-field electron microscopy. *Nature*, 462(7275):902–906, 2009. Cited on page 78.

[178] A. Dolocan, M. Hengsberger, H. J. Neff, M. Barry, C. Cirelli, T. Greber, and J. Osterwalder. Electron–Photon Pulse Correlator Based on Space-Charge Effects in a Metal Pinhole. *Japanese Journal of Applied Physics*, 45(1R):285, 2006. Cited on page 78.

[179] G. F. Mancini, B. Mansart, S. Pagano, B. van der Geer, M. de Loos, and F. Carbone. Design and implementation of a flexible beamline for fs electron diffraction experiments. *Nuclear Instruments and Methods in Physics Research Section A: Accelerators, Spectrometers, Detectors and Associated Equipment*, 691:113–122, 2012. Cited on page 78.

[180] A. Janzen, B. Krenzer, O. Heinz, P. Zhou, D. Thien, A. Hanisch, F.-J. Meyer zu Heringdorf, D. von der Linde, and M. Horn von Hoegen. A pulsed electron gun for ultrafast electron diffraction at surfaces. *Review of Scientific Instruments*, 78(1):013906, 2007. Cited on page 78.

[181] L. Merz, T. Bauert, M. Parschau, G. Koller, J. S. Siegel, and K.-H. Ernst. Polymorph selection in 2D crystals by phase transition blocking. *Chemical Communications*, (39):5871, 2009. Cited on pages 79 and 121.

[182] C. Godrèche. *Solids Far from Equilibrium*. Cambridge University Press, 1991. Cited on pages 91 and 92.

[183] K. Nakanishi, H. Takatera, Y. Yamada, and H. Shiba. The Nearly Commensurate Phase and Effect of Harmonics on the Successive Phase Transition in 1T-TaS2. *Journal of the Physical Society of Japan*, 43(5):1509–1517, 1977. Cited on page 92.

[184] P. L. DeVries. Application of the Split Operator Fourier Transform method to the solution of the nonlinear Schrödinger equation. *AIP Conference Proceedings*, 160(1):269–271, 1987. Cited on page 94.

[185] M. R. Hermann and J. A. Fleck. Split-operator spectral method for solving the time-dependent Schrödinger equation in spherical coordinates. *Physical Review A*, 38(12):6000–6012, 1988. Cited on page 94.

[186] J. Frank. *Numerical Modelling of Dynamical Systems, Chapter 13. Splitting Methods*. 2008. Cited on page 94.

[187] J. Ishioka, Y. H. Liu, K. Shimatake, T. Kurosawa, K. Ichimura, Y. Toda, M. Oda, and S. Tanda. Chiral Charge-Density Waves. *Physical Review Letters*, 105(17):176401, 2010. Cited on page 106.

[188] T. W. B. Kibble. Topology of cosmic domains and strings. *Journal of Physics A: Mathematical and General*, 9(8):1387, 1976. Cited on page 112.

[189] S. Deutschländer, P. Dillmann, G. Maret, and P. Keim. Kibble–Zurek mechanism in colloidal monolayers. *Proceedings of the National Academy of Sciences*, 112(22):6925–6930, 2015. Cited on page 112.

[190] A. J. Bray and A. D. Rutenberg. Growth laws for phase ordering. *Physical Review E*, 49(1):R27–R30, 1994. Cited on pages 112 and 113.

[191] F. Rojas and A. D. Rutenberg. Dynamical scaling: The two-dimensional XY model following a quench. *Physical Review E*, 60(1):212–221, 1999. Cited on page 113.

[192] M. Zapotocky, P. M. Goldbart, and N. Goldenfeld. Kinetics of phase ordering in uniaxial and biaxial nematic films. *Physical Review E*, 51(2):1216–1235, 1995. Cited on page 113.

[193] A. N. Pargellis, S. Green, and B. Yurke. Planar XY-model dynamics in a nematic liquid crystal system. *Physical Review E*, 49(5):4250–4257, 1994. Cited on page 113.

[194] T. Nagaya, H. Orihara, and Y. Ishibashi. Coarsening Dynamics of +1 and -1 Disclinations in Two-Dimensionally Aligned Nematics - Spatial Distribution of Disclinations. *Journal of the Physical Society of Japan*, 64(1):78–85, 1995. Cited on page 113.

[195] M. Mondello and N. Goldenfeld. Scaling and vortex dynamics after the quench of a system with a continuous symmetry. *Physical Review A*, 42(10):5865–5872, 1990. Cited on page 113.

[196] A. N. Pargellis, P. Finn, J. W. Goodby, P. Panizza, B. Yurke, and P. E. Cladis. Defect dynamics and coarsening dynamics in smectic-C films. *Physical Review A*, 46(12):7765–7776, 1992. Cited on page 113.

[197] A. D. Rutenberg and A. J. Bray. Energy-scaling approach to phase-ordering growth laws. *Physical Review E*, 51(6):5499–5514, 1995. Cited on page 113.

[198] B. Yurke, A. N. Pargellis, T. Kovacs, and D. A. Huse. Coarsening dynamics of the XY model. *Physical Review E*, 47(3):1525–1530, 1993. Cited on page 113.

[199] K. Nam, W.-B. Baek, B. Kim, and S. J. Lee. Coarsening of two dimensional XY model with Hamiltonian dynamics: Logarithmically divergent vortex mobility. *Journal of Statistical Mechanics: Theory and Experiment*, 2012(11). arXiv: 1211.1462:P11023, 2012. Cited on page 113.

[200] H. Qian and G. F. Mazenko. Vortex Dynamics in a Coarsening Two Dimensional XY Model. *Physical Review E*, 68(2). arXiv: cond-mat/0304346, 2003. Cited on page 113.

[201] H. Dai and C. M. Lieber. Solid-hexatic-liquid phases in two-dimensional charge-density waves. *Physical Review Letters*, 69(10):1576–1579, 1992. Cited on page 115.

[202] R. Pindak, D. E. Moncton, S. C. Davey, and J. W. Goodby. X-Ray Observation of a Stacked Hexatic Liquid-Crystal B Phase. *Physical Review Letters*, 46(17):1135–1138, 1981. Cited on page 115.

[203] J. D. Brock, D. Y. Noh, B. R. McClain, J. D. Litster, R. J. Birgeneau, A. Aharony, P. M. Horn, and J. C. Liang. Hexatic ordering in freely suspended liquid crystal films. *Zeitschrift für Physik B Condensed Matter*, 74(2):197–213, 1989. Cited on page 115.

[204] M. Cheng, J. T. Ho, S. W. Hui, and R. Pindak. Electron-diffraction study of free-standing liquid-crystal films. *Physical Review Letters*, 59(10):1112–1115, 1987. Cited on page 115.

[205] M. Cheng, J. T. Ho, S. W. Hui, and R. Pindak. Observation of Two-Dimensional Hexatic Behavior in Free-Standing Liquid-Crystal Thin Films. *Physical Review Letters*, 61(5):550–553, 1988. Cited on page 115.

[206] I. R. Peterson and V. M. Kaganer. Diffraction line profile of a two-dimensional hexatic. *Physical Review Letters*, 73(1):102–105, 1994. Cited on pages 115 and 116.

[207] S. Mangin, M. Gottwald, C.-H. Lambert, D. Steil, V. Uhlíř, L. Pang, M. Hehn, S. Alebrand, M. Cinchetti, G. Malinowski, Y. Fainman, M. Aeschlimann, and E. E. Fullerton. Engineered materials for all-optical helicity-dependent magnetic switching. *Nature Materials*, 13(3):286–292, 2014. Cited on page 117.

[208] A. Zong, X. Shen, A. Kogar, L. Ye, C. Marks, D. Chowdhury, T. Rohwer, B. Freelon, S. Weathersby, R. Li, J. Yang, J. Checkelsky, X. Wang, and N. Gedik. Ultrafast manipulation of mirror domain walls in a charge density wave. *Science Advances*, 4(10):eaau5501, 2018. Cited on page 117.

[209] Y. Ma, S. Kolekar, H. Coy Diaz, J. Aprojanz, I. Miccoli, C. Tegenkamp, and M. Batzill. Metallic Twin Grain Boundaries Embedded in MoSe2 Monolayers Grown by Molecular Beam Epitaxy. *ACS Nano*, 11(5):5130–5139, 2017. Cited on page 121.

[210] Y. Kang, S. Najmaei, Z. Liu, Y. Bao, Y. Wang, X. Zhu, N. J. Halas, P. Nordlander, P. M. Ajayan, J. Lou, and Z. Fang. Plasmonic Hot Electron Induced Structural Phase Transition in a MoS2 Monolayer. *Advanced Materials*, 26(37):6467–6471, 2014. Cited on page 121.

[211] F. J. Himpsel, K. N. Altmann, R. Bennewitz, J. N. Crain, A. Kirakosian, J.-L. Lin, and J. L. McChesney. One-dimensional electronic states at surfaces. *Journal of Physics: Condensed Matter*, 13(49):11097, 2001. Cited on page 121.

[212] F. Hötzel, N. Galden, S. Baur, and A. Pucci. One-Dimensional Plasmonic Excitations in Gold-Induced Superstructures on Si(553): Impact of Gold Coverage and Silicon Step Edge Polarization. *The Journal of Physical Chemistry C*, 121(14):8120–8127, 2017. Cited on page 121.

[213] M. Krawiec, T. Kwapiński, and M. Jałochowski. Scanning tunneling microscopy of monoatomic gold chains on vicinal Si(335) surface: experimental and theoretical study. *physica status solidi (b)*, 242(2):332–336, 2005. Cited on page 121.

[214] D. Mou, A. Sapkota, H.-H. Kung, V. Krapivin, Y. Wu, A. Kreyssig, X. Zhou, A. I. Goldman, G. Blumberg, R. Flint, and A. Kaminski. Discovery of an Unconventional Charge Density Wave at the Surface of K 0.9 Mo 6 O 17. *Physical Review Letters*, 116(19), 2016. Cited on page 121.

[215] W. Steurer. Structural phase transitions from and to the quasicrystalline state. *Acta Crystallographica Section A: Foundations of Crystallography*, 61(1):28–38, 2005. Cited on page 121.

[216] A. Y. Brewer, T. Friscic, G. Day, L. M. Overvoorde, J. E. Parker, C. N. Richardson, and S. M. Clarke. The monolayer structure of 1,2-bis(4-pyridyl)ethylene physisorbed on a graphite surface. *Molecular Physics*, 111(1):73–79, 2013. Cited on page 121.

[217] Z. Y. Li. Orientational order of ultrathin C60 films on graphite. *Surface Science*:7, 1999. Cited on page 121.

[218] T. L. Cocker, D. Peller, P. Yu, J. Repp, and R. Huber. Tracking the ultrafast motion of a single molecule by femtosecond orbital imaging. *Nature*, 539(7628):263–267, 2016. Cited on page 122.

Danksagung

An erster Stelle möchte ich Prof. Dr. Claus Ropers für die ausgezeichnete Betreuung dieser Doktorarbeit danken. Nahezu jederzeit für Fragen oder Diskussionen zur Verfügung zu stehen, ist bei weitem nicht selbstverständlich und gebührt großer Anerkennung.

Ebenso gilt mein Dank Prof. Dr. Stefan Mathias für sein Interesse am ULEED Projekt und das Korreferat dieser Arbeit.

Weiterer Dank geht an Prof. Dr. Kai Roßnagel und Kerstin Hanff aus Kiel für zahlreiche 1T-TaS$_2$ Proben sowie für anregende Diskussionen zu Ladungsdichtewellen oder Probenpräparation.

Das Korrekturlesen dieser Doktorarbeit haben zu großen Teilen Benjamin von Ardenne, Jan Gerrit Horstmann und Armin Feist übernommen. Vielen Dank an euch!

Für den Erfolg einer Doktorarbeit sind Motivation und Spaß an der täglichen Arbeit unerlässlich. Eine zentrale Rolle spielen dabei die kollegiale Atmosphäre und Hilfsbereitschaft, die ich in den vergangenen fünf Jahren in dieser Arbeitsgruppe erleben durfte.

In diesem Zusammenhang möchte ich das ULEED Team hervorheben und Gero Storeck bzw. Jan Gerrit Horstmann erwähnen, mit denen ich viel Zeit im Labor verbracht habe. Ohne euch wäre so manches UHV Leck zu später Stunde sicher nicht zu stopfen gewesen.

Ebenso sollen auch Karin Ahlborn und Bernhard Spicher Erwähnung finden, die mit vielen technischen Ratschlägen, zahlreichen geliehenen Bauteilen und tatkräftiger Hilfe zum Erfolg des ULEED Projekts beigetragen haben.

Für ihre Unterstützung während des Studiums und der Promotion gebührt ein besonderer Dank meiner Familie. Der Rückhalt, den mir meine Eltern Hans und Monika, mein Bruder Daniel und meine Großeltern in allen Lebenslagen zukommen lassen, gibt Zuversicht und Kraft, auch größere Herausforderungen anzunehmen.

Vor allem möchte ich jedoch meiner lieben Frau Anja danken. Dich und Clara an meiner Seite zu wissen, ist ein wunderbares Geschenk, das mir jeden Tag aufs neue große Freude bereitet.